UNIVERSITY OF OKLAHOMA

GRADUATE COLLEGE

CHARACTERIZING TRANSFER ZONES WITH SEISMIC AND EXPERIMENTAL MODELS

A DISSERTATION SUBMITTED TO THE GRADUATE FACULTY

in partial fulfillment of the requirements for the

Degree of

Doctor of Philosophy

By

PIERRE KARAM

Norman, Oklahoma

2020

Downloaded from SHAREOK. Persistent Handle URL: https://hdl.handle.net/11244/325330

CHARACTERIZING TRANSFER ZONES WITH SEISMIC AND EXPERIMENTAL MODELS

A DISSERTATION APPROVED FOR THE

SCHOOL OF GEOSCIENCES

BY THE COMMITTEE CONSISTING OF

Dr. Brett M. Carpenter, Chair

Dr. Kurt Marfurt, Co-Chair

Dr. Heather Bedle

Dr. Zulfiquar Reza

© Copyright by PIERRE KARAM 2020

All Rights Reserved.

TABLE OF CONTENTS

LIST OF FIGURES VII

LIST OF TABLES XV

ACKNOWLEDGEMENTS XVI

ABSTRACT XVIII

CHAPTER 1: INTRODUCTION 1

1. TRANSFER ZONE DEFINITION 1
2. GROWTH MECHANISM 3
3. RELAY RAMP BREACHING AND FRACTURING 6
4. SEISMIC APPLICATION 8
5. STUDY OBJECTIVES 11

CHAPTER 2: SEISMIC EXPRESSION OF TRANSFER ZONES 12

1. INTRODUCTION TO THE TARANAKI BASIN 12
2. DATA AND INTERPRETATION METHODS 15
3. FAULT CHARACTERIZATION 19
4. RELAY RAMP CHARACTERIZATION 24
5. SEISMIC ATTRIBUTE ANALYSIS 29
6. APPLICATIONS OF SEISMIC ATTRIBUTES 31
   a) Horizon-Based vs Volumetric Dip Calculations 31
   b) Coherence or Variance 33
   c) Seismic Curvature 38
7. ANALYSIS 42

CHAPTER 3: ASSESSING FAULT SEALING POTENTIAL AT TRANSFER ZONES 44

1. INTRODUCTION TO FAULT SEALING METHODS 45
2. METHODOLOGY 52
3. TECTONIC BACKGROUND 54
4. FORMATION CHARACTERIZATION 56
5. SEISMIC INVERSION WORK 58
   a) Inversion Assumptions 58
   b) Rock Properties Modeling 60
6. INVERSION RESULTS 66
7. FAULT SEAL ANALYSIS 71
   a) 1D Well Juxtaposition Analysis 71
8. CONCLUSION 73
   b) 3D Faults Sealing Analysis 75
   c) Transfer Zone Sealing Analysis 79
9. CONCLUSIONS 84

CHAPTER 4: LITHOLOGICAL CONTROLS ON TRANSFER ZONES 86

1. INTRODUCTION 86
2. EXPERIMENTAL SETUP: 89
3. EXPERIMENTAL RESULTS 91
   a) Ductile Models: 91
   b) Brittle Models: 94
   c) Deformation Variations: 98

4. NATURAL EXAMPLES 101

5. SEISMIC EXAMPLE 105

6. RESERVOIR POTENTIAL 108

7. CONCLUSION 111

CHAPTER 5: CONCLUSIONS 113

REFERENCES 115

APPENDIX 125

LIST OF FIGURES

FIGURE 1.1. TRANSFER ZONE CLASSIFICATION BASED ON MORLEY ET AL. (1990) 5

FIGURE 1.2. DIFFERENT STAGES OF TRANSFER ZONE EVOLUTION AS DESCRIBED BY PEACOCK AND SANDERSON (1994)..... 5

FIGURE 1.3. SEISMIC ATTRIBUTES COLORED ALONG THE FAULT PLANE, PLOTTED AGAINST FAULT DISPLACEMENT (LOHR ET AL, 2008). 10

FIGURE 2.1. PLATE BOUNDARY SETTING OF THE NORTH ISLAND IN NEW ZEALAND. (A) REGIONAL SETTING DURING THE LATE CRETACEOUS (B) ZOOMED IN LOOK AT THE REGION DURING LATE CRETACEOUS (C) PARIHAKA FAULT DURING THE EARLY PLIOCENE (D) PARIHAKA FAULT DURING THE PLEISTOCENE (EDITED FROM GIBA ET AL. 2012). 14

FIGURE 2.2. TIME SLICE AT T=860MS THROUGH A COHERENCE VOLUME SHOWING THE LOCATION OF THE MAIN FAULTS IN THE AREA (A, B, C, AND D), THE ARAWA 1 WELL, AND THE LOCATION OF CROSS-SECTION AA'. THE NE TRENDING ACQUISITION FOOTPRINT CORRESPONDS TO THE SAIL LINE OF SEISMIC ACQUISITION. HIGH COHERENCE ELLIPTICAL FEATURES ARE SHALLOW GAS ACCUMULATIONS FORMING BRIGHT SPOTS WHICH CAN BE SEEN IN THE FOLLOWING FIGURE. 18

FIGURE 2.3. CROSS-SECTION AA' SHOWING ALL 11 HORIZONS INTERPRETED TO ASSESS RELAY RAMP FORMATION. 19

FIGURE 2.4. TIME-DEPTH CONVERSION CHART FROM THE WELL DATA WITHIN THE SEISMIC SURVEY. 20

FIGURE 2.5. DISPLACEMENT PROFILE FOR ALL HORIZONS FOR FAULT B..... 22

FIGURE 2.6.GROWTH INDEX (RATIO OF DOWNTHROWN TO UPTHROWN THICKNESS) FOR ALL THREE (3) FAULTS. 22

FIGURE 2.7. FAULT LENGTH PLOTTED VERSUS FAULT DISPLACEMENT OF ALL HORIZONS FOR THE FOUR (4) MAJOR FAULTS. 24

FIGURE 2.8. CROSS-SECTION ALONG THE MAIN FAULTS EXTENDING FROM THE SW TO THE NE DIRECTION SHOWING DISPLACEMENT FOR FOUR (4) MAIN HORIZONS. 25

FIGURE 2.9. (A) SLICE ALONG HORIZON 8 THROUGH THE VARIANCE VOLUME SHOWING THE LOCATION OF THE RELAY RAMPS (1 AND 2) (B) 3D VISUALIZATION OF THE RELAY RAMPS AS SEEN IN HORIZONS 3 AND 8. 28

FIGURE 2.10. MEASURED RAMP LENGTH PLOTTED AGAINST MAXIMUM DISPLACEMENT ASSOCIATED WITH THE RELATED FAULTS. 29

FIGURE 2.11. RELAY RAMP WIDTH PLOTTED WITH MAXIMUM DISPLACEMENT FOR ALL FOUR (4) FAULTS AT EVERY HORIZON 29

FIGURE 2.12. COMPARISON BETWEEN DIP MAGNITUDE COMPUTED FROM AN INTERPRETED HORIZON AND A HORIZON SLICE THROUGH A VOLUMETRIC DIP COMPUTATION FOR HORIZON 6 (A) AND (B), AND FOR HORIZON 8 (C) AND (D) RESPECTIVELY (MAPPING GRID SIZE IS 100 M × 100 M). NOTE THE IMPROVED RESOLUTION OF THE THREE TURBIDITE CHANNELS IN (D) VS. (C). THE SUBTLE LEFT-TO-RIGHT CORRUGATIONS ARE DUE TO ACQUISITION FOOTPRINT. 32

FIGURE 2.13. HORIZON SLICES THROUGH THE DIP MAGNITUDE VOLUME FOR HORIZONS 1 THROUGH 6 FOR RAMP 1. 34

FIGURE 2.14. HORIZON SLICES THROUGH THE DIP MAGNITUDE VOLUME FOR HORIZONS 2 THROUGH 8 FOR RAMP 2. 35

FIGURE 2.15. MAPPED VARIANCE ONTO THE FAULT PLANES WITH RED INDICATING AN INCREASE IN VARIANCE FROM HORIZONS 1 TO 11 (FAULTS FOUR TIMES VERTICALLY EXAGGERATED). 36

FIGURE 2.16. CALCULATED DISPLACEMENT USING DEPTH CONVERTED SEISMIC DATA SHOWING AN INCREASE OF DISPLACEMENT TOWARDS THE BOTTOM-CENTER PART OF THE FAULTS (FOUR TIMES VERTICALLY EXAGGERATED)..... 36

FIGURE 2.17. CALCULATED HEAVE USING DEPTH CONVERTED SEISMIC DATA SHOWING AN INCREASE OF DISPLACEMENT TOWARDS THE BOTTOM-CENTER PART OF THE FAULTS (FOUR TIMES VERTICALLY EXAGGERATED)..... 37

FIGURE 2.18. MAXIMUM DISPLACEMENT SEEN FOR EVERY FAULT AT EVERY HORIZON PLOTTED AGAINST AVERAGE VARIANCE MEASURED FROM MAPPED SEISMIC ATTRIBUTES..... 37

FIGURE 2.19. ZOOMED IMAGES OF HORIZON SLICES ALONG HORIZONS 6 AND 8 THROUGH THE VARIANCE VOLUME SHOWING SMALL SUB SEISMIC FAULTING ALONG RAMPS 1 AND 2. 39

FIGURE 2.20. TIME-STRUCTURE MAPS OF HORIZONS 2, 8, AND 11, AND A VERTICAL SLICE THROUGH CO-RENDERED MOST-POSITIVE CURVATURE, K1, MOST-NEGATIVE CURVATURE, K2, AND SEISMIC AMPLITUDE, SHOWING THE CORRELATION OF POSITIVE CURVATURE ANOMALIES WITH THE HANGING..... 41

FIGURE 2.21. CO-RENDERED MOST-POSITIVE (K_1) AND MOST-NEGATIVE (K_2) CURVATURES COMPUTED FROM PICKED HORIZONS 1 THROUGH 9 SHOWING AN INCREASE IN CURVATURE ASSOCIATED WITH INCREASED DISPLACEMENT. 42

FIGURE 3.1. JUXTAPOSITION DIAGRAM USING STRATIGRAPHIC LAYERS AND FAULT THROW (KNIPE, 1997). 46

FIGURE 3.2. (A) OUTCROP AND EXPERIMENTAL DATA FOR CLAY SMEAR CONTINUITY, (B) SMEAR PROBABILITY FROM 80M OF FAULT TRACES IN THE ROUND O QUARRY (AFTER YIELDING, 1996). 48

FIGURE 3.3. BOWERS' PORE PRESSURE ESTIMATION (BOWERS, 1995)..... 49

FIGURE 3.4. (A) PORE PRESSURE ESTIMATION FOR THE NORIAN HORIZON, (B) STRUCTURE MAP FOR THE NORIAN FORMATION SHOWING STRUCTURAL CHANGES AND MAJOR INTERPRETED FAULTS IN THE AREA (EDITED FROM TOBIAS ET AL, 2015). 51

FIGURE 3.5. MAP VIEW OF THE DATA AVAILABILITY INCLUDING THE SEISMIC DATA (AMPLITUDE SLICE SHOWN) ALONG WITH INTERPRETED FAULTS AND FOUR VERTICAL WELLS (FOR A ZOOM IN OF THE FAULT SYSTEM REFER TO FIGURE 2.2). 53

FIGURE 3.6. CROSS-SECTION THROUGH THE MAIN FOUR (4) WELLS WITHIN OUR AREA OF INTEREST SHOWING THE COMPRESSIONAL AND SHEAR SLOWNESS DATA. 54

FIGURE 3.7. TARANAKI BASIN STRATIGRAPHIC COLUMN (KING AND THRASHER, 1996). 56

FIGURE 3.8. CROSS-SECTION THROUGH THE MAIN 3 WELLS WITH GAMMA RAY (GREEN), COMPRESSIONAL SLOWNESS (RED), DENSITY (BLACK), AND NEUTRON (PURPLE) LOGS. 58

FIGURE 3.9. STATISTICAL WAVELET EXTRACTED FROM SEISMIC AND USED FOR WELL-TIE AND INVERSION. 59

FIGURE 3.10. AMPLITUDE SPECTRUM OF THE SEISMIC DATA. 60

FIGURE 3.11. RELATIONSHIP BETWEEN VP/VS AND P-IMPEDANCE COLORED BY POROSITY (HOT COLORS ARE HIGHER POROSITY). 62

FIGURE 3.12. POROSITY-PERMEABILITY RELATIONSHIP FROM CORE PLUGS FOR DIFFERENT WELLS. 63

FIGURE 3.13. PLOT SHOWING RELATIONSHIP BETWEEN GAMMA RAY AND P-IMPEDANCE COLORED BY DERIVED POROSITY FOR THE MAIN WELLS IN THE AREA. 65

FIGURE 3.14. DEFINITION OF SHALE AND SAND TREND USING THE DENSITY AND P-IMPEDANCE CORRELATION COLORED BY VOLUME OF SHALE. 66

FIGURE 3.15. RELATION BETWEEN ORIGINAL AND PREDICTED P-IMPEDANCE FOR VARIOUS WELLS. 67

FIGURE 3.16. COMPARISON BETWEEN (FROM THE LEFT TO RIGHT) THE POROSITY, GAMMA RAY, AND P-IMPEDANCE VOLUMES AT THE INLINE PASSING THROUGH THE ARAWA #1 WELL BASED FROM THE INVERSION VOLUMES. 68

FIGURE 3.17. POROSITY VS GAMMA RAY COLORED BY FACIES FROM THE MUDLOG DATA AVAILABLE FOR THE ARAWA #1 WELL 70

FIGURE 3.18. 3D VIEW OF FACIES DISTRIBUTION AT BOTH TRANSFER ZONES. 70

FIGURE 3.19. SEAL DIAGRAM FOR THE ARAWA #1 WELL BASED ON DERIVED FACIES LOGS. 72

FIGURE 3.20. SIGNIFICANT COMBINATIONS HIGHLIGHTING IN GREEN FOR AREAS OF POTENTIAL LEAKING (A) AND AREA OF RED (SAND-SHALE), SEALING POTENTIAL (B). 73

FIGURE 3.21. LOOKING FACE ON THE FAULT PLANE (A) 3D VISUALIZATION OF THE LEAST PERMEABLE FACIES ALONG FAULT A, (B) 3D VISUALIZATION OF THE SGR ESTIMATED FOR FAULT A. 77

FIGURE 3.22. LOOKING FACE ON THE FAULT PLANE (A) 3D VISUALIZATION OF THE LEAST PERMEABLE FACIES ALONG FAULT B, (B) 3D VISUALIZATION OF THE SGR ESTIMATED FOR FAULT B. 78

FIGURE 3.23. LOOKING FACE ON THE FAULT PLANE (A) 3D VISUALIZATION OF THE LEAST PERMEABLE FACIES ALONG FAULT B, (B) 3D VISUALIZATION OF THE SGR ESTIMATED FOR FAULT C. 79

FIGURE 3.24. MAP VIEWS OF THE M00 INTERVALS COLORED BY SAND FACIES INTERVAL THICKNESS (DARKER IS THICKER) AND ASSESSED FOR SEALING POTENTIAL USING BOTH METHODS: (A) STRATIGRAPHIC JUXTAPOSITION AND (B) SGR METHOD. 81

FIGURE 3.25. MAP VIEWS OF THE M10 INTERVALS COLORED BY SAND FACIES INTERVAL THICKNESS (DARKER IS THICKER) AND ASSESSED FOR SEALING POTENTIAL USING BOTH METHODS: (A) STRATIGRAPHIC JUXTAPOSITION AND (B) SGR METHOD. 82

FIGURE 3.26. MAP VIEWS OF THE M20 INTERVALS COLORED BY SAND FACIES INTERVAL THICKNESS (DARKER IS THICKER) AND ASSESSED FOR SEALING POTENTIAL USING BOTH METHODS: (A) STRATIGRAPHIC JUXTAPOSITION AND (B) SGR METHOD. 83

FIGURE 4.1. INFLUENCE OF MECHANICAL STRATIGRAPHY ON FAULT GROWTH AND FOR RELAY RAMP DEVELOPMENT (FERRILL AND MORRIS, 2008) 88

FIGURE 4.2. EXPERIMENTAL SETUP SHOWING A 3D VIEW OF THE APPARATUS USED AND THE THREE PLATE CUTS USED STUDY BEND ANGLE IMPACT. 90

FIGURE 4.3. 3D VIEW OF THE TRANSFER ZONE AT THE END OF EXPERIMENT 1 SHOWING THE BED TILTING AND SIGNIFICANT FAULTING WITH THE RELAY RAMP. 92

FIGURE 4.4. DETAILED EVOLUTION OF THE STRUCTURE AT THREE STAGES (EARLY, MID, AND LATE CORRESPONDING TO BEGINNING OF FAULTING, MIDWAY, AND FINAL FAULTING STAGE) FOR EXPERIMENTS 1, 2, AND 3. 93

FIGURE 4.5. FINAL TOPOGRAPHIC MAP OF EACH EXPERIMENT (1, 2, 3) MODELED AND BUILT IN PETREL SHOWING DEEPER PARTS OF THE BASIN IN PURPLE. 94

FIGURE 4.6. TRANSFER ZONE FOR EXPERIMENT 4 BEYOND THE ORIGINAL EXTENSION DESIRED SHOWING THE FAULTS CURVING INTO EACH OTHER. 96

FIGURE 4.7. DETAILED EVOLUTION OF THE STRUCTURE AT THREE STAGES (EARLY, MID, AND LATE, CORRESPONDING TO BEGINNING OF FAULTING, MIDWAY, AND FINAL FAULTING STAGE) FOR EXPERIMENTS 4, 5, AND 6. 97

FIGURE 4.8. FINAL STRUCTURE OF EACH EXPERIMENT (4, 5, AND 6) MODELED AND BUILT IN PETREL SHOWING DEEPER PARTS OF THE BASIN IN PURPLE. 98

FIGURE 4.9. DISPLACEMENT INCREASE AT EACH STAGE FOR EXPERIMENT 1 (STAGE 1 IS AT THE BEGINNING AND STAGE 4 IS AT THE END OF THE EXPERIMENT). 100

FIGURE 4.10. DISPLACEMENT INCREASE AT EACH STAGE FOR EXPERIMENT 4 (STAGE 1 IS AT THE BEGINNING AND STAGE 4 IS AT THE END OF THE EXPERIMENT). 101

FIGURE 4.11. STRUCTURAL MAP AT THE YUCCA MOUNTAIN (BRITTLE ROCK) SHOWING TRANSFER ZONES AND FAULTING STYLE USING LIDAR DATA. 104

FIGURE 4.12. STRUCTURAL MAP AT THE UNCOMPAHGRE UPLIFT (DUCTILE ROCK) SHOWING TRANSFER ZONES AND FAULTING STYLE USING LIDAR DATA. 105

FIGURE 4.13. DIP ATTRIBUTES EXTRACTED ALONG AN INTERPRETED HORIZON OF THE PARIHAKA FAULT OFFSHORE NEW ZEALAND. 106

FIGURE 4.14. DIP MAGNITUDE CALCULATED FOR EXPERIMENTAL MODELS USING TOPOGRAPHIC DATA COLLECTED DURING LASER SCANNING AT THE END OF EACH EXPERIMENT. 108

FIGURE 4.15. SURFACE PROFILE FOR EXPERIMENTS 1, 2, AND 3 ALONG THE RELAY RAMPS AT SECTION AA', BB', AND CC'. 109

FIGURE 4.16. 3D VIEW OF THE TRANSFORM ZONE FOR EXPERIMENTS 1 AND 4 SHOWING THE STRUCTURE AND DISTRIBUTION OF FAULTS/FRACTURES AT THE END OF THE EXPERIMENT (LATE STAGE). 111

FIGURE A.1. SEISMIC WELL-TIE FOR THE ARAWA #1 WELL. 125

FIGURE A.2. SEISMIC WELL-TIE FOR THE OKOKI #1 WELL. 126

FIGURE A.3. SEISMIC WELL-TIE FOR THE TAIMANA #1 WELL. 127

FIGURE A.4. SEISMIC WELL-TIE FOR THE WITORIA #1 WELL. 128

FIGURE A.5. COMPARISON BETWEEN WELL LOGS AND INVERTED P-IMPEDANCE. 129

FIGURE A.6. COMPARISON BETWEEN WELL LOGS AND INVERTED S-IMPEDANCE. 129

FIGURE A.7. COMPARISON BETWEEN WELL LOGS AND INVERTED DENSITY LOGS..... 130

FIGURE A.8. RELATIONSHIP BETWEEN P-WAVE VELOCITY AND PREDICTED S-WAVE VELOCITY USING A NEUTRAL NETWORK..... 130

FIGURE A.9. COMPARISON BETWEEN WELL LOGS AND EXTRACTED SEISMIC INVERSION PROPERTIES (SHOWN IN RED) AT THE ARAWA #1 WELL LOCATION. 131

FIGURE A.10. 3D SEISMIC TO WELL TIE SHOWING THE MAIN FORMATION TOPS TIED TO THE INTERPRETED HORIZON. 132

LIST OF TABLES

TABLE 2.1. APPROXIMATE AGE OF HORIZONS BASED ON BIOMARKER DATA FROM ARAWA 1. 21

TABLE 3.1. SUMMARY OF THE TRANSFER ZONE ANALYSIS RESULTS AT EACH ZONE USING BOTH STRATIGRAPHIC JUXTAPOSITION AND SGR METHODS. 83

TABLE 4.1. SUMMARY OF THE EXPERIMENTS CONDUCTED AND THEIR CORRESPONDING PROPERTIES. 91

ACKNOWLEDGEMENTS

I would like, first and foremost, to thank God almighty for helping through this journey and for his blessings throughout those years at the University of Oklahoma.

I would like to express my deep and sincere gratitude to my research committee chair, Dr. Brett M. Carpenter, and to the co-chair, Dr. Kurt Marfurt, for providing valuable guidance and input into my research and for supporting the on-going work that lead to the completion of this dissertation. In addition, I would like to extend my gratitude to my committee members Dr. Heather Bedle and Dr. Zulfiquar Reza for serving on my committee and reviewing the work presented. I would like also to thank my retired advisor, Dr. Shankar Mitra, who accepted me into the program and provided guidance and support for my continued education and research. Finally, in memory of our beloved Dr. Roger Slatt, who is an inspiration for all geology students at the University of Oklahoma, and who through his care and passion, touched everyone's life and impacted everyone's career, including mine.

Furthermore, the work would have not been completed without the support of Baker Hughes Inc and Devon Energy, specially my manager at Devon, Mr. Ken Pfau, who have allowed me to continue my education while working and have supported research through funding and software mainly through JewelSuite modeling software. Similarly, I would like to thank the University of Oklahoma, Schlumberger (Petrel), Hampson Russell, and the AASPI consortium for providing the software and tools to make this work possible.

I am extremely thankful as well for the care, support, guidance, and input that I have received from all the OU Geosciences family including students, professors, staff, and researchers, whom I have truly enjoyed being a part of, for the last 8 years of my life. A special shout out goes

to Rebecca Fay, the coordinator of Academic Student Services for Geology and Geophysics, for all her support and help with dissertation related paperwork.

Finally, to my beautiful beloved wife, Paulina, our little handsome son John-Paul Charbel, my parents Jean and Marie, my sister Carla, and all family members and friends in Lebanon and all over the world, thank you for everything. Thank you for your prayers, patience, understanding, support, guidance, encouragement, for being there for me, for staying close when I had to be away, and above all for your love. It has been a long journey, and I would have never been able to be here without you. I love you and thank you all.

ABSTRACT

This dissertation focuses on characterizing and understanding transfer zone growth and geometry. Seismic data including seismic attributes are used to better image transfer zones and understand their structural properties. Coherence shows a strong correlation with displacement for major faults and with the relay ramps. My analysis shows that increases in fault displacement to be logarithmic with the increase in fault length and relay ramp length, such that significant displacement does not result into significant length growth, beyond the initial faulting stage. This is due to the development of relay ramps that not only transfer displacement from one fault to another, but accounts for the increase in displacement through breaching. Similarly, curvature can be used to image folding and bed rotation associated with faulting, with shallower horizons draping across some of the faults exhibiting finite displacement at deeper horizons. Finally, other attributes such as dip and azimuth can help image splay development and breaching within the transfer zones.

I also use seismic data to assess fault sealing potential. To do so, I used seismic inversion methods to invert for rock properties including gamma ray, and porosity, which then can be translated into rock descriptions. Facies juxtaposition within the 3D model allow me to assess areas of sealing and leaking potential. My analysis shows that transfer zones can serve as major migration pathways, where the geometry of the ramp prevents a total fault seal associated with displacement. I also used the SGR method to assess the sealing capacity of those faults. Results are similar to the juxtaposition method, but show a much broader sealing capacity, and in some intervals, a total seal across the major faults and within transfer zones. As transfer zones become breached and heavily faulted, they provide potential migration pathways if fractured, or migration barriers associated with the displacement that the breaching fault undergoes.

Experimental models are analogue models that can be used to better understand the mechanism by which transfer zones develop. In this research, the analogue modeling focused on studying the relationship between pre-existing fault geometry, bed lithology, and transfer zone development. Pre-existing faults, including overlapping faults, can cause the development of a larger “damage” zone characterized by the development of synthetic and antithetic faults. Lithology greatly impacts the growth mechanism and the distribution of faulting around transfer zones. Analysis of the analogue models suggest that harder rocks (modeled by cement) tend to have less folding and rotation of faults, and more significant faulting, while softer rocks (modeled by clay) tend to develop gradually with time and exhibit significant folding and fracturing. These analogue models correlate well to multiple outcrop field studies. Hence this work will focus on seismically characterizing transfer zones, developing new methods to assess their sealing potential, and studying lithological and pre-existing faulting importance on their geometries.

CHAPTER 1: INTRODUCTION

1. TRANSFER ZONE DEFINITION

Transfer zones are ramps that connect two faults (the upthrown block of one to the downthrown block of another one) by transferring displacement from one fault to another. They have been extensively studied to better understand the transfer of fault slip and considered for their importance for fluid migration and fracture distribution on different scales. There are multiple transfer zones types, depending on the relative dip directions of adjacent faults and the distribution of slip along individual faults. Figure 1.1 shows the classification of transfer zones depending on how faults are dipping and their relative position. These include divergent, convergent, synthetic, collateral and colinear transfer zones (Morley et al, 1990).

Convergent and divergent zones are defined by faults dipping in different directions either towards each other (convergent) or away from each other (divergent). Synthetic transfer zones consist of faults that dip in the same direction and are separated by strike or relay ramps (Morley, 1990). Approaching faults initially terminate along strike, commonly branching into a number of smaller faults splays. As the fault-related extension increases, a transfer fault can connect some of the smaller initial faults and result in fully detached blocks (Larsen, 1988). The significance of relay ramps as well as other damage zones is defined by their role in defining traps, reservoirs, migration conduits, or barriers for hydrocarbon exploration.

Many works on transfer zones and their structural characteristics has been published covering mainly fault initiation, observed displacement, and associated folding. Larsen (1988) presented one of the earliest studies on the geometrical and tectonic implications of these structures. His work examined deformation geometry of relay ramps for synthetic extensional faults based on ramp “strength”, strain rate, and the amount of extension. He noted that the relative

location of faults can influence the final geometry of the relay ramp leading to detached hangingwall or footwall relay systems.

Morley et al (1990)'s work presents the first and most detailed classification of transfer zones. As seen in Figure 1.1, the "idealized" classification of a relay ramp in an extensional setting is based on the relative direction and magnitude of throw on the major faults, fault dipping directions, and fault termination. Hence based on the dipping direction, transfer zones can be synthetic or conjugate (convergent or divergent), and based on the extension magnitude and fault termination, each zone can either classified as approaching, overlapping, collateral, or colinear.

Peacock and Sanderson's work published between 1991 and 1995 is a series of publications that investigated the relationship between displacement variations along faults, fault segments linkage, strain estimation, and relay ramps geometries within a normal or strike-slip system. Displacement at a transfer zone is seen to be reduced caused by folding or tilting of beds within the relay ramp while maintaining a constant ramp rotation (Peacock et al, 1990, 1993). This variation in displacement at relay ramps causes a variation in the d-x (distance vs displacement) plots along the geometry of the structure. Hence, Peacock and Sanderson (1991) defined four (4) stages of relay ramp development based on displacement profiles of the two (2) main faults. This definition was later revised and published in 1994 with a more detailed description of relay ramp growth for normal faulting (Figure 1.2). Those four (4) evolutionary stages involve (1) fault initiation, (2) fault propagation, (3) relay ramp breaking and development of a connecting fault, and finally (4) the complete faulting and breaking of the ramp with multiple composite along-strike faults.

In strike-slip settings, relay ramps are characterized by re-oriented bedding between two faults of different direction (Peacock and Sanderson, 1995). In case of any vertical displacement

associated with strike-slip movement, relay ramps transfer that displacement using synthetic and antithetic faults. Similar to an extensional setting, Peacock and Sanderson defined four (4) stages of relay ramp growth defined by: (1) fault initiation, (2) fault propagation and interaction and the formation of small-scale faulting and veining, (3) breaking of the relay ramp and faulting through the ramp, leading to (4) a by-passed fault system defined by a single fault with contractional bend. Similarly, in strike slip settings, Sylvester (1988) observed similar stages for growth for relay ramps from a basin-scale perspective. Sylvester gave a description of pull apart basin geometry in overstepping domains of parallel faults including (1) single subsidence graben, (2) narrow two grabens formation, (3) terminal extension fractures, and (4) sub-parallel faulted mini-basins. This definition is related to the relative magnitude of the depth to basement (defined as D), the spacing between en-echelon faulting (S), and overstepping of faults (O).

2. GROWTH MECHANISM

Understanding the fault growth mechanism is essential to understand transfer zone characteristics. In his work in 2002, Peacock focused on fault initiation and provided a good definition of three-dimensional complex fault geometries consisting of individual fault segments that are interacting with each other in different directions with different displacement amounts. The work explained how faults initiate at a small nucleus that connects into a large one with variable slip, orientation, and plane geometry. This idea was supported by observations of outcrops where variations of brittle vs ductile lithology affects fault growth. Peacock (2002) documented two type of fault growth, the first is initiated in the brittle layers with contractional bends in less brittle rocks, where faults dips are gentler. The second is characterized by overstepping of faults causing the formation of relay ramps in between those faults. The relationships between fault geometries, fault interactions, and accumulation of displacement within a fault were studied using

different models that account for single slip, cumulative slip, fault interactions, propagation rate, fault reactivation, and complex fault networks including pre-existing faulting or reactivation. Similarly, Fossen et al. (2016) defined fault linkage as the result of one of two end member scenarios, either a tip propagation model of randomly distributed small faults, or through coherent growth caused by a pre-existing buried fault being reactivated. This work expands this work presented in 2006 in order to consider ramp length, width, geometric irregularities of overlapping faults, rock ductility, and variation of fault strength. With the tip propagation model, the growth of faults is controlled by different parameters including fault population and distribution, stress orientation and perturbation, the boundary conditions such as weak fabrics or faults, and reactivated basement faults. Because displacement is being transferred from one fault to the other, the spacing of the two faults impacts the length of the ramp. When considering the coherent growth model, Fossen et al (2016) stated that fault reactivation is not only accommodating for major displacement, but for providing an answer to understand fault networks and changes in fault orientation, and variation of displacement along a fault. When considering fault re-activation, larger faults will tend to reactivate first, dictating the location of smaller faults, and accommodating for the formation of new faults based on the new stress state.

Similarly, Walsh et al (2002) suggested that applying kinematic interpretations to 3D models allow for a different understanding of relay ramp evolution and fault propagation. 2D modeling of fault propagation and growth led to the “isolated faults” models that favor growth of faults through linkage of independent faults. However, Walsh et al. (2002) suggests that 3D fault propagation models provides a “coherent fault model” where damage zones are kinematically coherent array that breach as a result of continual displacement or radiation of relay ramps.

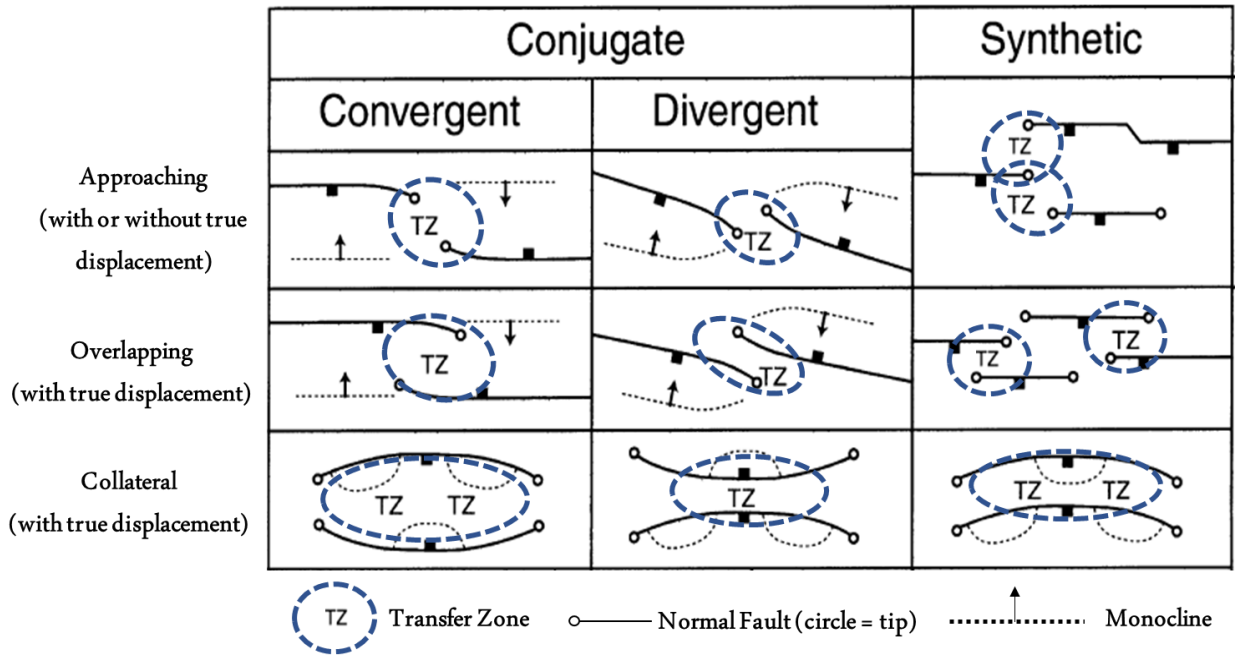


Figure 1.1. Transfer zone classification based on Morley et al. (1990)

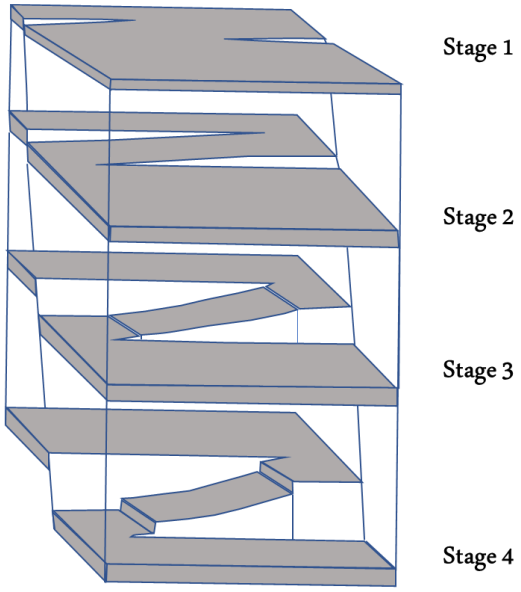


Figure 1.2. Different stages of transfer zone evolution as described by Peacock and Sanderson (1994).

3. RELAY RAMP BREACHING AND FRACTURING

As displacement increases, breaching of the transfer zones may occur. Fossen et al. (2016) presented a comprehensive approach for relay ramp breaching associated with bed tilting and lengthening of the ramp connecting the two faults. Depending on the sedimentary layering, as faulting continues, breaching within the relay structure may occur along with lengthening and bending of beds, causing fracturing and faulting of the ramp. This fracturing is quite important for vertical and lateral fluid movement, migration, or entrapment. The effect of relay ramps on migration was studied and presented by many researchers based on available natural examples. Ferrill and Morris (2000) address the locally enhanced fault and fracture density for brittle faulting such as the Yucca Mountain in Nevada. Those transfer zones present pathways and barriers for fluid movement and flow.

Additional work concerning relay ramp deformation and fracturing was carried out by Ferrill and Morris (2001) using a geometrical model for a normal fault-block based on studies of natural examples. The geometric model would estimate ramp deformation and determine potential pathways or zones of altered permeability or trapped resources. Similarly, as a result of the model developed by Imber et al (2004), it is determined that breaching within relay ramps is associated with the rotation of the ramps until the ramp is faulted and connecting footwall and hangingwall blocks. The model successfully reproduced relay ramp geometries and displacement profiles for natural examples of normal faults cutting through homogeneous sandstone rocks.

Conneally et al (2014) further modified the relay ramp evolution model by determining the geometry and kinematic history of two transfer zones from the South China Sea. It was determined that kinematic analysis using 3D seismic interpretation show that the mechanism of breached zones development might have included the formation of a “through-going” fault followed by the development of splay within the breached zone. This can be seen by the rotation of the ramp which

occurred after the faulting and prior to the formation of splay geometries. The data that Conneally et al (2014) used included an upper and a lower relay zone that were vertically separated by 100m of sediments, thus suggesting causality between the two (2) structures. A possible explanation indicates that the lower relay zone might have been "triggered" the development of the upper ramp due to the complex inherited geometry.

The impacts of pre-existing faults on subsequent fault growth and geometries have been extensively studied. Similarly, transfer zones do inherit the location and complexity of the "parent" faults. This has been shown in many examples around the world including the Gulf of Aden in Yemen (Bellahsen et al, 2013) the Albertine rift in Uganda (Aanyu and Koehn, 2011 and Katumwehe et al, 2015), and Thailand (Morley et al, 2004). Bellahsen et al. (2013) established a classification of fractures zones based the syn-rift structures: type 1 for pre-oceanic spreading, type 2 for during, and type 3 for post spreading. Morley et al (2004) acknowledge the pre-existence of oblique fabrics which have impacted the development of basins and en-echelon faulting in northern Thailand associated with oblique extensions. Sandbox models are great analogues of oblique extension and were thus used to reproduce some of the geometries observed.

Experimental models are types of models that have been used to better describe and understand transfer zones and relay ramp growth and their associated fracturing/faulting. These models used wet clay or sand to model different lithological variations (Dooley and Schreurs, 2012, and Paul and Mitra, 2013) and are aimed at better defining the controlling parameters of transfer zone development. Hus et al (2005) used sand (as brittle) overlaying silicone layers (ductile analogues) in extensional experiments to geometries observed within rift zones. Differential extension is then achieved due to the variation between viscosities of the silicone layers thus producing geometries similar to those observed in differential extension grabens. The

degree of differential displacement between two faults is directly related to the degree of deformation that relay ramps experience, such as major transfer faults developed with larger displacement. Studying the mechanical stratigraphy impact on transfer zones has been done in sandbox experiments and observed in the field. Ferrill and Morris (2008) examined the transfer zones in natural examples from east and south Texas for the Eagle Ford, Buda, and Del Rio outcrops. Those observations lead to the definition of incompetent, mixed, and competent stratigraphic unit deformation. Competent transfer zones are characterized by less tilting of beds and mainly well defined, more vertical faults. Incompetent shows more tilting and rotation of bed dips along with a wider fault zone.

4. SEISMIC APPLICATION

With the improvement and development of seismic interpretation and seismic attributes, studying transfer zones has resulted in a better understanding of ramp geometry and associated faulting and folding. There are different seismic attributes that can be used to help structural interpretation and to better understand fault geometries, slip, and strikes. Coherence allows us to see discontinuities in the data such as faults, fractures, or stratigraphic features such as channels. In addition, curvature shows how bent the curve is or in a 3D setting, it represents the shape of the surface, which can be defined using Gaussian curvature as a cone, ridge, valley, or bowl (Roberts, 2001). Volumetric dip and azimuth are two attributes that can be valuable in interpretation mainly to define local reflector surfaces that show discontinuities or oppositely using those attributes to look for continuity in the data. Corendering different attributes may improve imaging qualities and provide additional geological insights (Marfurt, 2015).

A good example of the application of seismic attributes come from the NW German Basin that is characterized by NS striking normal faults. After interpreting the seismic data, seismic

attributes are then calculated and extracted along the faults. Those attributes are then plotted against structural parameters such as displacement (vertical, horizontal) (work after Lohr et al, 2008). By examining dip, azimuth, and curvature shown in Figure 1.3, it is clear the correlation between the location of transfer zones and the changes in the attributes. The amount of displacement, such as maximum horizontal and vertical displacement match the fault changes. The steeper the fault, the higher the difference between vertical and horizontal displacement (Lohr et al, 2008). Hence using this analysis, the fault morphology can be linked to segmented fault growth associated with heterogeneous deflection and displacement along that fault. Similarly, it can be inferred that areas with smaller displacement can be associated with normal fault drag.

Similarly, Iacopini et al (2016) worked on a large reverse fault in the Parahaki 3D survey in New Zealand, where the analysis focused on relating fault zones to their seismic expressions. Seismic expression of fault zones vary from other regions such that faulted zones tend to have higher coherency and a different envelope response. That work defines areas of high incoherency and relatively low amplitude, associated with high damage, and other areas of low incoherent data associated with low deformation.

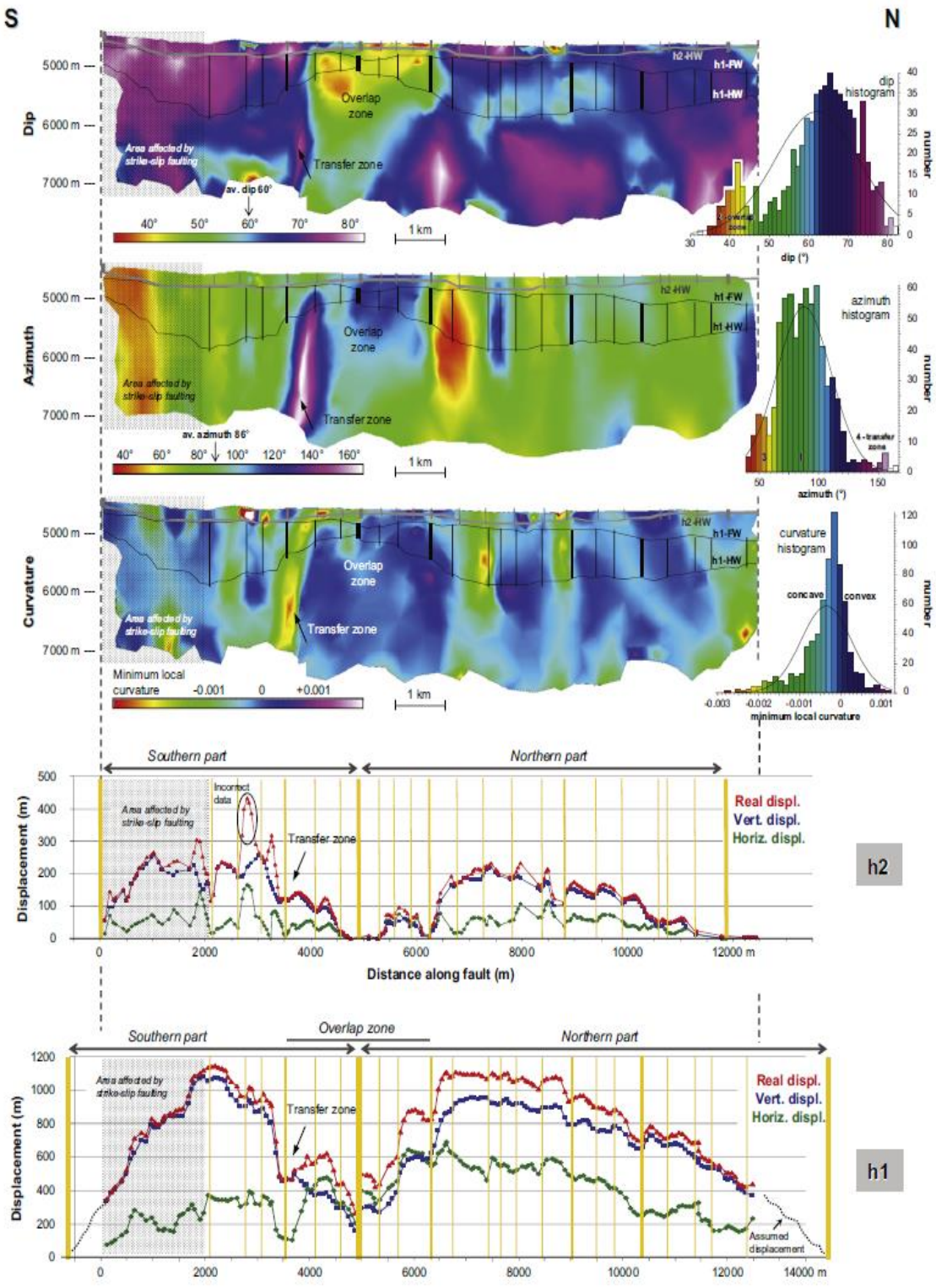


Figure 1.3. Seismic attributes colored along the fault plane, plotted against fault displacement (Lohr et al, 2008).

5. STUDY OBJECTIVES

Despite the work mentioned by Lohr et al (2008) and Iacopini et al (2016) that uses seismic attributes data to understand fault geometries and relay ramp growth, there is still more that can be done to correlate structural parameters to derived seismic attributes. Additional understanding of fault dip, displacement, bed tilting, and fault connectivity can be derived from seismic attributes. Such an understanding can shed light on transfer zone growth mechanisms which as shown, impacts fracturing within relay ramps. In addition, there is limited work using seismic inversion data to assess fault sealing potential and pathway analysis. The work published have relied heavily on 1D or 3D juxtaposition models built using reservoir models with limited seismic impact. Finally, the work presented by Ferrill and Morris (2008) is a great start of natural examples of transfer zones and additional experimental work is needed to assess the mechanical stratigraphy impact on transfer zone growth.

The work presented here will cover the following study objectives:

1- Understanding the expression of structural parameters of transfer zones using seismically derived attributes.

2- Assessing sealing and leaking potential of relay ramps and faults using seismic inversion results.

3- Understanding the implication of pre-existing geometries and lithological variation on the geometry and growth of relay ramps, as well as, the distribution of fracturing across those zones.

The work presented here aims at a providing a deeper understanding of relay ramp growth and transfer zones properties using seismic data, natural examples, and analog modeling.

CHAPTER 2: SEISMIC EXPRESSION OF TRANSFER ZONES

In this chapter, we investigate the geometry and development of relay ramps in the Parihaka fault system in the northern Taranaki Basin, New Zealand. The Parihaka fault system is defined by a series of en-echelon faults forming a synthetic transfer zone. Major and secondary faults and associated relay ramps are generally well imaged by traditional 3-D seismic amplitude data. We first use traditional 3-D seismic interpretation to study the geometry of the synthetic transfer zone and related relay ramps. Displacement patterns on individual faults and at relay ramps are mapped for different units to understand the evolution of the transfer zones. We then use three seismic attributes, namely, coherence, curvature, and dip and azimuth, to study the deformation patterns on the major faults as well as related folds and secondary faults. The results provide a better understanding of the deformation patterns within the transfer zone, and also serve as a test for the use of attribute analysis in transfer zone analysis.

1. INTRODUCTION TO THE TARANAKI BASIN

The Taranaki Basin is a Cretaceous sedimentary basin encompassing approximately 100,000 square kilometers located off the western coast of New Zealand. It formed as an active volcanic back-arc rift basin (Giba et al., 2010) during the subduction of the Pacific plate beneath the Australian plate (Haque et al., 2016; Rajabi et al., 2016). The formation of the basin is defined by three stages: an extensional phase that occurred from the late Cretaceous to the Paleocene time characterized by the formation of graben and horst structures along a N-S normal faulting system (King, et al., 1996; Giba et al., 2010), a shortening phase primarily confined to the southern part of the basin caused by the subduction of the Pacific plate, and another extensional phase starting in the late Miocene occurring in different locations (King, 2000; King et al., 1996). Subsidence increased significantly between 30-25 Ma (King et al., 1996), induced by mantle convection as

subduction continued on the eastern side (Stern, 1994). Gradual southward and eastward migration of volcanism and faulting is evident around 18 Ma due to the rollback of the Pacific plate (Giba et al., 2010; King, 2000; Nicol et al., 2007).

The sedimentation rate within the basin is determined to be higher than the fault displacement rate, resulting in preservation of units in both blocks and thickness increases across the faults into the downthrown blocks. Sediments were deposited in the basin in large volumes due to the erosion of areas with positive relief (King, 2000). Within the South Taranaki Basin (STB), the vertical displacement rate was the largest during the late Cretaceous (Reilly et al., 2015). The sedimentary record from the northern Taranaki Basin indicates significant displacement around 29 Ma seen by the activation of the Manganui fault (Tripathi and Kamp, 2008). Understanding the deformation history of this area is key to understanding faulting observed in the Parihaka area.

The Parihaka fault studied in this paper is located in the northern central part of the Taranaki Basin, and underwent normal faulting. The fault system is about 50 km long and comprised of five segments forming an en-echelon system (Figure 2.1), striking north-south to northeast-southwest (Giba et al., 2012). According to Giba (2012), the fault has up to 1.8 km of vertical displacement with the maximum displacement shifting to the north during Plio-Pleistocene time, while becoming almost inactive in the southern part. The minimum displacement on the faults coincides with the locations of the relay ramps.

Giba et al (2012) discussed the fault growth history considering the pre-existing faulting which was active during the Miocene age. The Pliocene faults are seen to have a different orientation compared to the deeper faults possibly due to changes in extension direction. This confirms a complex structural history of the Parihaka fault compromised of Late Cretaceous to

Early Eocene extension towards the southern part of the basin, and an irregular displacement distribution during the Plio-Pleistocene time (Giba et al 2012).

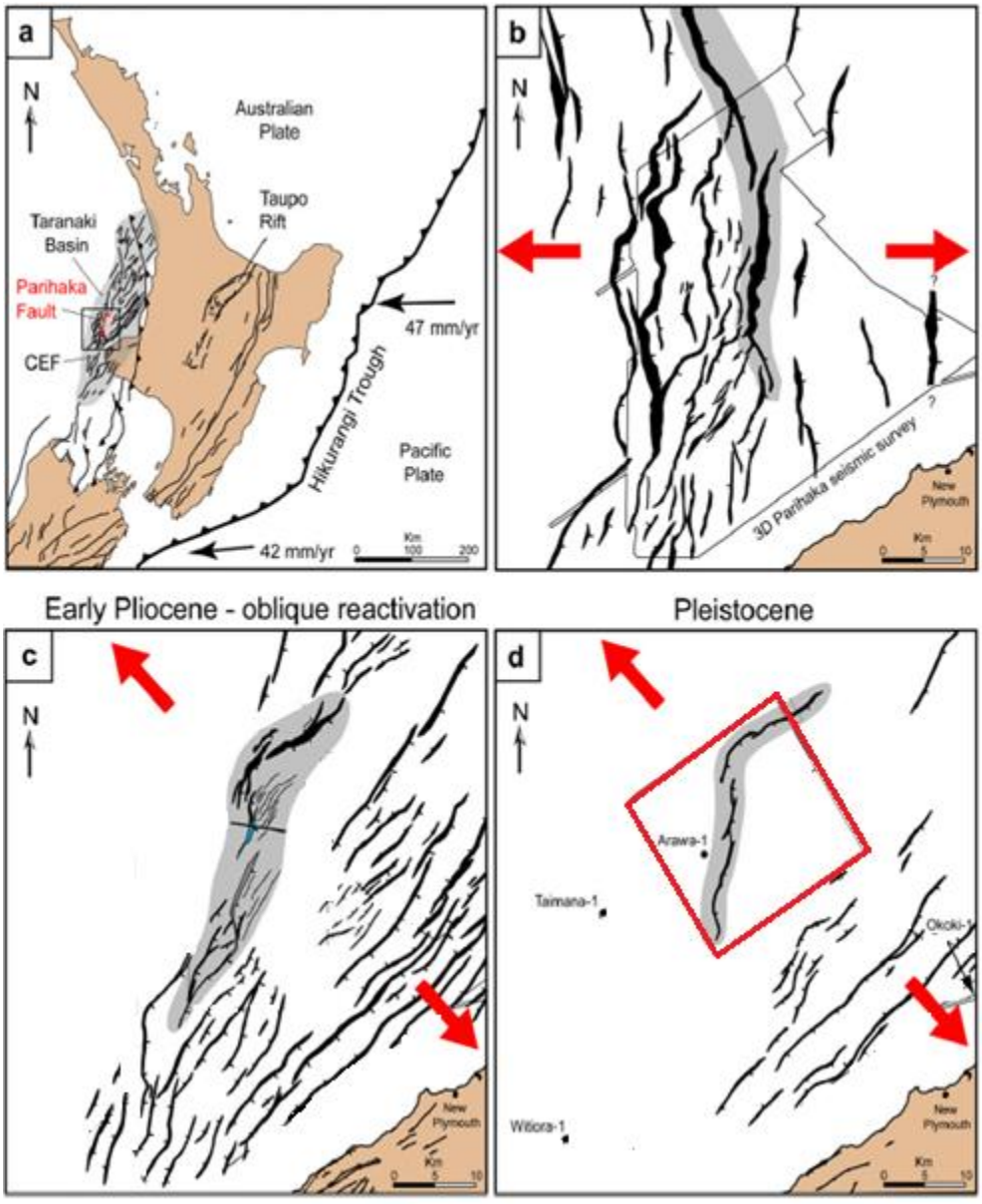


Figure 2.1. Plate boundary setting of the North Island in New Zealand. (a) Regional setting during the Late Cretaceous (b) Zoomed in look at the region during Late Cretaceous (c) Parihaka fault during the Early Pliocene (d) Parihaka fault during the Pleistocene (edited from Giba et al. 2012).

2. DATA AND INTERPRETATION METHODS

A 3D poststack time-migrated seismic volume for the area west of New Zealand covers a large area of the Parihaka fault. The seismic volume was provided through the SEG data storage facility and covers most of the three en-echelon faults connected by relay ramps. In general, the seismic quality is good mainly in the section covering the faulting system. Seismic acquisition footprints contaminate the shallower portion of the data but does not significantly inhibit a good interpretation of faulting, folding, and stratigraphic features.

The seismic volume was reprocessed in 2012 for the purpose of improving the Miocene target, better image the deeper targets west of the Cape Egmont fault, the top of the basement, the Cretaceous geology, the shallow biogenic gases in the North, and the geohazards. This was accomplished by reformatting field data, converting the source signature to zero (or minimum) phase, noise removal and anomalous amplitude attenuation (AAA), linear noise attenuation using Tau-P filtering, removing water-layer reverberations using modified Surface Multiple Prediction (SMP) process, estimating and removing surface multiples using Surface Related Multiple Estimation (SRME), filtering the noise using adaptive filter process, and finally by analyzing the velocity. The velocity analysis included NMO of processed CMP gather data using Multi Velocity Function (MVF) and velocity semblance analysis to ensure consistent velocity interpretation. Once velocity analysis was completed, a series of additional noise cancellation processes were conducted including weighted least squares Radon Multiple attenuation, overburden compensation developed for the specific needs of the South East Asian shelf basins by WesternGeo, inverse Q compensation filter based on the Futterman frequency-constant Q model of earth attenuation, coordinates transform, regularization using Compact Fourier Interpolation (COMFI) allowing wavenumber scanning to determine optimum operator for each output location, Spatially Relative Amplitude Compensation (SRAC) to smooth sudden changes in amplitude, Kirchhoff Isotropic

Pre-stack Time Migration, Density Velocity Analysis (DVA), residual weighted least-squares Radon demultiplex, and finally the residual trim static corrections using Full Offset Residual Trim (FORT) (according the New Zealand Petroleum & Minerals processing report).

Well data including logs, checkshots, core descriptions, mud log reports, drilling reports, geochemistry, and other data were available for three wells in the area. Only one of the wells (Arawa #1) available falls within the 3D seismic volume that covers the interpreted intervals. The well data were used to correlate key units in the seismic data. Checkshot data served as the main input for the velocity model and for the depth migration piece, while as tops, correlated to available bio-stratigraphic unit from the rocks collected were then matched to interpreted seismic horizons and provided an estimate on the timing of the structural events.

Structural analyses of the synthetic transfer zone consisted of two main components. The first component consisted of a traditional approach of analyzing the transfer system including a three-dimensional analysis of the fault zones, the variation of slip both on individual faults and along relay ramps connecting the individual faults. Figure 2.1 is a map showing the location of the three main faults offshore New Zealand interpreted within Pleistocene to Pliocene units. Figure 2.2 represents a map view of a time slice at t=860ms through a coherence volume. The coherence displayed is a measure of how coherent the seismic response is thus allowing to pick and determine areas of variability which then reflects the presence of discontinuity. The darker continuous colors, trending mainly north south, are the major en-echelon faults in the area defined in this chapter as Fault A, Fault B, and Fault C. Ramp 1 is defined as the ramp connecting Faults A and B while Ramp 2 is defined as the ramp connecting Faults C and D. Note the location of the Arawa #1 well on the upthrown side of Fault A in close proximity to Ramp 1.

The second component consisted of seismic attribute analyses to refine the fault interpretation and the related deformation in the vicinity of the relay ramps. This analysis included the use of variance (coherence), maximum positive and negative curvature, seismic dip, and seismic azimuth. We conducted our analysis using time slices as well as horizon slices through the attribute volumes. In contrast to time slices through the original seismic amplitude, time slices through the dip, curvature, and coherence volumes are relatively insensitive to the seismic wavelet and are thus quite easy to interpret on time slices.

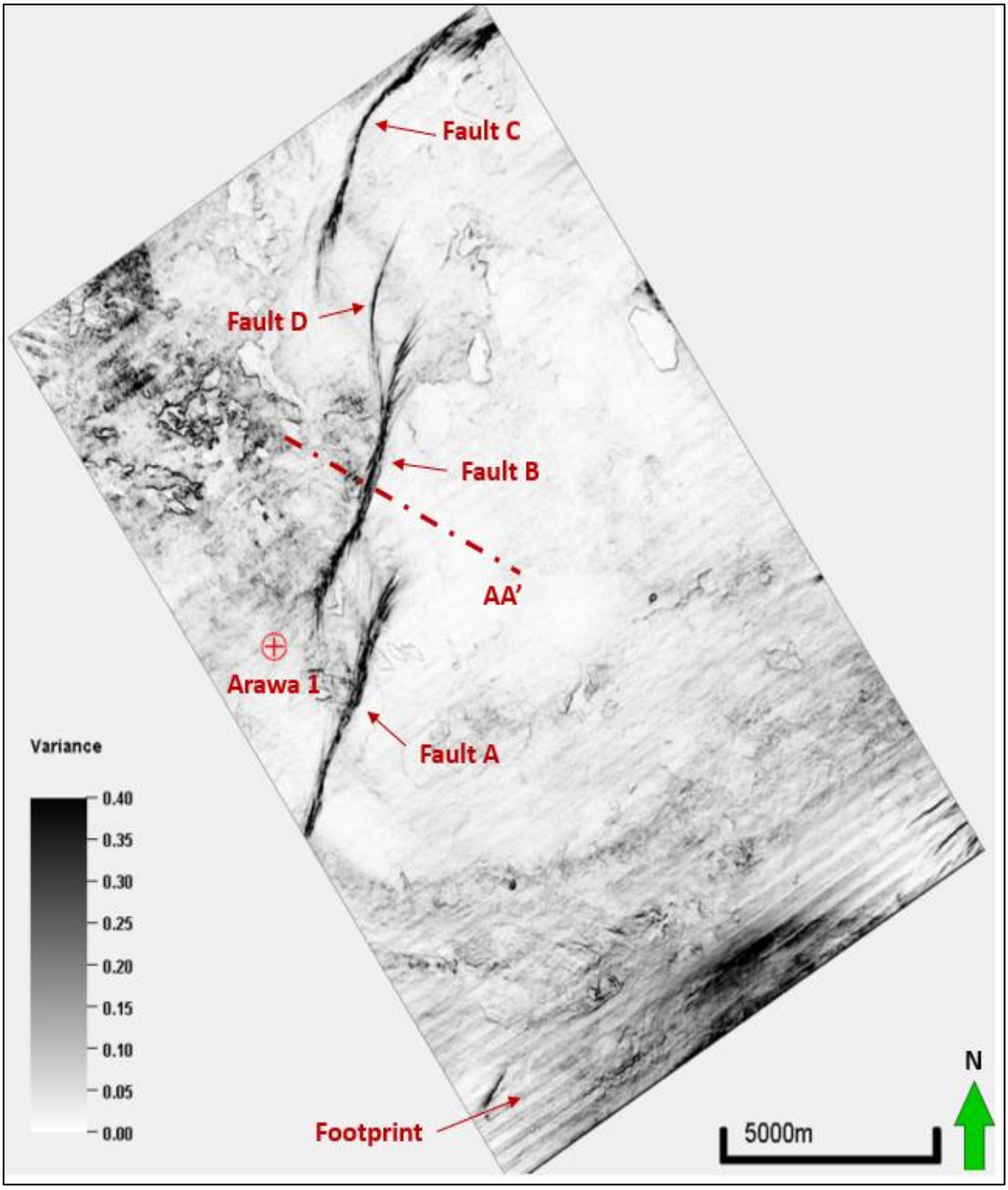


Figure 2.2. Time slice at t=860ms through a coherence volume showing the location of the main faults in the area (A, B, C, and D), the Arawa 1 well, and the location of cross-section AA'. The NE trending acquisition footprint corresponds to the sail line of seismic acquisition. High coherence elliptical features are shallow gas accumulations forming bright spots which can be seen in the following figure.

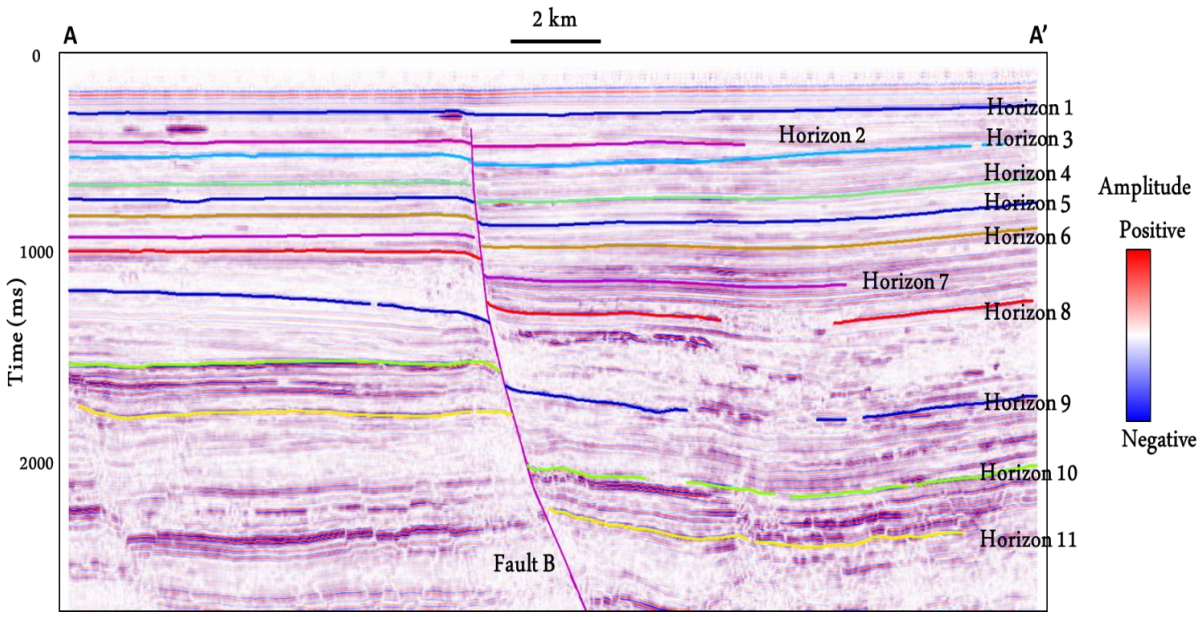


Figure 2.3. Cross-section AA' showing all 11 horizons interpreted to assess relay ramp formation.

3. FAULT CHARACTERIZATION

A time-depth conversion based on one well (Arawa 1) was used to better interpret the structure and related faults with depth. The data show an overall consistent increase in velocity with depth. The model was separated into three velocity trends to accommodate for velocity changes with depth and a more accurate depth conversion. Figure 2.4 shows the velocity data from the Arawa #1 well plotted with depth for the checkshot data. Different colors represent different defined trends in the velocity model that was adopted during the depth conversion.

Examining Figure 2.3, Horizon 1 shows almost no displacement across the fault, with the displacement increasing to a maximum at Horizon 11. Approximate ages of the horizons was determined using biomarker data shown in Table 1. The downthrown units associated with extension show growth, or increases in thickness compared to the upthrown units. Similar observations on other faults indicate that the region was structurally active as a part of the extensional system during the deposition of those units. Figure 2.5 shows the variations in

displacement along the length of Fault B. For each unit the displacement decreases from a maximum in the center of the fault to a minimum at the fault tips, suggesting an increase in fault displacement with increasing lateral fault propagation. It also shows the progressive increase in the maximum displacement of each unit with depth implying a progressive increase in growth. The increase in separation of the curves between Horizons 8 and 10 suggests a rapid increase in growth during the deposition of the units.

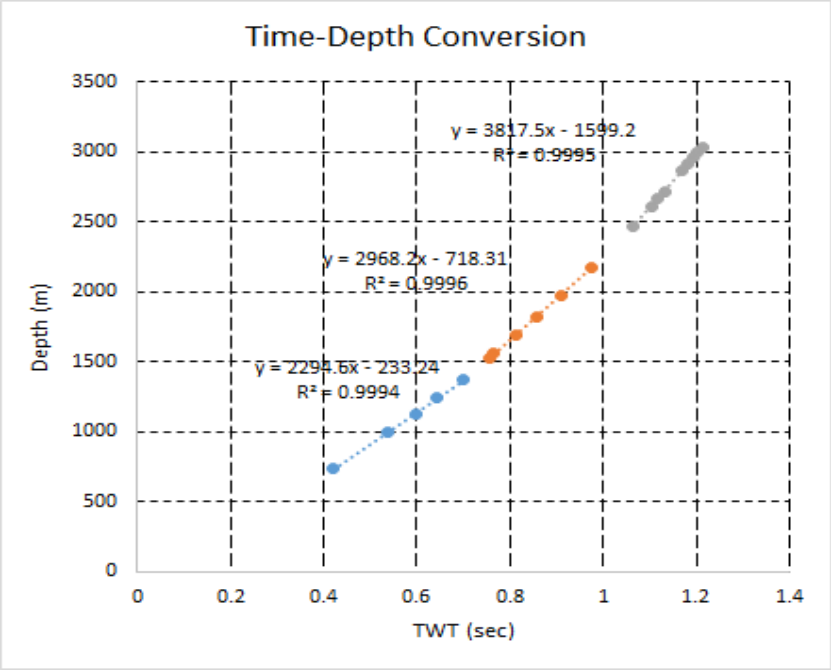


Figure 2.4. Time-Depth conversion chart from the well data within the seismic survey.

By measuring the thickness change at maximum displacement locations across the three main faults A, B, and C, we compute the growth index, defined as the ratio of hanging wall to footwall thickness (Thorsen, 1963), to assess the relative growth associated with each horizon for each of the three main faults (A, B, and C). Figure 2.6 summarizes the findings for the main faults at all eleven (11) horizons. The growth index increases from Horizon 1, showing lower growth, to Horizon 7, which has higher growth. Horizons 1 to 5 are Pleistocene, whereas Horizons 6 to 11

are Pliocene in age. Minor changes in relative growth are seen for the different faults for these horizons.

Table 2.1. Approximate age of horizons based on biomarker data from Arawa 1.

Horizon	Approximate Age (Ma)
1	0.3
3	0.5
4	1
5	1.3
6	1.5
7	2.4
8	2.7
9	3.1
10	5
11	11

During deposition of geologic units underlying Horizons 8 to 10, the growth index for the different faults varies considerably suggesting changes in extension along the fault system. Furthermore, while the growth index is highest for Fault A for units 8 to 9, it is highest for Fault C for units 9-10, suggesting transfer of displacement along trend from Fault A to Fault C during this time.

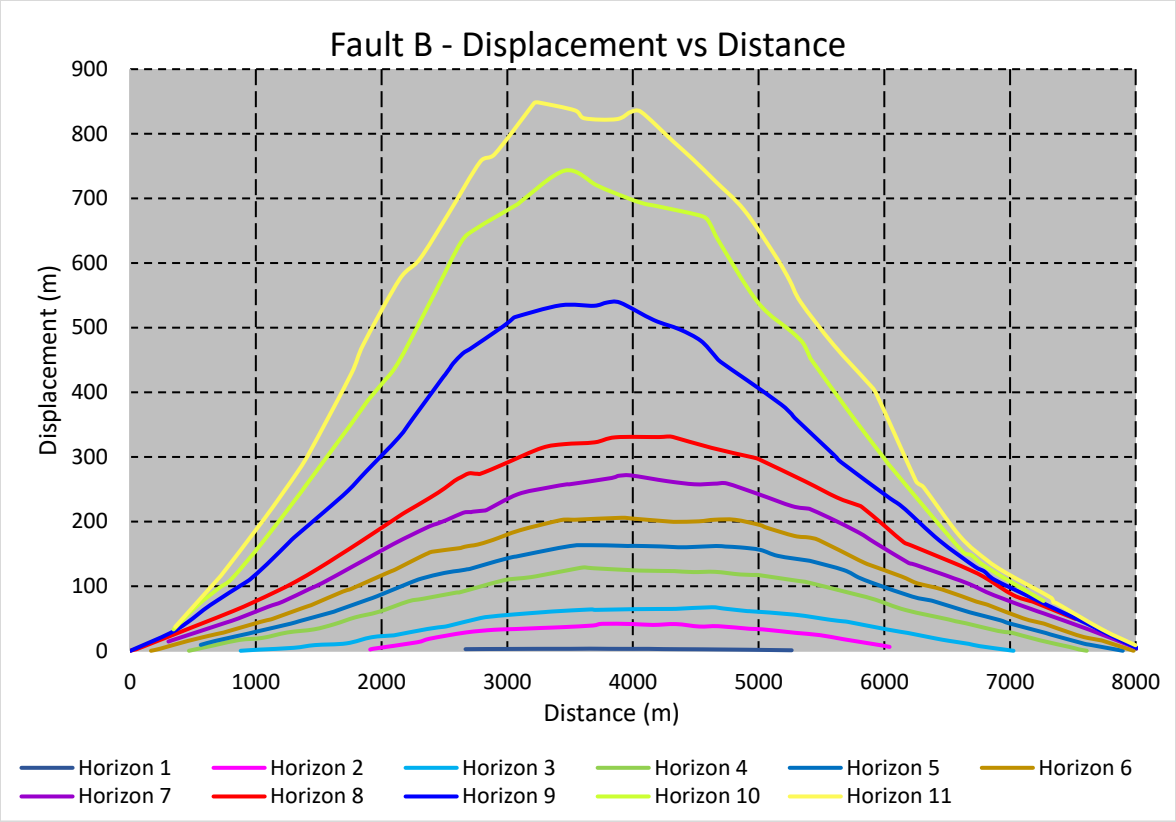


Figure 2.5. Displacement profile for all horizons for fault B.

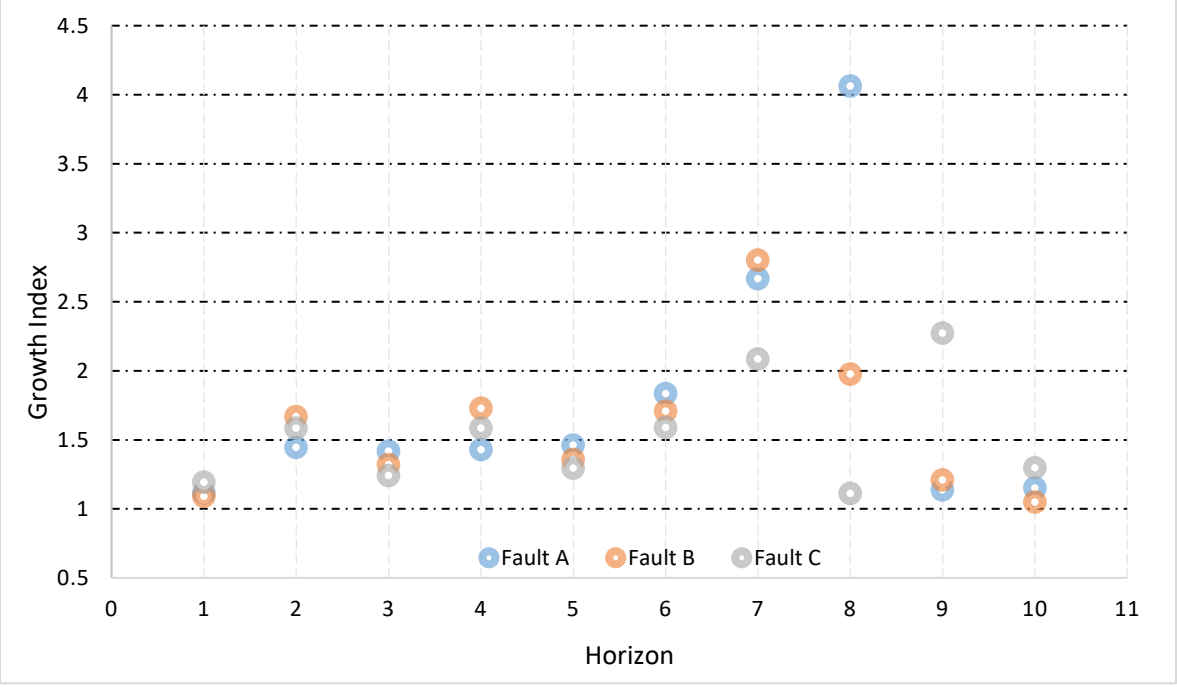


Figure 2.6.Growth index (ratio of downthrown to upthrown thickness) for all three (3) faults.

Another key parameter analyzed was the relationship between fault length and displacement during propagation of each major fault through the major mapped horizons. Fault length was measured at each horizon and plotted along with displacement for all four (4) faults shown in Figure 2.2.

Figure 2.7 shows the fault length versus displacement for every horizon. Shallower horizons (starting with Horizon 1) show shorter fault lengths compared with the deeper horizons, due to the progressive increase of fault length with increasing displacement. However, the rate of change of fault displacement shows three distinct trends: (1) an "early" episode of rapid fault length increase characterized with little displacement, (2) a "second" episode characterized by a rapid increase in fault displacement associated with little or small increase in fault length, and (3) a final episode of fault length increase with small fault displacement. These changes in the rates of displacement with fault length can be attributed to two main factors: (1) the general change in fault displacement with length during the propagation of the faults as discussed by Rotevatn et al (2018), and (2) changes in the rates of propagation caused by variations in mechanical properties of the individual units.

Rotevatn et al. (2018) discusses two fault growth models consisting of (1) a propagation model or an isolated fault model where the fault displacement is positively related to the fault length, and (2) a constant length model in which the faults establish most of their length early on in their history and displacement accumulates without major increase in fault length. The plot of the four (4) faults (Figure 2.7) can be explained due to rapid fault growth in the early stages of evolution (Rotevatn et al., 2018), but also to changes in fault propagation rates due to variations in the mechanical properties of the units.

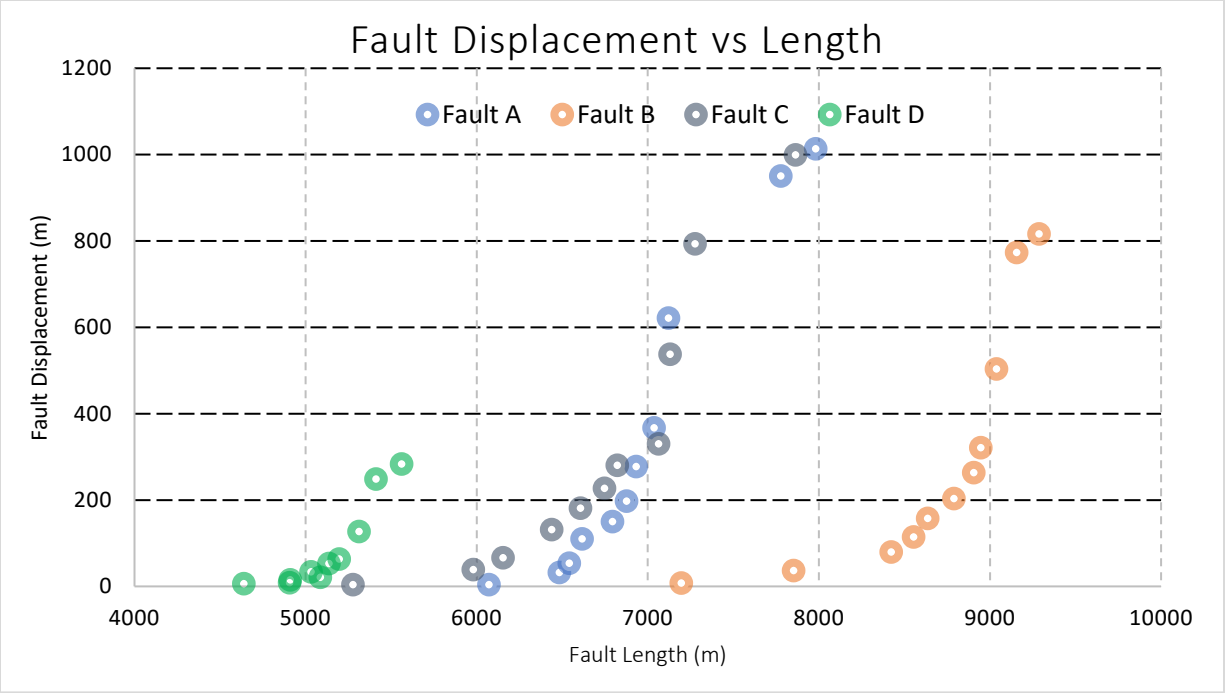


Figure 2.7. Fault length plotted versus fault displacement of all horizons for the four (4) major faults.

4. RELAY RAMP CHARACTERIZATION

We now examine the variation in displacement along the ramps and transfer zones for the different horizons. Figure 2.8 is a cross-section along the faults from the southwest to the northeast in the area. The cumulative displacement at any point along the cross-section for all interpreted faults is plotted. The plot shows the displacement variations for four (4) representative horizons (Horizon 4, 8,10, and 11).

For each major fault and related secondary faults, the displacement is at its maximum in the center of the fault and decreases to a minimum along the transfer zones. There is an overall decrease in fault displacement to the north east for the deeper horizons 10 and 11 (late Miocene and Early Pliocene age). For Horizon 8 (Pliocene age), the decrease in displacement to the northeast is smaller than that for the deeper horizons. The displacement pattern reverses for the shallowest mapped horizon (Horizon 4) for which there is a slight increase in displacement to the

northeast. This pattern can be seen as well in the growth index measurement in Figure 2.6 and may be associated with the change in the relative extension direction during the Pliocene or changes in depositional settings during that Early Pliocene time.. Similar observations regarding the variation in displacement were also made by Giba et al. (2012) for this area and by Lohr et al. (2008) in the NW German Basin.

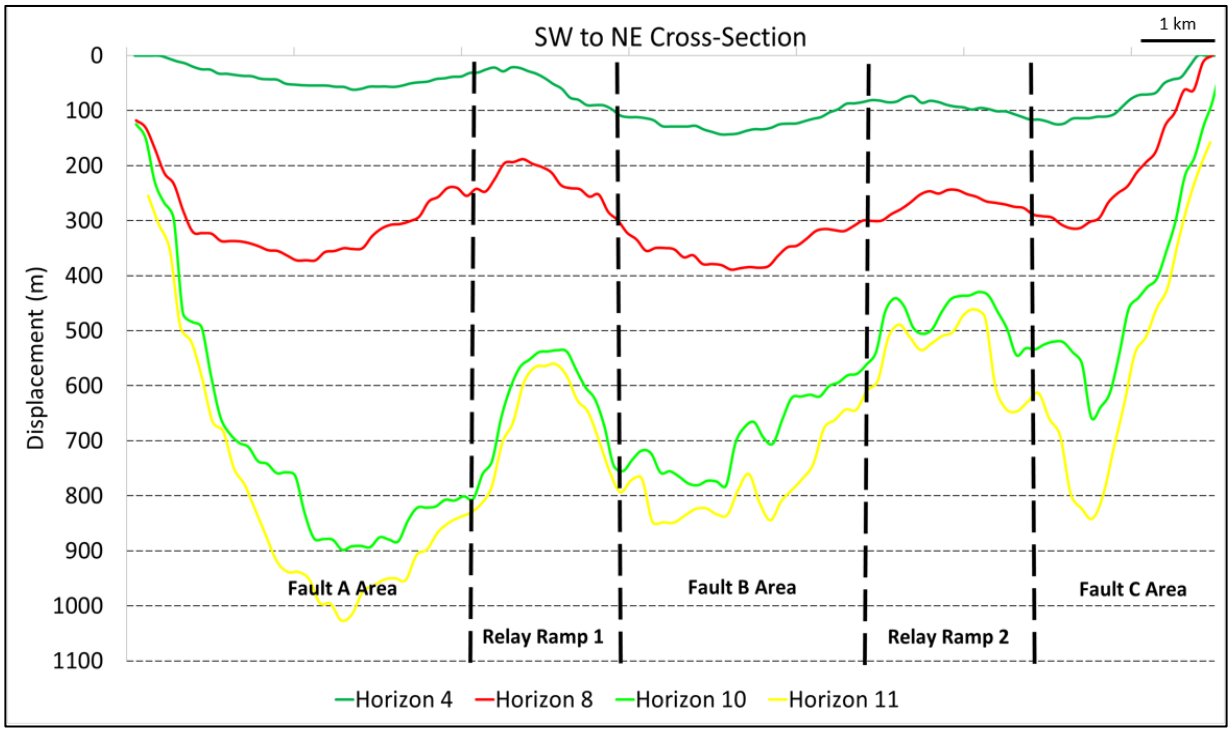


Figure 2.8. Cross-section along the main faults extending from the SW to the NE direction showing displacement for four (4) main horizons.

Relay ramps can be seen in time slices particularly for shallower horizons (from Horizon 1 to Horizon 7). With an increase in displacement, relay ramps are often cut by small faults, which connect the major faults, thus making it more difficult to examine displacement transfer. Ramps connecting the different faults were examined by recording ramp length and width and plotting them against the maximum displacement observed on both faults defining the ramp. Figure 2.10 shows the relay ramp length increasing with the increase of displacement at every horizon for both

connected faults. For Faults A and B, the maximum displacement is similar causing almost identical data points relating displacement to the ramp length for ramp 1, whereas Fault C shows slightly smaller fault displacements and related ramp lengths for Ramp 2. Fault D is a much smaller secondary fault associated with Fault B and shows the smallest fault displacements.

The relationship between the displacements and lengths of Ramps 1 and 2 follow a logarithmic pattern, characterized by a sharp increase in ramp length, so that the majority (70% to 80%) of the length is attained with small displacement (less than 25% extension), followed by a flatter curve associated with small additional increases in ramp length with additional extension. Similar to fault growth seen in Figure 2.7, the logarithmic pattern in relay ramp length increase is associated with a similar logarithmic increase in fault length (Walsh and Watterson, 1988). Since ramp length is related to the length of the fault, the flatter curve supports that fault propagation occurs at a higher rate in the early stages relative to the fault displacement. For Ramp 1 (connecting Fault A and B), the plateau level in ramp length is achieved at Horizon 4, while as that for Ramp 2 (Fault B and C) corresponds to much deeper formation, probably around Horizon 6 or 7. This change in ramp length behavior is seen to match the appearance and development of breaching faults that connects those faults, such that breaching of Ramp 1 extends to shallower intervals (Horizon 4), compared to Ramp 2. Hence as ramps are breached, the additional displacement on the fault is transferred into displacement along breaching faults rather than an increase in fault and thus ramp length.

The ramp width, shown in Figure 2.11, is independent of the increase of displacement for both ramps. The ramp width is defined by the initial location of the faults relative to each other and is possibly controlled by the location of pre-existing basement faults. The ramps quickly extend in length, as adjacent faults transition from approaching to overlapping patterns, eventually

curving and connecting with each other or terminating against each other. The growth history of faults is associated with a significant gain in fault length in the initial stages and then a smaller gain in length with the increase in displacement. Ramps transfer the additional displacement from one fault to the other without significant additional fault growth. The computed ratio of relay ramp Length/Width is then a function of the ramp length since the width of the ramp is considered constant. By examining the computed ratio for horizons post breaching, Ramp 1 averages a ratio around 2, and Ramp 1 averages a ratio around 1.5. Those numbers are significantly lower than what was reported in literature of a ratio of 3 to 3.5 (Fossen et al, 2016).

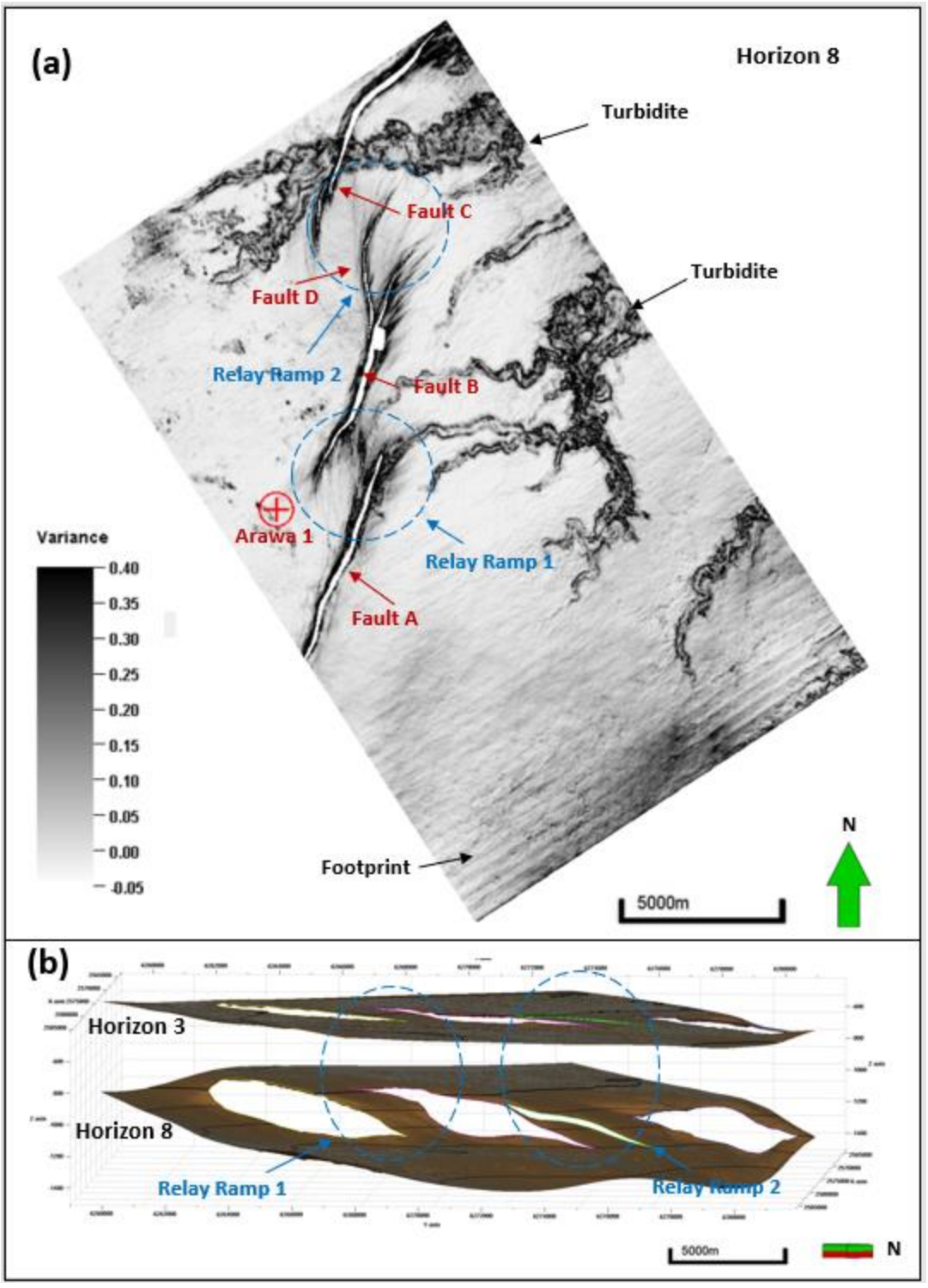


Figure 2.9. (a) Slice along Horizon 8 through the variance volume showing the location of the relay ramps (1 and 2) (b) 3D visualization of the relay ramps as seen in Horizons 3 and 8.

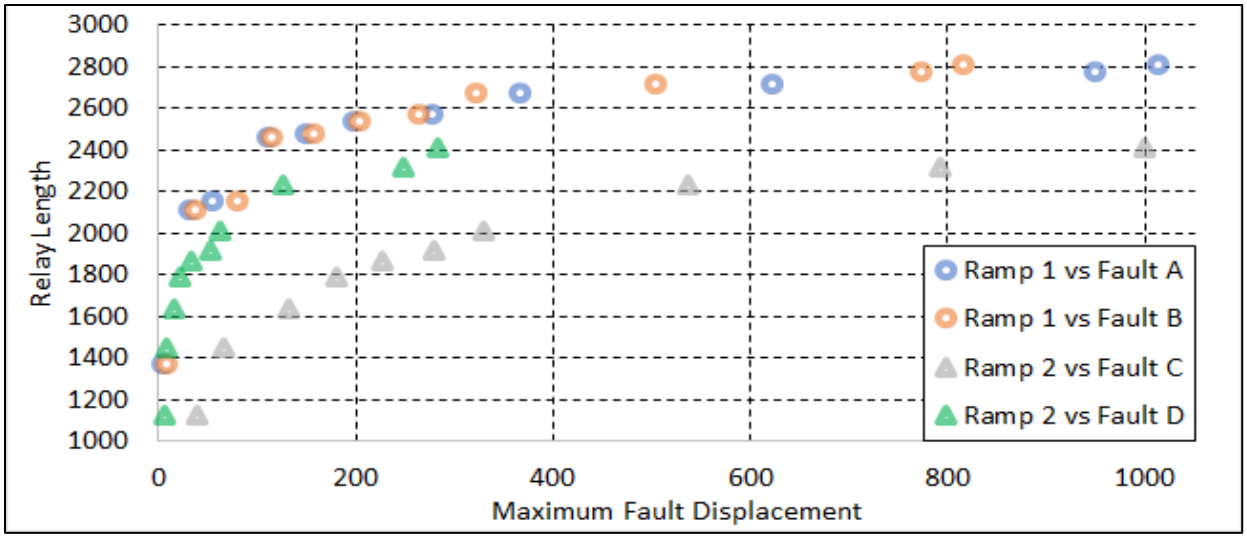


Figure 2.10. Measured ramp length plotted against maximum displacement associated with the related faults.

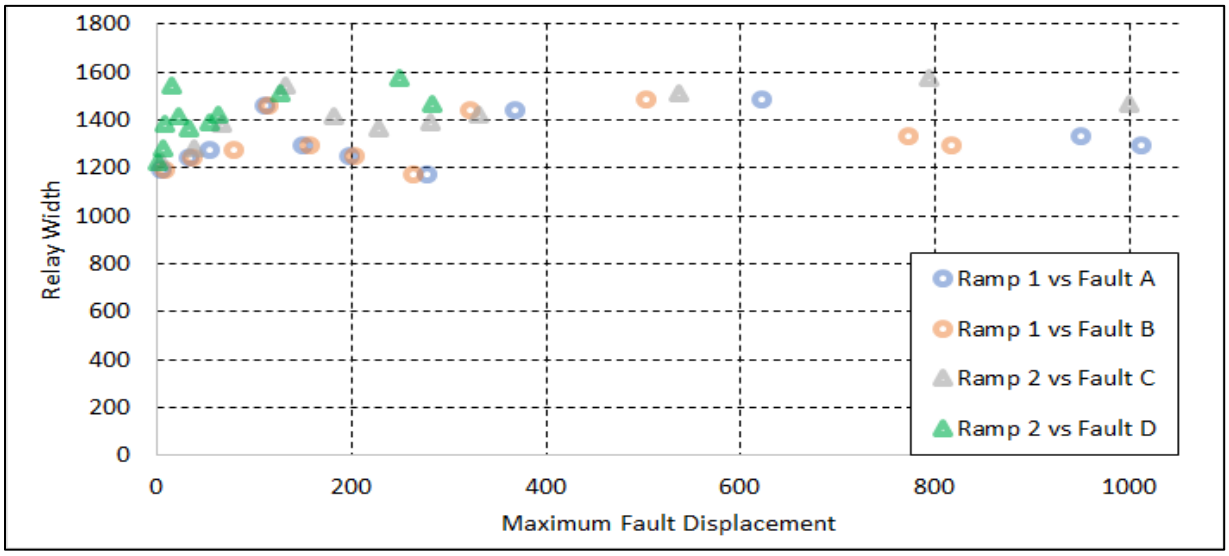


Figure 2.11. Relay ramp width plotted with maximum displacement for all four (4) faults at every horizon

5. SEISMIC ATTRIBUTE ANALYSIS

Seismic attribute analysis was used to understand the detailed geometry of faults and related deformation within the transfer zones. Different seismic attributes can be used to help structural interpretation and to better understand fault geometries and displacements. The attributes

provide a better visualization of the faults, and in some instances, reduced ambiguity in fault location than the original seismic amplitude volume. We summarize the main attributes used in our analysis, including coherence, volumetric dip magnitude and dip azimuth, and most-positive and most-negative curvature.

The dip magnitude and dip azimuth volumes define the orientation of a plane that best presents the seismic reflection pattern at each voxel in the data volume. For time-migrated data, the dip magnitude is measured in ms/m which through the use of a simple velocity model can be converted to degrees. Using 3D visualization and appropriate color bars, horizon slices and time slices through vector dip provide easy to understand images of structural deformation.

Coherence measures the similarity of the waveform within a small 3D window (Bahorich et al., 1995), providing better visualization of discontinuities in the data such as faults, large fractures, and stratigraphic edges (such as the turbidites). By using a small 3D analysis window, coherence provides excellent images of faults on time slices whereas faults parallel to bed strike are easily confused with stratigraphic changes (Bahorich et al., 1995). An eigenstructure coherence algorithm can be applied to produce better results and improve image quality to account for noise and low signal to noise ratios (Gerszentkom et al., 1999).

Curvature is a second order derivative of the time structure, or the first derivative of vector dip. Whereas vector dip can be expressed by a single vector, curvature requires two vectors – the value and the strike of the most-positive and most-negative curvature. Used together, these two vectors provide a representation of domes, ridges, saddles, valley, bowls, and planes within the data volume (Roberts, 2001). Curvature anomalies tend to bracket, rather than align with coherence anomalies. For normal faults, there is usually a positive curvature anomaly on the footwall side of the fault and a negative curvature anomaly on the hanging wall side of fault. In

our present study, this attribute can be used to identify folding of different wavelengths in addition to the faults. Overlaying the most positive and most negative curvature on a time slice enables the visualization of folds, faults, and other structural features. The most positive and negative curvatures are always orthogonal and shows anomalies along the fold crests or troughs (Marfurt, 2010).

6. APPLICATIONS OF SEISMIC ATTRIBUTES

a) Horizon-Based vs Volumetric Dip Calculations

Seismic dip (Marfurt, 2006) was derived and mapped for all interpreted horizons. In addition, dip was calculated by structural modeling and depth conversion for all interpreted horizons. Figure 2.12 presents a comparison between seismic dip and structural dip for various horizons for the two (2) ramps. As seen in the figure, derived seismic dip can be very close to the actual structural dip calculated for the interpreted horizons.

Along relay ramps, the dip of the beds changes along the ramp from the upthrown side of one fault to the downthrown side. Bed dips increase from sub-flat to more dipping to sub-flat again. The dip change relates to displacement transfer along the ramp.

To examine the relation of bed dipping (tilting) with fault development along relay ramps, multiple images of dip change for different horizons were examined. Considering the similarity of seismic dip and structural dip along the ramps, Figure 2.13 shows seismic dip attributes along the ramps. As beds rotate by 5 or 6 degrees, the ramps develop smaller faults to account for the additional tilting on the ramps. The actual dip angle for the fault initiation can be formation specific and depends on the lithological characteristics.

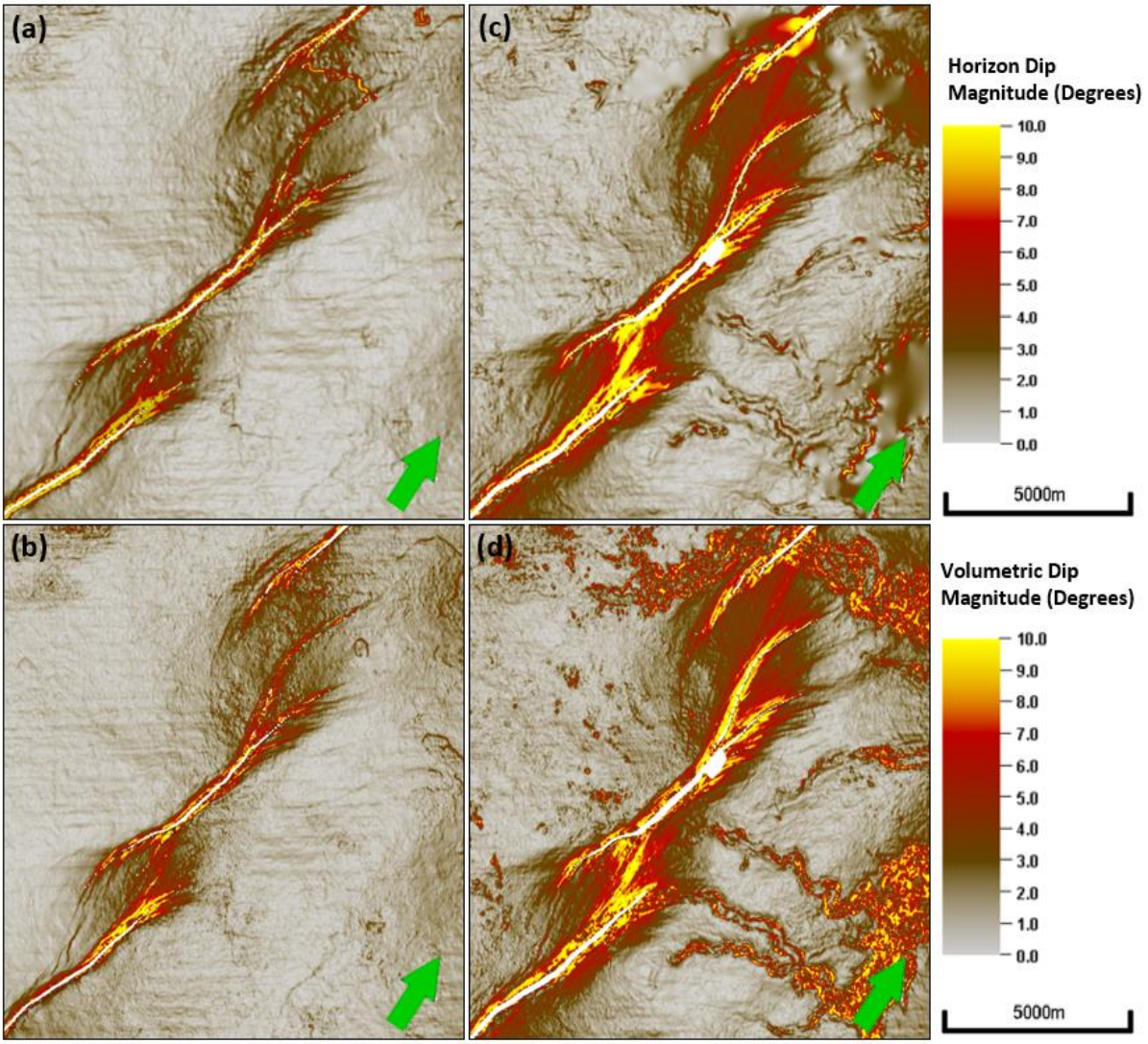


Figure 2.12. Comparison between dip magnitude computed from an interpreted horizon and a horizon slice through a volumetric dip computation for Horizon 6 (a) and (b), and for Horizon 8 (c) and (d) respectively (mapping grid size is 100 m × 100 m). Note the improved resolution of the three turbidite channels in (d) vs. (c). The subtle left-to-right corrugations are due to acquisition footprint.

For Ramp 2, the breaching occurs at a deeper formation and the same Horizon (5) that is faulted at Ramp 1 does not show any faulting at Ramp 2 (Figure 2.14). Breaching initiates between Horizons (6) Horizon (7). Similar to Ramp 1, that breaching is associated with a dip angle of almost 6 degrees. The deeper breaching is because Fault D does not have as much displacement

as Faults A, B, and C. The dipangles of breaching are as well significantly smaller than the number reported by Fossen et al (2016) of 10-15 degrees, which could be a function of lithology.

b) Coherence or Variance

Coherence is an effective tool for visualizing structural changes in seismic data. Although eigenstructure coherence shows the stratigraphic and hydrocarbon edges better, in this application, variance (1-semblance) shows improved delineations about the fault tips where there is no change in waveform shape, but only a change in amplitude. Figure 2.15 shows slices along Faults A, B, C, and D through the variance volume, followed by averaging within a 50 ms window. The changes in color represent the changes in variance along the fault such that red colors indicate a higher variance (less coherent reflectors). A variance of 0 (zero) indicates coherent reflectors with no faulting, whereas a variance of 1 indicates a totally incoherent seismic signal within the analysis window. The observed changes follow the changes in displacement on the faults. Figure 2.16 shows the increase in displacement towards the bottom-center part of the faults which is consistent with the overall increase in variance. Figure 2.17 shows the changes in heave measurements along those same faults, showing a better match with the variance derived from seismic. Along the plane of maximum displacement at every fault location, average variance was measured for every interpreted horizon and plotted with maximum displacement in Figure 2.18. The increase of displacement is consistent with an increase in variance observed particularly for variance below 0.5. Therefore, variance can be used as a direct measure of fault displacement or fault heave for seismic data.

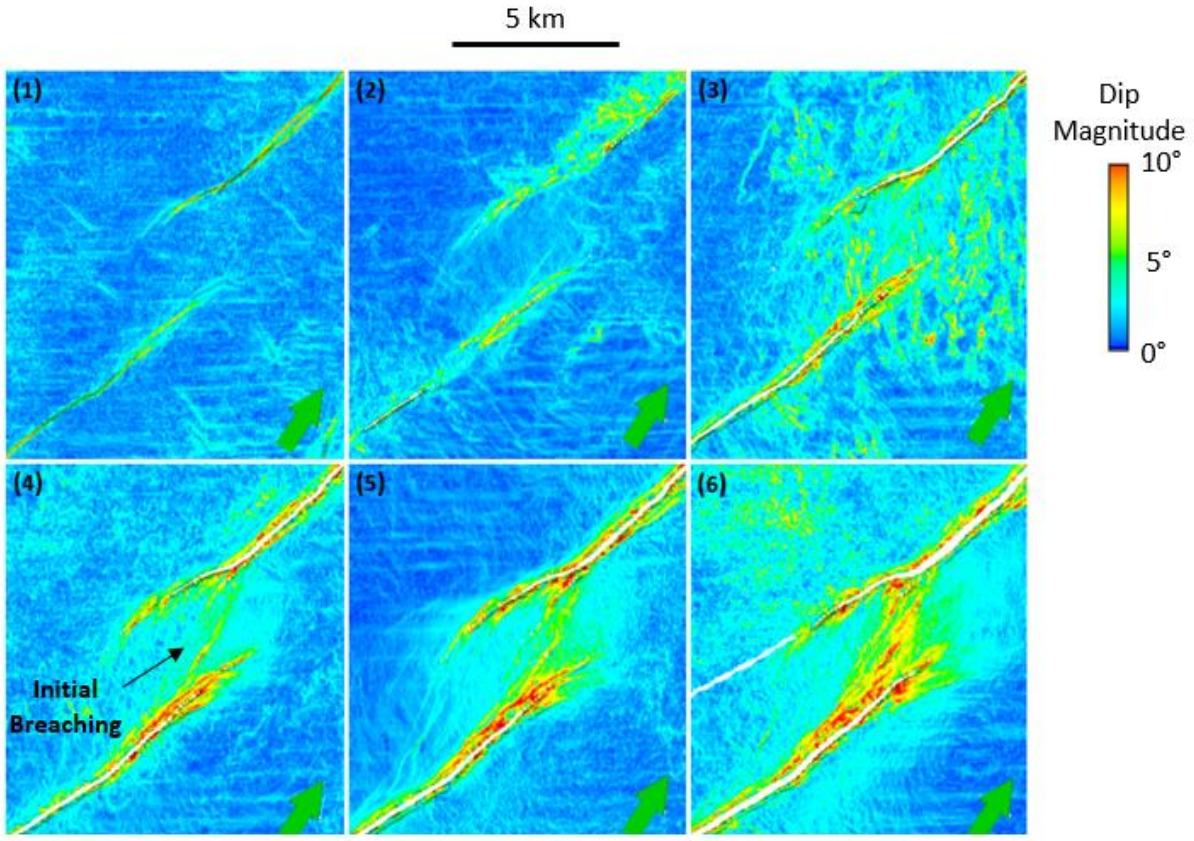


Figure 2.13. Horizon slices through the dip magnitude volume for Horizons 1 through 6 for Ramp 1.

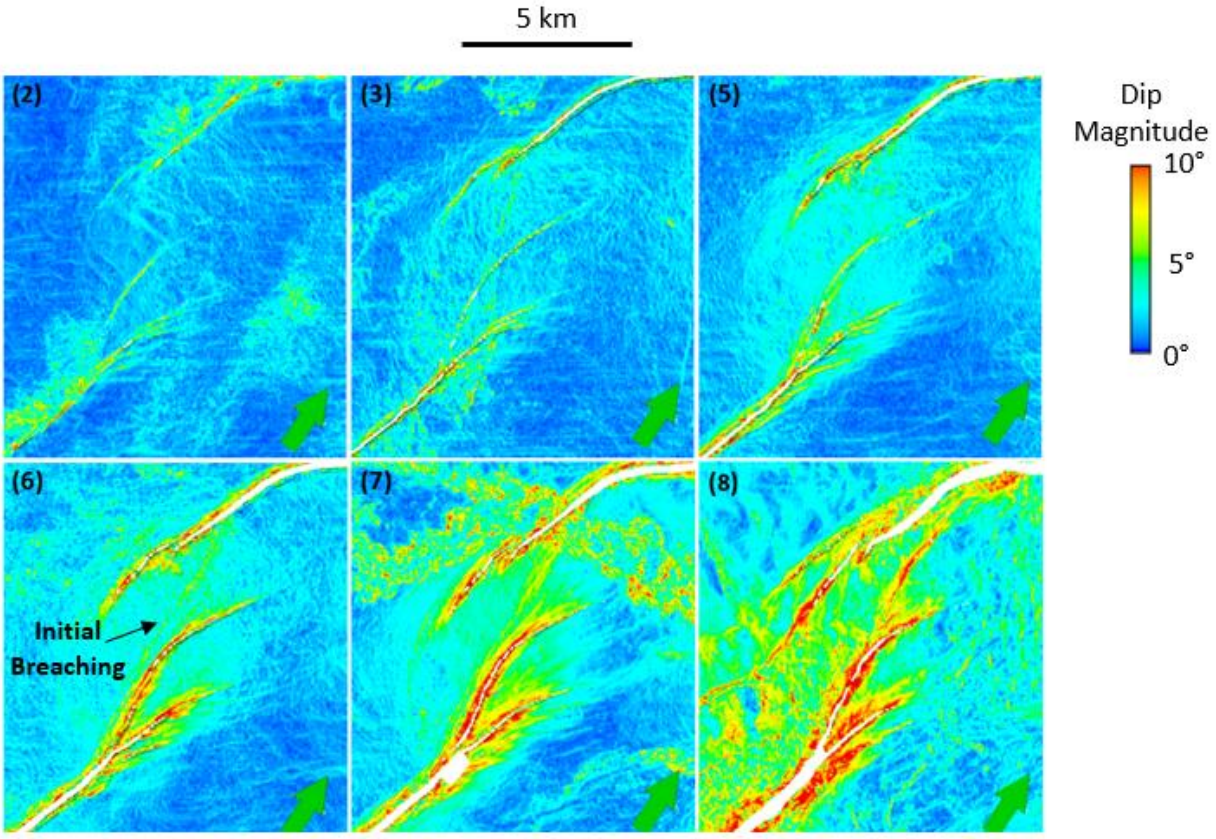


Figure 2.14. Horizon slices through the dip magnitude volume for Horizons 2 through 8 for Ramp 2.

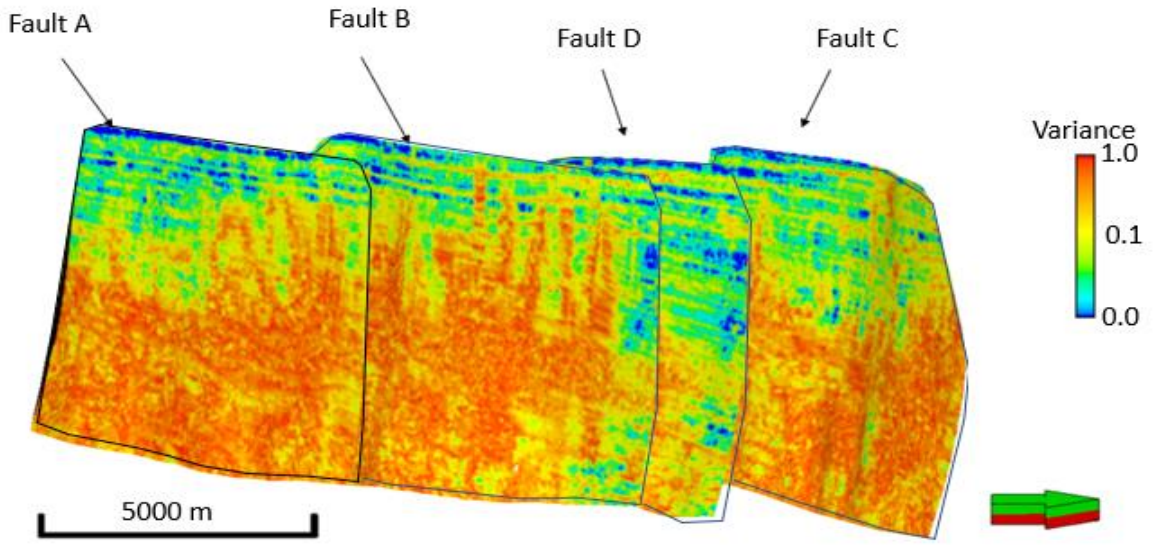


Figure 2.15. Mapped variance onto the fault planes with red indicating an increase in variance from Horizons 1 to 11 (faults four times vertically exaggerated).

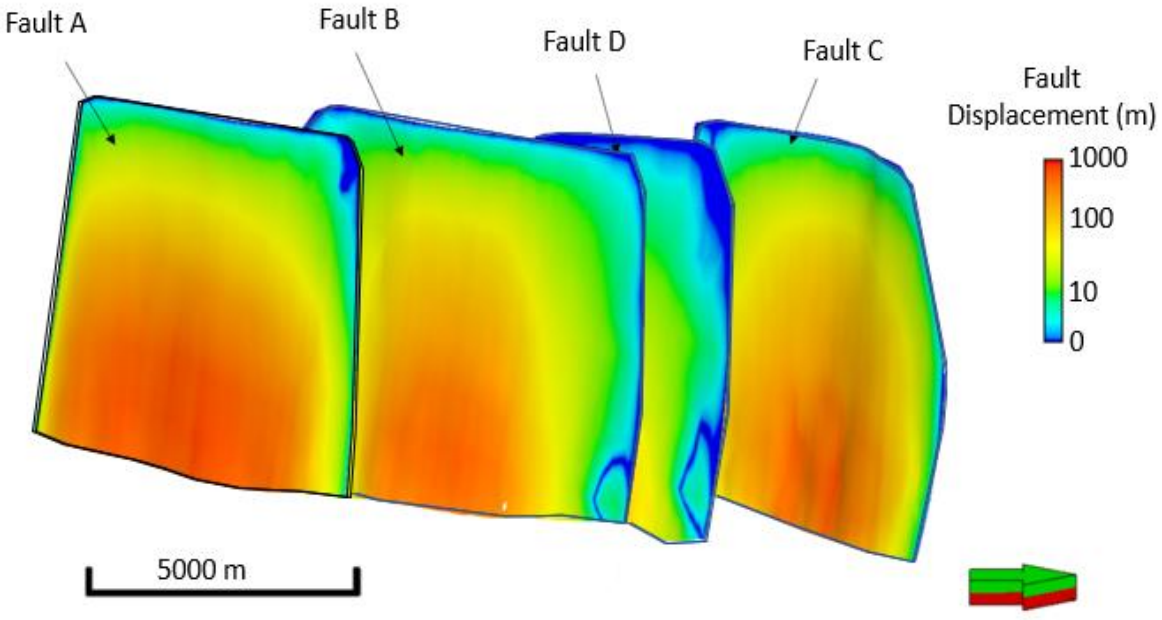


Figure 2.16. Calculated displacement using depth converted seismic data showing an increase of displacement towards the bottom-center part of the faults (four times vertically exaggerated).

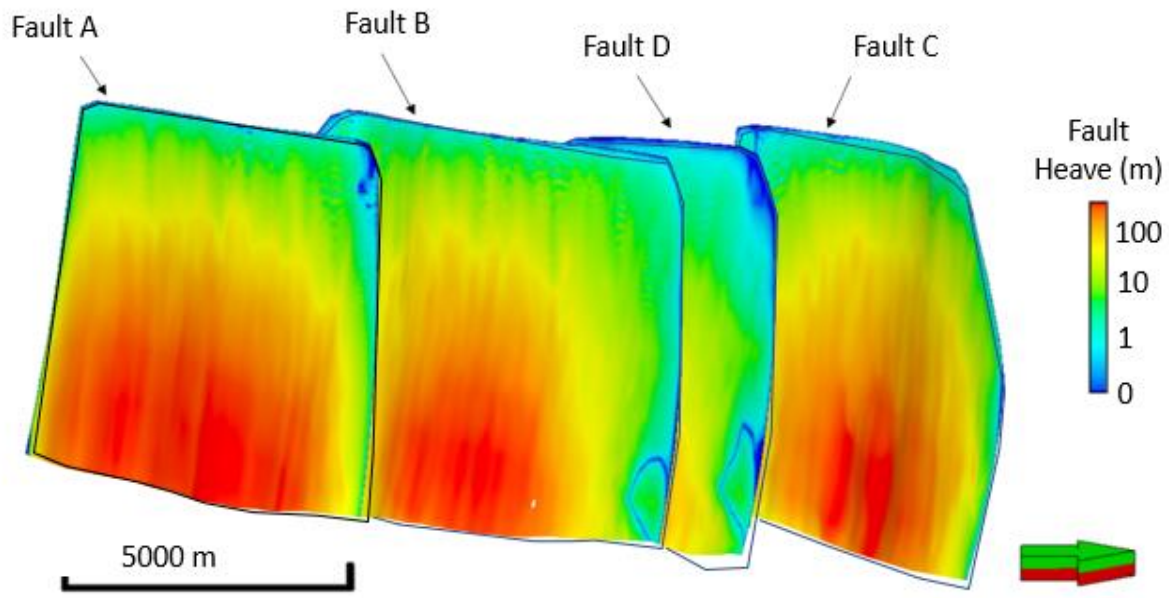


Figure 2.17. Calculated heave using depth converted seismic data showing an increase of displacement towards the bottom-center part of the faults (four times vertically exaggerated).

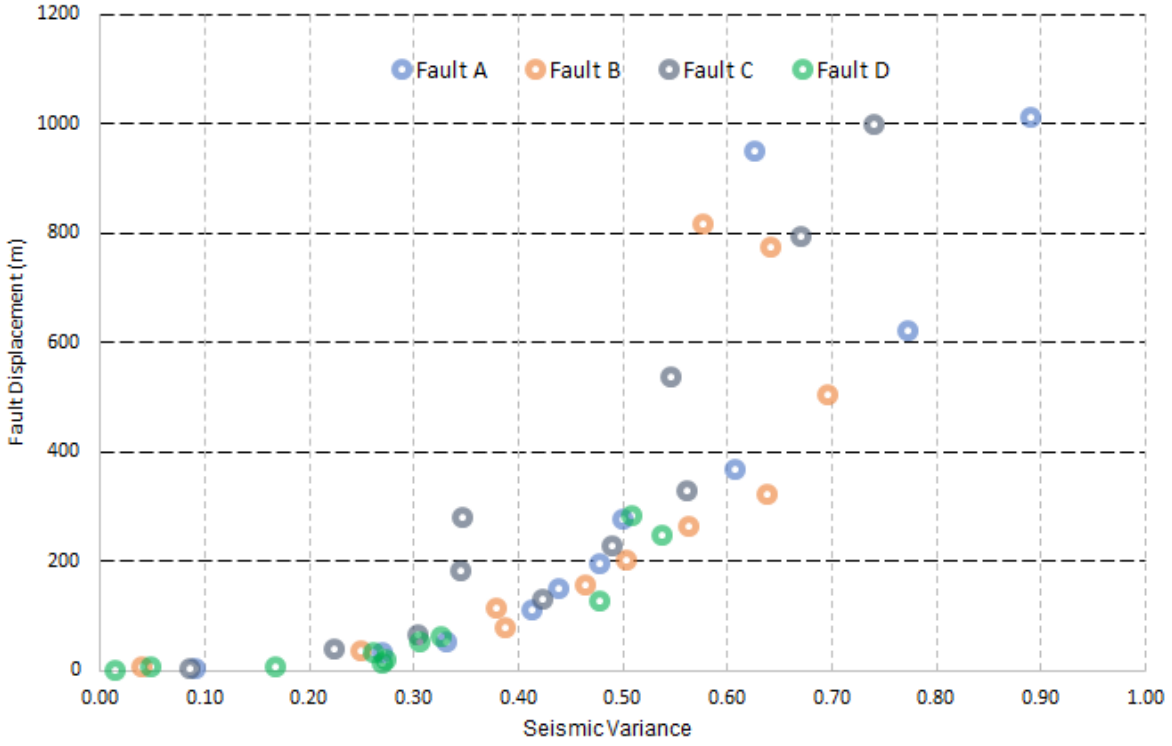


Figure 2.18. Maximum displacement seen for every fault at every horizon plotted against average variance measured from mapped seismic attributes.

Coherence or variance below a certain threshold, can also to study the nature of secondary faulting. This is useful for predicting and mapping the distribution of smaller faults in a faulted zone. Figure 2.19 shows examples of variance at representative horizons, within the ramps area, close to the faults, highlighting additional possible smaller faulting. The variance indicates a change in color at the tip of the faults and splaying of the faults into smaller sub-faults or splays. These splays are difficult to predict or map with conventional amplitude mapping.

c) Seismic Curvature

Curvature measures the variation of a local surface from a plane. In terms of fault tectonics, curvature a good proxy in measuring strain. Figure 2.20 shows a horizon slice along horizon 8 through co-rendered most positive and most-negative curvature and a vertical slice through co-rendered most positive and most-negative curvature and the seismic amplitude volumes. Note that the footwall side of the fault exhibits a positive-curvature anomaly (in red) and the hanging wall a negative-curvature anomaly (in blue) common to many, if not most normal fault geometries. Note on the horizon slice that the fault discontinuity does not line up with the curvature anomalies, indicating a lateral error in the fault picks.

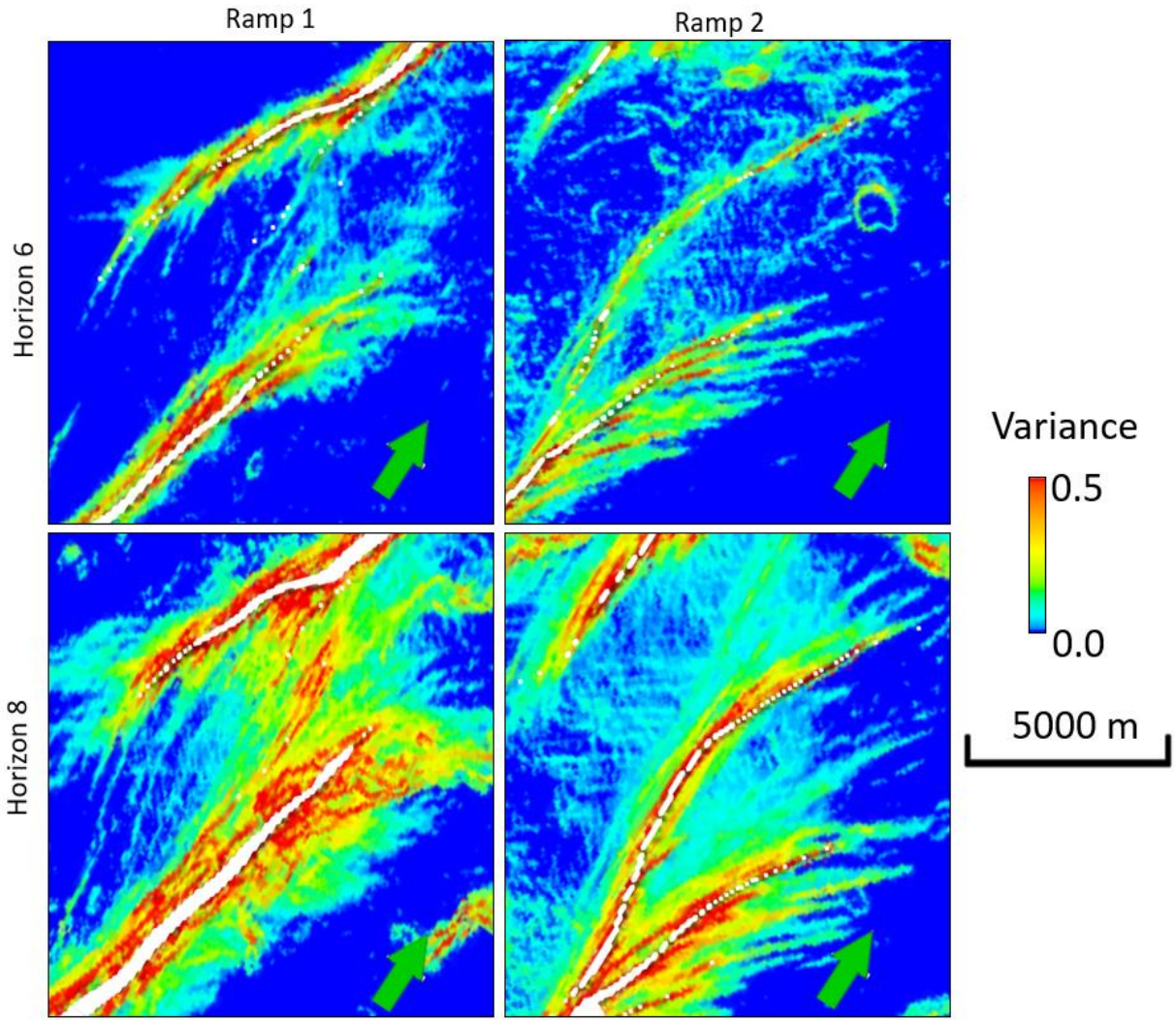


Figure 2.19. Zoomed images of horizon slices along Horizons 6 and 8 through the variance volume showing small sub seismic faulting along Ramps 1 and 2.

Figure 2.21 shows a suite of nine horizon slices through the co-rendered most-positive and most-negative curvature volumes. As in the previous figure the curvature attributes near the fault zone show positive curvature on the upthrown block and negative curvature on the downthrown block related to folding of the beds. Beds on the upthrown block rotate into the fault forming anticlines, whereas on the downthrown side, beds rotate up to the fault (up to 10 degrees or more dip), forming a syncline. Deeper formations (Horizons 8, 9, 10, and 11) tend to have more complex attributes caused by the longer structural history and additional tectonic events that they

underwent. In addition to these larger-scale features, the curvature also shows a very sharp increase over a short distance near the fault, attributed directly to the faulting.

The degree of curvature can be seen to correlate with the amount of displacement on the faults. As displacement increases, the amount of curvature increases indicating increased bed rotation. By examining the cross section shown in Figure 2.3, the overall geometry of the beds outside the fault zones is seen to be flat, with consistent rotation near the fault. Both the magnitude of rotation and the width of the folded zone is associated with the displacement as well as the lithology.

Traditional models of transfer zones (Morley et al., 1990) show only broad rollover folding of beds related to the changes in fault dip, but no additional folding in the immediate vicinity of the fault. However, experimental studies (Paul and Mitra, 2013) suggest that in many instances, additional extensional fault-propagation or drape folding occurs in the vicinity of the faults, altering the geometry of the transfer zone. Drape folds, accompanied by drag folding, produce the curvature changes described above for the Parihaka fault system. Therefore, the broader curvature changes directly record drape folding, whereas the sharp changes reflect the effects of the faulting. The presence of drape is also supported by the cross sections through the traditional amplitude data (Figure 2.3).

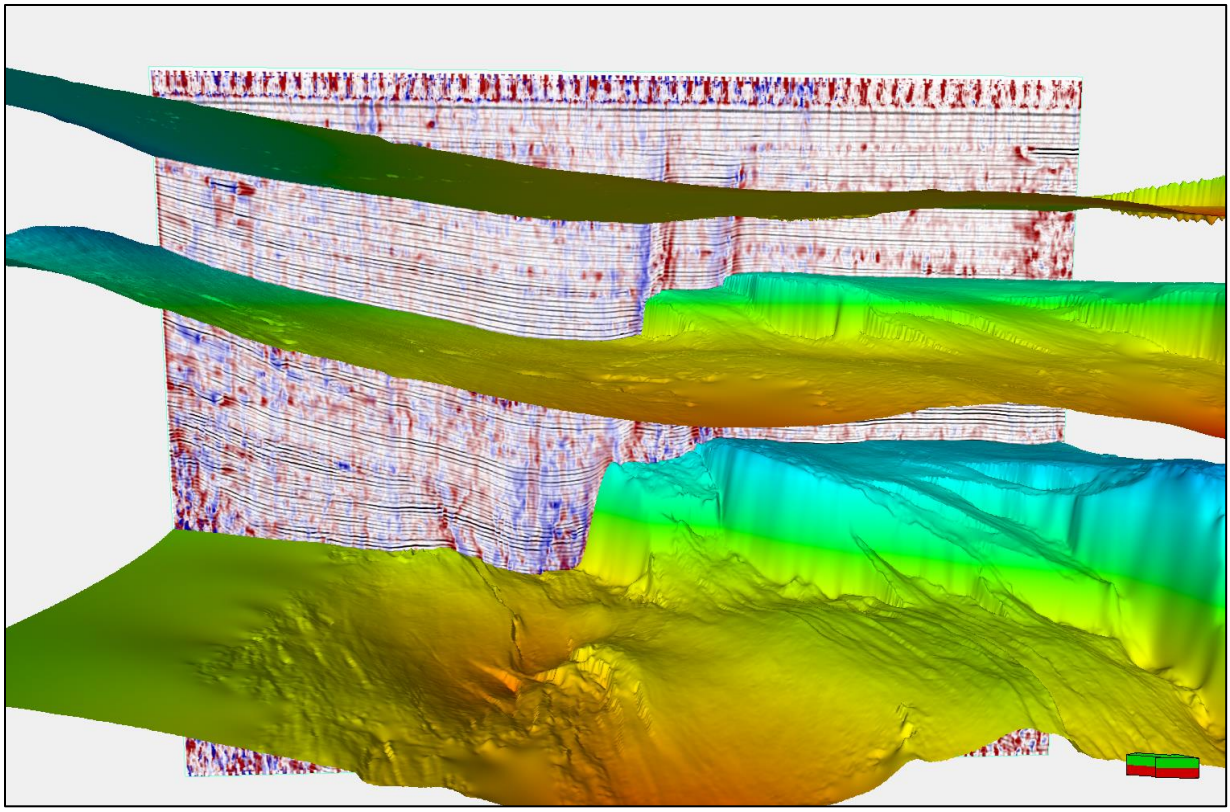


Figure 2.20. Time-structure maps of Horizons 2, 8, and 11, and a vertical slice through co-rendered most-positive curvature, k1, most-negative curvature, k2, and seismic amplitude, showing the correlation of positive curvature anomalies with the hanging

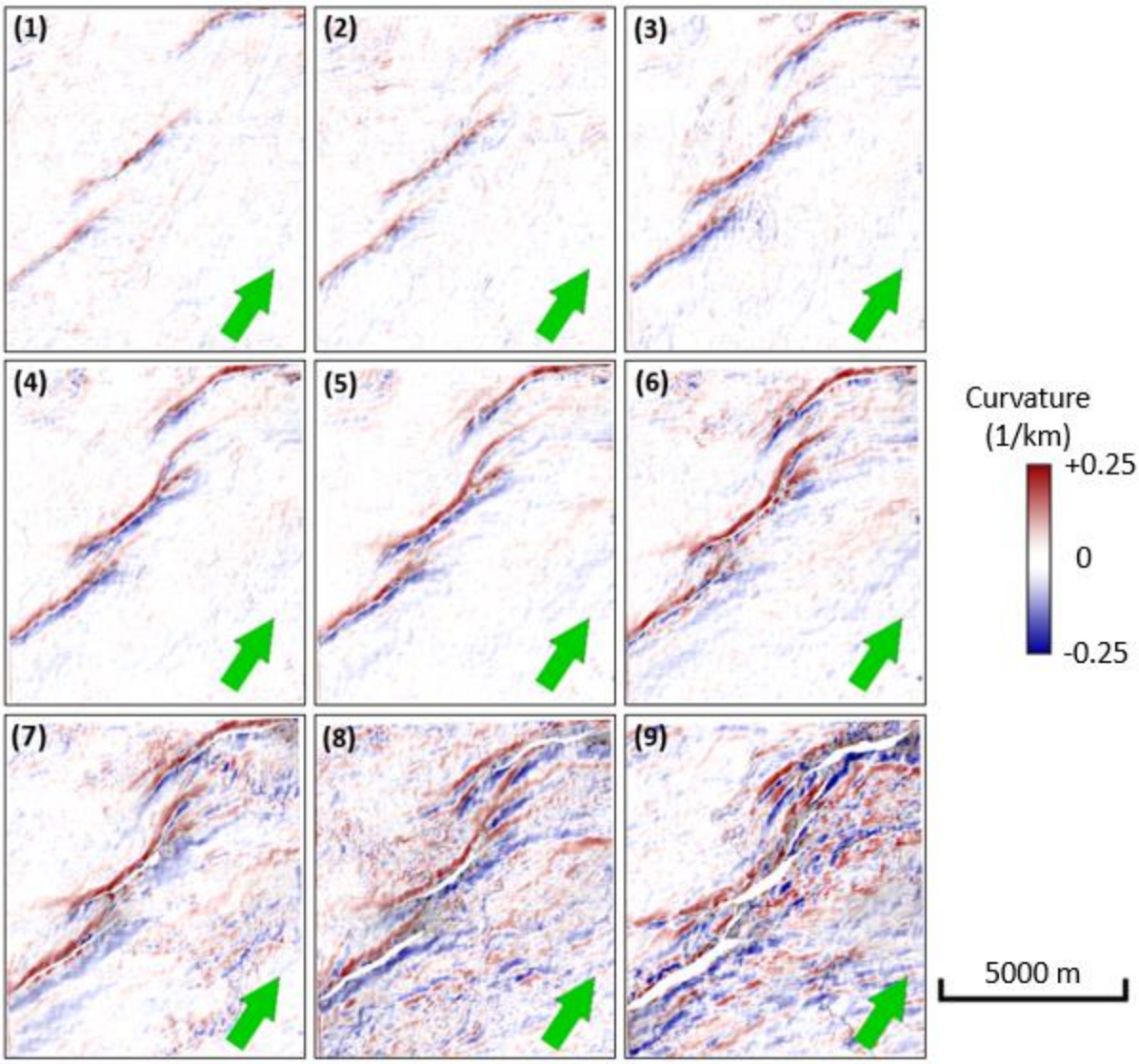


Figure 2.21. Co-rendered most-positive (k_1) and most-negative (k_2) curvatures computed from picked Horizons 1 through 9 showing an increase in curvature associated with increased displacement.

7. ANALYSIS

Based on the results presented above and the observation from the application of seismic attributes to faults and horizons, understanding the deformation mechanism and growth history of some of those transfer zones can be determined. By examining the seismic dip data, the bed dips can be imaged to determine the degree of deformation that transfer zones have undergone. As

displacement increases within relay ramps, beds within the ramp rotates to accommodate for the displacement. Above a certain dip angle, ramps cannot further accommodate the additional displacement leading to the formation of smaller faults. This critical dip for the formation of secondary faults is probably controlled by the lithological composition of the beds. This growth model approach is consistent with the model that Peacock and Sanderson (1994) suggested where faulting is seen to occur post breaching or splay formation. No evidence shows that transfer zones breaching, and rotation and fracturing of beds are occurring post hard-link faulting development.

The intensity of breaching experienced by Ramp 1 and Ramp 2 can be seen using the seismic dip data as well as the variance and curvature. This observation is consistent with the bed rotation deformation mechanism and indicates higher density of fracturing with deeper formations/horizons that have undergone further deformation. Similarly, in Figure 2.20, the degree of curvature can be seen to correlate with the amount of displacement on the faults. As displacement increases, the amount of curvature increases indicating increased bed rotation. By examining the cross section shown in Figure 2.3, the overall geometry of the beds outside the fault zones is seen to be flat, with consistent rotation near the fault. Both the magnitude of rotation and the width of the folded zone is associated with the displacement as well as the lithology. However, lithological implications might have limited controlling factor to the degree of fracturing that those beds and ramps are showing compared to the displacement. Traditional models of transfer zones (such as the one suggested by Morley et al., 1990) show only broad rollover folding of beds related to the changes in fault dip, but no additional folding in the immediate vicinity of the fault. However, experimental studies (Paul and Mitra, 2013) suggest that in many instances, additional extensional fault-propagation or drape folding occurs in the vicinity of the faults, altering the geometry of the transfer zone. Drape folds, accompanied by drag folding, produce the curvature

changes described above for the Parihaka fault system. Therefore, the broader curvature changes directly record drape folding, whereas the sharp changes reflect the effects of the faulting. The presence of drape is also supported by the cross sections through the traditional amplitude data (Figure 2.3). Within the transfer zones, this indicates that many of those beds with maximum curvature observed, indicates that significant rotation and thus higher amount of fracturing and/or faulting which accompany the splay faults formation.

In addition, variance extracted along each of the fault planes shows a correlation with calculated displacement that faults have undergone. This observation indicates that the similarity between the upthrown and downthrown blocks is significantly reduced for deeper formation levels, hence hinting at significant changes in seismic response. This is partially carried by the higher displacement and juxtaposition of different formations, but it is significantly related to the additional breaking and fracturing that fault zones experience. Despite being hard to assess, the degree of fracturing that damage zones have experienced, it can be qualitatively estimated that higher degree of breaking is expected.

CHAPTER 3: ASSESSING FAULT SEALING POTENTIAL AT TRANSFER ZONES

Fault sealing potential within a transfer zone requires a knowledge of the rock behavior coupled with seismic properties to derive valuable information on fluid migration. We examine the most common methods used to assess fault sealing behavior and proceed with a 3D fault sealing potential analysis. A seismic well-tie was conducted on available well data in the Parihaka fault area then seismic inversion was conducted to determine density and impedance data. Inverted volumes were then used to derive rock properties. Different fault sealing assessment methods were used to determine sealing capacity of those faults and potential pathways along

transfer zones. This included a 1D and 3D juxtaposition analysis as well as a 3D Shale Gouge Ratio (SGR) estimation for each fault and for the two relay ramps. Results indicate that even though faults have tendency to seal, transfer zones are predominately acting as migration pathways.

1. INTRODUCTION TO FAULT SEALING METHODS

Fault sealing analysis is a tool in hydrocarbon exploration and production particularly in regard to seal capacity (Peacock et al 1994, Sayers, 2002, Tobias et al, 2015). It is a key element in risk assessment of exploration targets and plays. Seismic data, well logs, core data and other information are typically used to estimate fault properties. Many studies have used seismic inversion methods and amplitude derived attributes to determine fault curvature, displacement, continuity, and possibly lithological variations.

To better describe fault seal potential Pei et al. (2015) groups the fault seal types into two main groups: Juxtaposition seals and fault rock seals. Juxtaposition seals typically assume a siliciclastic rock (Knipe, 1992a) where an impermeable layer, usually shale, is juxtaposed next to a good permeable reservoir layer, usually sandstone, allowing any hydrocarbon to be trapped within it (Allan, 1989; Clarke, 2005; Gibson, 1994). Knipe (1997) introduces a method to assess fault juxtaposition based on stratigraphic layer description and the throw associated with the fault movement by projecting the footwall and hanging wall units onto the fault plane, and determining the leaking potential (Figure 3.1).

In contrast, fault rock seals assume that any fault has a core material and a damage zone that define the behavior of the fault as a conduit or a barrier (Caine et al., 1996). As displacement increases along faults, materials, particularly clay, are smeared within it at a defined thickness

related to the amount of displacement (Egholm et al., 2008). Lindsay et al., 1993 and Bense et all., 2003 confirmed such smearing in outcrop studies.

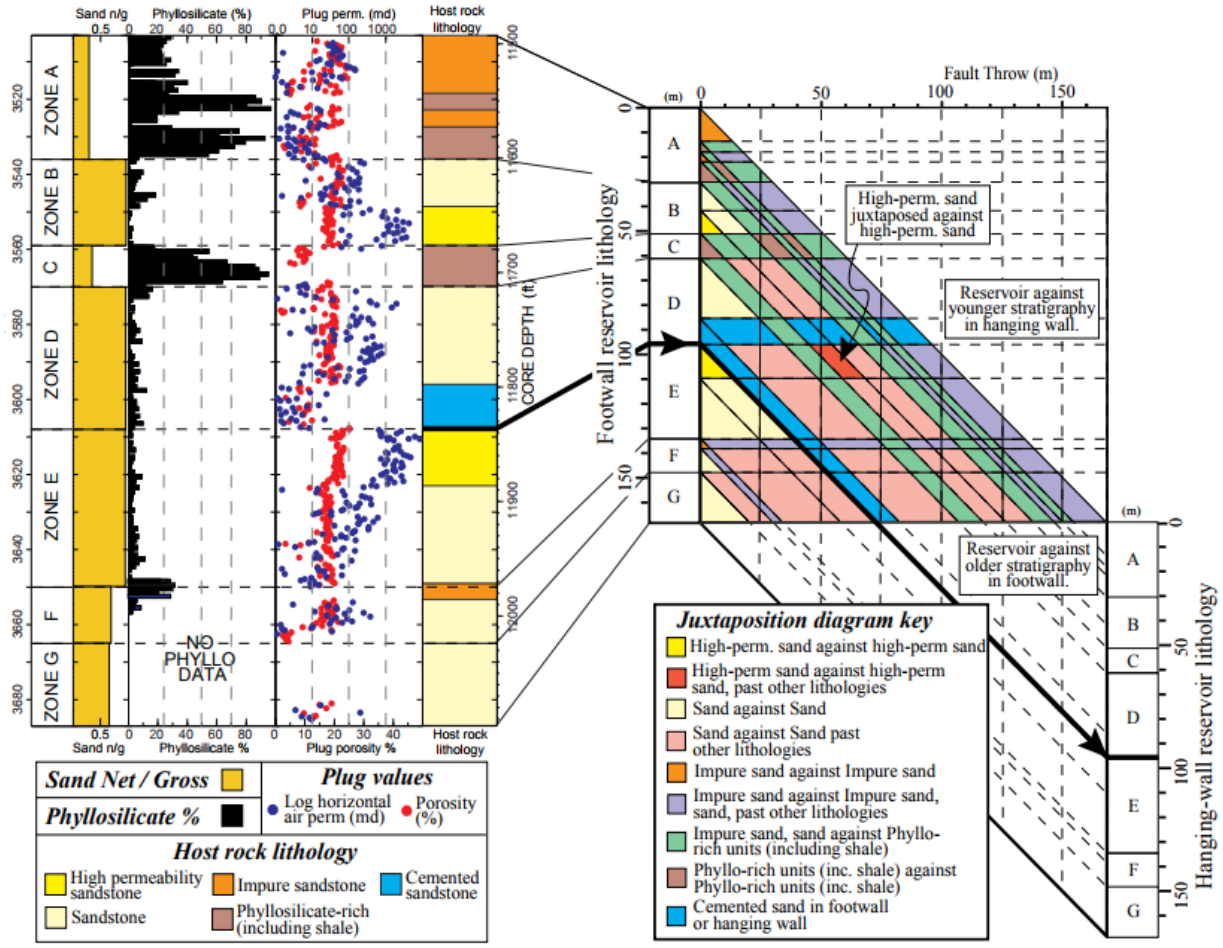


Figure 3.1. Juxtaposition diagram using stratigraphic layers and fault throw (Knipe, 1997).

Fulljames (1997) developed a quantitative method to describe the sealing potential of the rock by using a clay smear potential factor (CSP).

$$\mathrm{CSP} = c\frac{T_c^2}{d} \tag{1}$$

The factor is a function of the thickness (T) of the source bed and the distance (d) away from that bed caused by displacement where c is a calibration term for rheological properties and stress dependencies. CSP is one of many factors used in addition to Shale Gouge Ratio factor to

predict the clay content in any fault zone (Yielding, 1996). Disregarding the method used, all analyses technologies assume that a high clay content within the fractured zone is sufficient enough to seal any fluid migration. Yields (1996) assumes that a 15-20% SGR is sufficiently large to generate continuous smear and thus total sealing (Figure 3.2). Both methods are based on a visual assessment of the fault which is not possible from seismic surface data. They also require an estimate of the capillary sealing capacity.

Capillary sealing is caused by capillary forces due to the fine grain size within the formation, and can be derived at the "hydrostatic equilibrium condition". Ingram et al. (1997) and Nakayama et al (2002) define the capillary entry pressure, Pe, as a function of hydrocarbon column height, surface tension, and the pore throat radius (r) (δ is interfacial tension, and θ is wetting angle of the liquid).

$$P_e = \frac{2\gamma \cos\theta}{r} \tag{2}$$

As the pore throat increases the capillary entry pressure (P_e) is reduced and the thus the hydrocarbon column is lower. Hence, the hydrocarbon height (h) that the seal can withstand is related to the differential pressure (ΔP) across the seal and the density of water ρ_w and hydrocarbon ρ_h (Watts, 1987).

$$h = \frac{\Delta P}{g(\rho_w - \rho_h)} \tag{3}$$

Similarly, capillary pressure estimation be applied to fault seal behavior by studying differential pressure across the faults and failure in the seal caused by pressure alteration (Tobias, 2015). Rock failure by capillary leakage can be derived by related Mohr Coulomb failure criteria

to differential pressure near the fault. Pressure variations thus provide insight on fluid communication and migration potential.

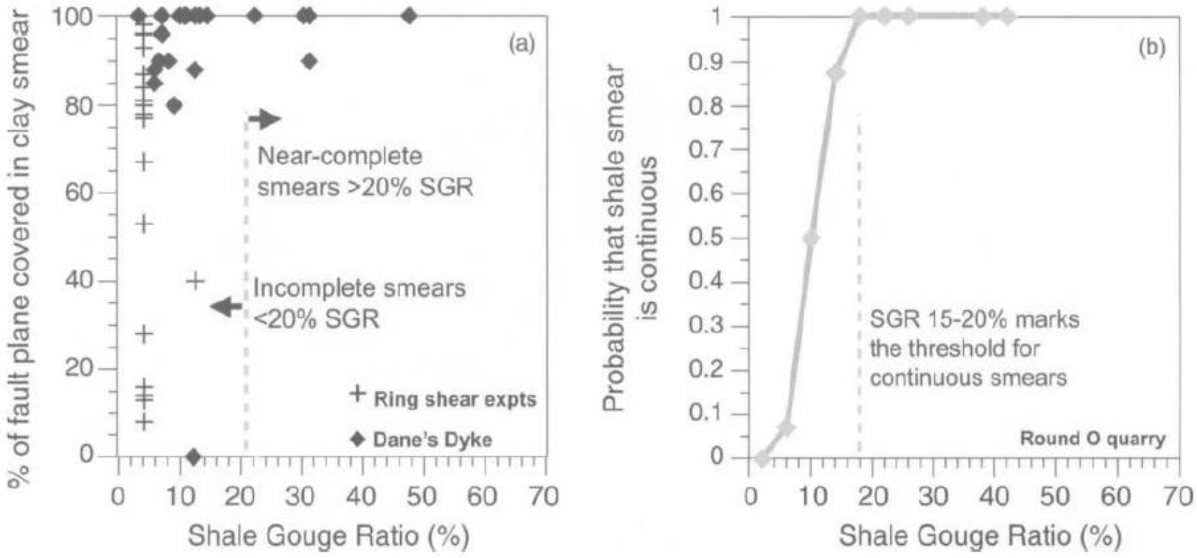


Figure 3.2. (a) Outcrop and experimental data for clay smear continuity, (b) Smear probability from 80m of fault traces in the Round O Quarry (after Yielding, 1996).

Pore pressure estimation is another common method used to asses faulting sealing potential by taking into consideration the distribution of pore pressure across the field. Pore pressure by itself can shed light on compartmentalization across faults, or any potential leakage as a result of a pressure increase. The most common method to estimate pore pressure in 3D is through the use of seismic data. Even though well logs are used to calibrate the modeled pressure, they do not provide 3D coverage of the interested area that seismic does.

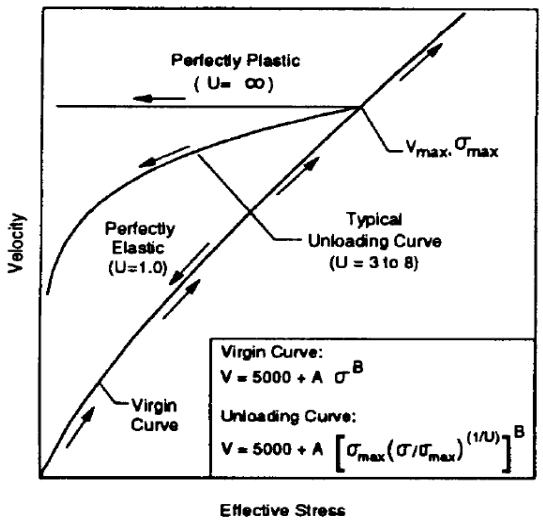


Figure 3.3. Bowers' Pore Pressure Estimation (Bowers, 1995).

There are multiple methods to estimate pore pressure using seismic velocity while the most frequently used ones for oil and gas application are Eaton's (1975) and Bowers' (1995) methods. The Eaton method, originally developed in 1975, is based on disequilibrium compaction within the formation causing pressure buildup such that the effective stress can be calculated using overburden and pore pressure (Eaton, 1975). Eaton developed an empirical relationship between pore pressure gradient (P_{pg}) and well logs, where sonic travel time uses the most useful measure. The formation pore pressure is then a function of overburden pressure, Sg, hydrostatic pore pressure, P_{ng}, and the sonic log time:

$$P_{pg} = S_g - (S_g - P_{ng})\left(\frac{\Delta t_n}{\Delta t}\right)^x \tag{4}$$

where Δt is transit time in shales, Δt_n is transit time in shales at normal compacted pressure, and x is sensitivity of velocity to differential stress).

Similar to the Eaton, Bowers' method is based on the disequilibrium compaction, also using an empirical relationship between pore pressure and sonic logs. Bowers (1995)

accommodates for fluid expansion and under-compaction. Pore pressure can be calculated using the virgin loading or the unloading curves thereby defining the upper and lower boundaries are defined (Figure 3.3). As effective stress increases, the velocity will increase following the virgin curve. As stress decreases caused by fluid expansion or the unloading of the vertical stress on the rock, the rock not being perfectly elastic nor plastic follows the unloading curve instead.

Whereas the above described methods were derived from well logs, multiple attempts have been made to use seismic velocity (V_p) to estimate pore pressure. Sayers (2002) was among one of the first few studies that estimated pore pressure using seismic data. The results though, required few modifications, but were able to provide valuable information about pore pressure ahead of the drill bit in the Gulf of Mexico. Similarly, Tobias (2015) used Eaton's method to estimate pore pressure distribution within the Dampier sub-basin of the North West Shelf of Australia (Figure 3.4). This work presents a simple approach to fault seal analysis by estimating pore pressure variation across the field. While pore pressure changes across adjacent compartment to the other, this indicates that the fault separating them prevents the flow of fluid from one place to the other, thus creating differential pressure.

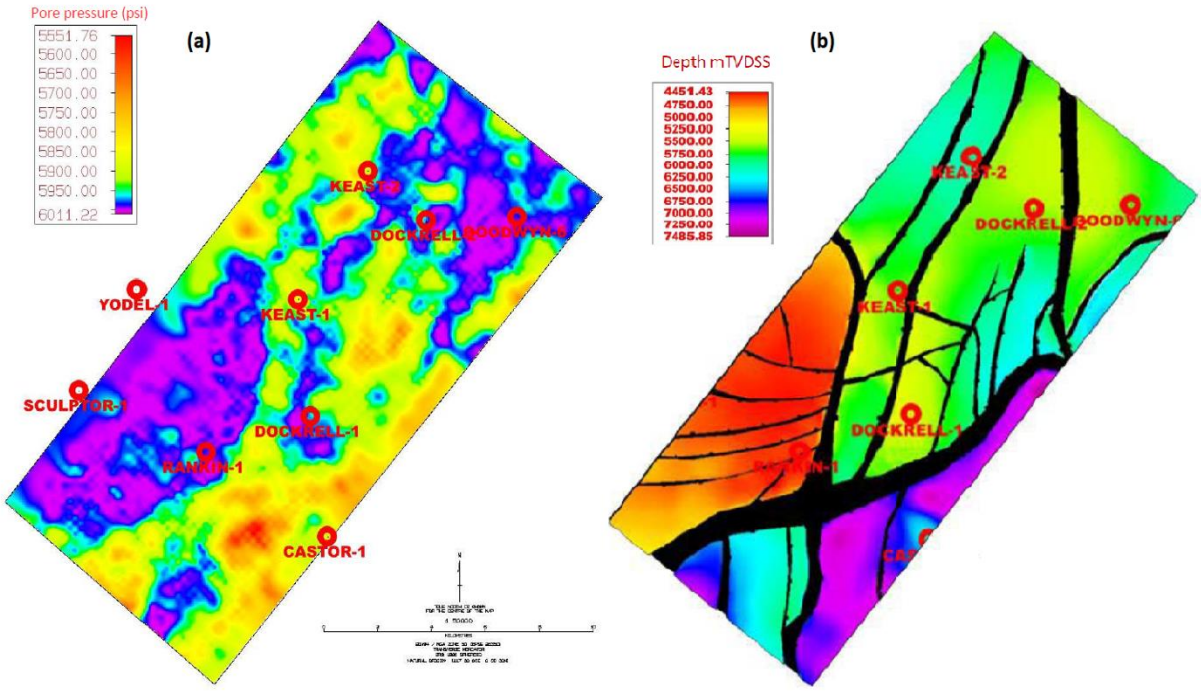


Figure 3.4. (a) Pore pressure estimation for the Norian horizon, (b) Structure map for the Norian formation showing structural changes and major interpreted faults in the area (edited from Tobias et al, 2015).

The use of seismic data allows for a three-dimensional view of variations in pressure within the field. Data availability is by far the most important limitation to consider and be aware of before proceeding in our analyses. Beyond the data limitations, it is important to highlight the assumptions for most of those equations. Both theoretical approaches assume uniform, homogenous rock, mostly elastic, and without any geomechanical anisotropy. Despite the complexity associated with addressing those assumptions, valuable information can result by considering them. The work presented here will describe a new workflow that uses seismic inversion data to assess fault sealing potential using stratigraphic juxtaposition and shale gouge ratio methods. The work first step is to construct a seismic to well data tie, and use it to derive acoustic and density volumes for the seismic cube. Then using elastic properties, we will predict

porosity, gamma ray, and other properties that can be derived which can be used to map the facies variation across the seismic volume. Once facies are mapped in 3D, we will apply a juxtaposition analysis and estimate the Shale Gouge Ratio (SGR) to determine sealing potential for each of the major faults and the main two (2) relay ramps.

2. METHODOLOGY

To assess the fault sealing potential, this chapter focuses on extracting data using seismic inversion of faulted zones to determine juxtaposition of permeable and impermeable lithologies across a transfer zone as well as estimate assessment of the clay smearing behavior. Specifically, sealing assessment herein we will relate the degree of deformation of relay ramps to the lithological displacement of beds. For this work we will use the same dataset from the Taranaki Basin described in Chapter 2, which showed us two (2) relay ramps connect three (3) normal faults in relatively young sediments. The potential of hydrocarbon generation within those formations is minimal considering the age and burial depths of those formations.

The available seismic data within the Taranaki Basin contains four (4) vertical wells with gamma ray, density, P-wave acoustic logs in all wells. There are no S-wave logs. Well Kanuka #1, is slightly outside the seismic coverage area, and north of our area of interest is the only well with shear wave logs (Figure 3.5). For this reason, neural network method was used to compute shear logs in all other four (4) wells that fall within the seismic survey. The method uses some of the shear data available in the Kanuka #1 well as the desired output data and the other three logs as input to train the network. The algorithm is then validated on the part of the data that was not used in training. Figure 3.6 shows a cross-section of four (4) wells including the Kanuka 1 well. The orange DTS curve is the measured shear log. The blue curve is the predicted DTS log using a

neutral network trained on the compressional DT log: note the good match between the measured and predicted data.

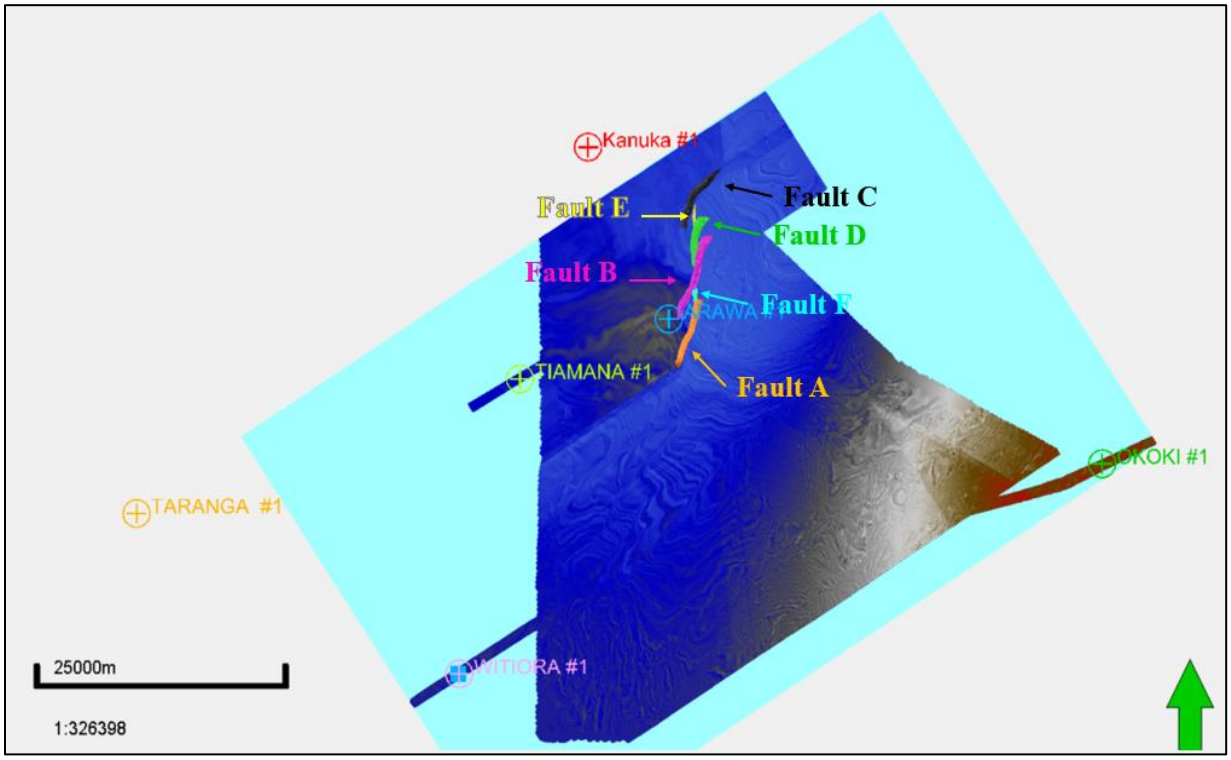


Figure 3.5. Map view of the data availability including the seismic data (amplitude slice shown) along with interpreted faults and four vertical wells (For a zoom in of the fault system refer to Figure 2.2).

The seismic to well tie was completed using Hampson Russell software for all four (4) wells and by extracting a wavelet from the well information. Once a good well tie is achieved, inversion of the seismic P-impedance data can then be completed to derive the S-Impedance volume, and Density volumes and then depth-converted to match the vertical data at well locations. Depth converted volumes can then be used to complete and conduct the fault seal analysis workflow. Interpreted horizons and faults in the area were also depth converted.

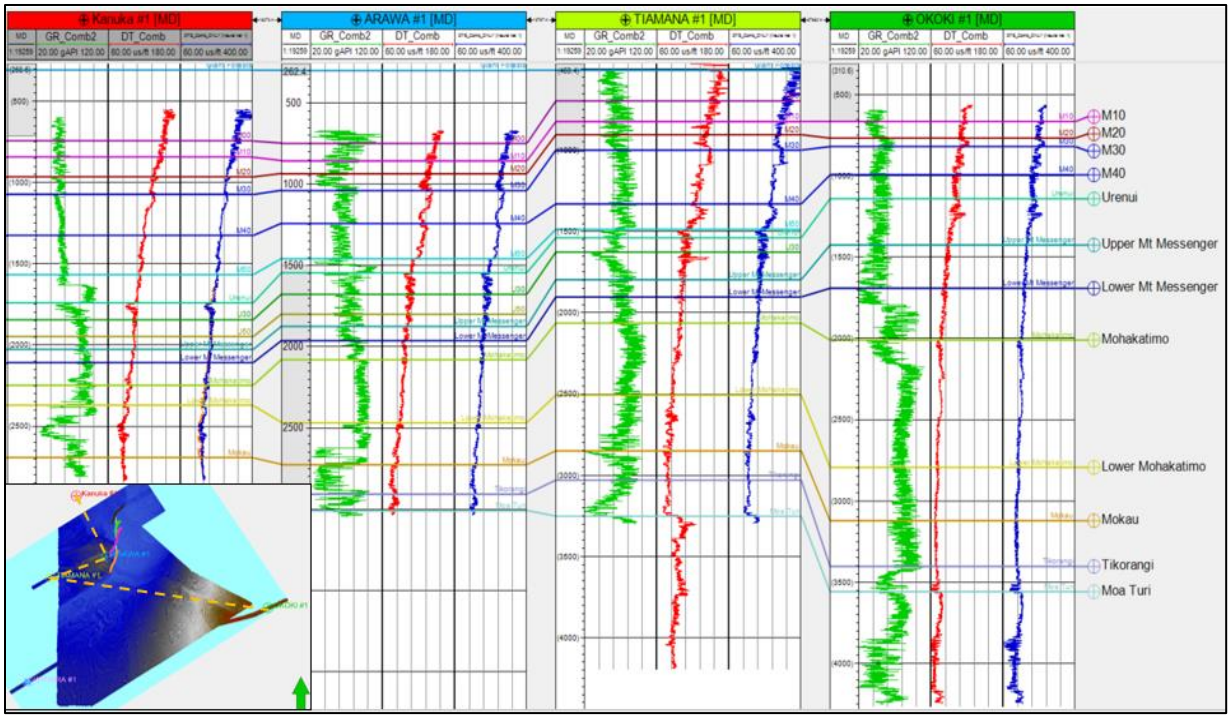


Figure 3.6. Cross-section through the main four (4) wells within our area of interest showing the compressional and shear slowness data.

3. TECTONIC BACKGROUND

The system within the Taranaki Basin consists of two episodes of deformation: the first one is associated with the volcanic activity in the basin and characterized by basement normal faulting, while the second episode is defined by shallow normal faulting within the sedimentary column. This study focuses only on the shallow structural deformation associated with normal faulting which might be impacted by deeper basement activity. Understanding the relationship between the shallow and deep system is beyond the scope of this study.

The Arawa #1 well is the closest well to the normal faults drilled and completed in 1992 targeting a “bright spot” on the seismic volume in a structural trap within the deeper system. Despite a minor gas show observed while drilling, the targeted formation turned out to be volcanic rock, not hydrocarbon bearing rock. Infante-Paez et al. (2017) studied igneous intrusions within

the Taranaki Basin by examining seismic amplitude, derived attributes, seismic stratigraphy principles, and seismic geomorphology. The study concluded that igneous rocks can “mimic” the seismic response of carbonate buildups, or siliciclastic mass-transport complexes. Seismically, the acoustic and density properties of the igneous rocks are similar to carbonate, both of which are different than clastics.

The Parahaki fault system consists of three en-echelon faults connected through two relay ramps or transfer zones (Figure 3.5). Displacement along those faults is thought to have started around 11 million years ago and continued through the shallow young sediment column during the last million years. Maximum displacement is observed to be exceeding 1000 m for the southernmost fault and to be decreasing to a relative minimum at relay ramps locations. Most of the faulted formations are assumed to be unproductive following the drilling of several exploration wells. This reservoir mainly consist of the Rangitikei group (mainly Giant Forest and Matemateonga), the Wai-ti group (including the Urenui, Mt Messenger, Mohakatino, and Moki), down to the Nigatoro group (Figure 3.7).

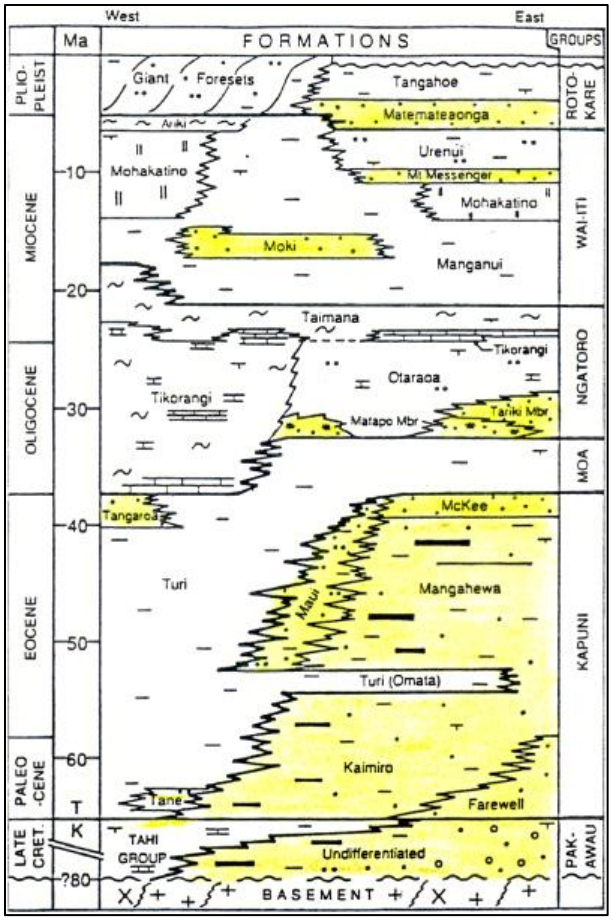


Figure 3.7. Taranaki Basin stratigraphic column (King and Thrasher, 1996).

4. FORMATION CHARACTERIZATION

According to Tripathi and Kamp (2008), the Rangitikei group is a Late Pliocene formation deposited mainly in a regressive system track with thinly deposited transgressive beds. Sediments are characterized by alteration of 4-5 m thick sandstone layers along with thick mudstone intervals built out the Giant Forest formation as part of a submarine fan system. The Matemateonga sequence started depositing during the late Miocene through the early Pliocene consists of predominately sandstone interbedded with siltstones deposited in shelf to marine environment (SENZL Report, 2009).

Based on available New Zealand government reports for exploration in the Taranaki Basin, the Wai-ti group is defined to be Miocene in age and spanning about 20 million years consisting of primary exploration targets. The Urenui formation within the Wai-ti group is mainly a siltstone and mudstone interval compromised of thick claystones that are eroded in some areas with channels (SENZL, 2009). Urenui is a continuous formation that can easily be picked on seismic lines. The Mt Messenger formation, is one of the targeted reservoirs consisting of fine to medium coarse sandstones with minor interbedded mudstones. The base of the Mt Messenger is defined by a sonic marker caused by the cementation of planktic foraminifers (Tripathi and Kamp, 2008). The underlying formation is the Mohakatino lower slope formation redeposited by volcanic highs during the reactivation of the Taranaki Graben. The unit consists mainly of reworked detritus volcanic deposits, highly heterogenous siltstones and mudstones, non-continuous sandstone reservoirs, highly faulted and fractures intervals, and that are rich in swelling clays.

Other units form the Wai-ti sequence including the Awakau fm (interbedded sandstone, siltstone, and shale), the Manganui fm (predominately mudstone deposited in a deepwater setting), and down to the Moki fm (SENZL, 2009). The Moki fm. are mainly consists of deepwater turbidites with sand channels clearly seen on seismic amplitude and seen to be controlled by faulting.

Figure 3.8, shows a cross-section through the main three (3) wells near the fault system on the upthrown side of the fault. Main formation tops are correlated across and additional tops are added to match the interpreted horizons in the seismic data. Those additional subdivisions allow studying certain intervals with reservoir-like properties in order to assess fault sealing potential (Giant Forests divided into M00, M10, M20, M30, and M40, Urenui divided into Urenui, U30 and U50, Mt Messenger into Upper and Lower, Mohakatimo into Upper and Lower).

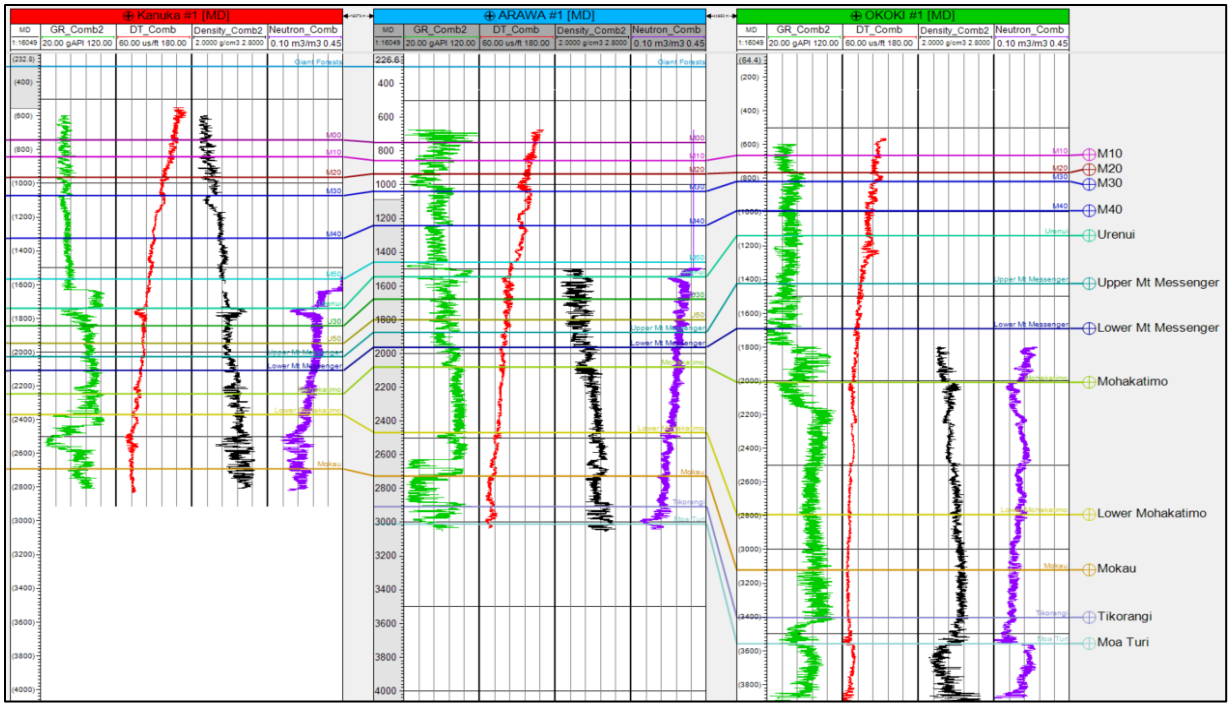


Figure 3.8. Cross-section through the main 3 wells with gamma ray (green), compressional slowness (red), density (black), and neutron (purple) logs.

5. SEISMIC INVERSION WORK

a) Inversion Assumptions

Post stack 3D seismic inversion allows for the generation of impedance data which represents layer-based rock properties using interpreted horizons, well data, a background velocity model, the estimated wavelet, and petrophysical rock modeling. In addition to its ability to reduce interference effects and tuning and increasing bandwidth, inversion is used to better integrate the data available and define rock facies for sealing potential. Once impedance inverted volumes are generated they can be converted to depth which allows for tying with well data and generating inverted reservoir properties volumes. Inversion is carried using a deterministic approach to derive S-Impedance, and density volumes.

A total of ten (10) interpreted horizons were used in the inversion to assure the control of the inversion across the faults where growth units are clearly observed on the downthrown block. The interval covered by those horizons is most of the Wai-ti group and some of the Rangitikei group. The four (4) wells, shown in Figure 3.5 were used to generate a seismic-to-well tie and derive a time-depth relationship using an extracted wavelet. The appendix figures show the well ties associated with all four (4) wells and the corresponding seismic wavelet. Comparison of synthetic seismic and actual data shows major events and a good overall match, exceeding 85% in all three (3) wells, with limited stretching and squeezing of the data and less than 15 ms difference between the sonic and seismic time (drift curve). A statistical wavelet (Figure 3.9) estimation was carried around each wellbore using a defined cube of seismic traces to maximize the tie between seismic data and synthetic reflection coefficient calculated from well logs. The final extracted wavelet is shown to be stationary with zero phase and bandwidth of 180 ms. This final extracted wavelet is determined to best fit most of the wells and give the most accurate inversion model (least matching with the Taimana 1 well, with only a 60% match). A lowcut frequency filter (5-15 Hz) was applied separating low frequency trends and allowing for better inversion within seismic bandwidth.

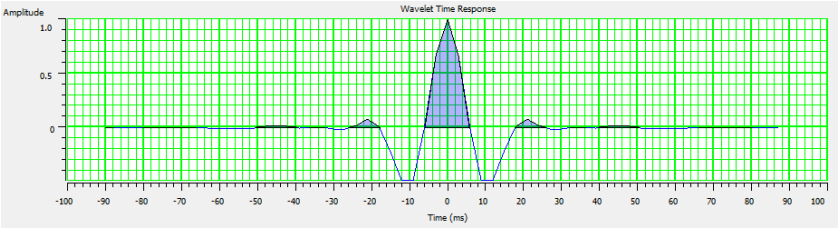


Figure 3.9. Statistical wavelet extracted from seismic and used for well-tie and inversion.

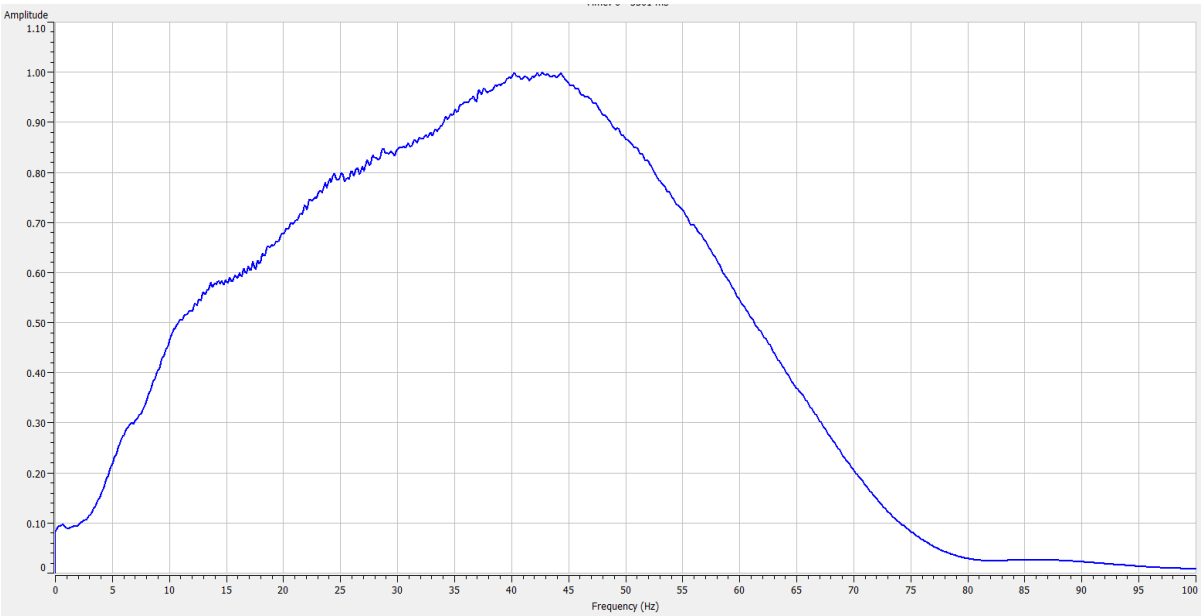


Figure 3.10. Amplitude spectrum of the seismic data.

b) Rock Properties Modeling

Inverted impedance volumes are the main output of the inversion process and are used as the main input for the rock properties volume. A strong relationship between rock properties, facies, and seismic impedance is essential for accurate models. In addition, the impedance volumes present a higher resolution dataset due to the elimination of thin bed tuning and side-lobes of the signal.

Multivariant analysis can be very useful to assess the relationship between different input parameters and rock typing. Relationships were initially established for available well data using calculated logs and derived properties. Prior to establishing those relationships, well data was carefully normalized and corrected for borehole conditions, tool calibration, and other geological variations that can impact the results observed. Total porosity is derived using neutron density cross-plot, corrected for volume of clay, which was derived from the available gamma ray logs. Fluid saturation values, which is mainly brine within our structural window of interest, were

calculated using Archie's equation with established parameters from core and other data provided by the New Zealand Ministry of Economic Development. Mudlog reports for the Arawa #1 well and examination of available full core data from the Okoki #1 well, combined with prior geological knowledge of the reservoir in the area, provided insight on the rock facies.

Figure 3.11 is a plot of Vp/Vs and P-impedance colored by porosity for the Kanuka #1 well (outside seismic). This plot shows that most all the data fit within one trend indicating a brine system with little evidence of hydrocarbon storage. The blue curve is a major trendline used for porosity modeling using Vp/Vs and P-impedance data. Porosity can then be inverted using the Vp, Vs, and P-impedance volumes for the available seismic cubes. This porosity definition allows determining the permeability and sealing potential of certain rocks and facies.

Data available through the New Zealand government for core sample measurements completed in 1997 provide additional information on the permeability of the system from various wells within the basin. Figure 3.12 is a cross-plot of basic core porosity and air permeability for various 6" core plugs from different wells. Correlation indicates significant permeability potential for samples with porosity higher than 10% (corresponds to permeability higher than 10 mD). Note that core plugs location selection is based towards reservoir rocks and hence has limited implication to the shalier parts of the system.

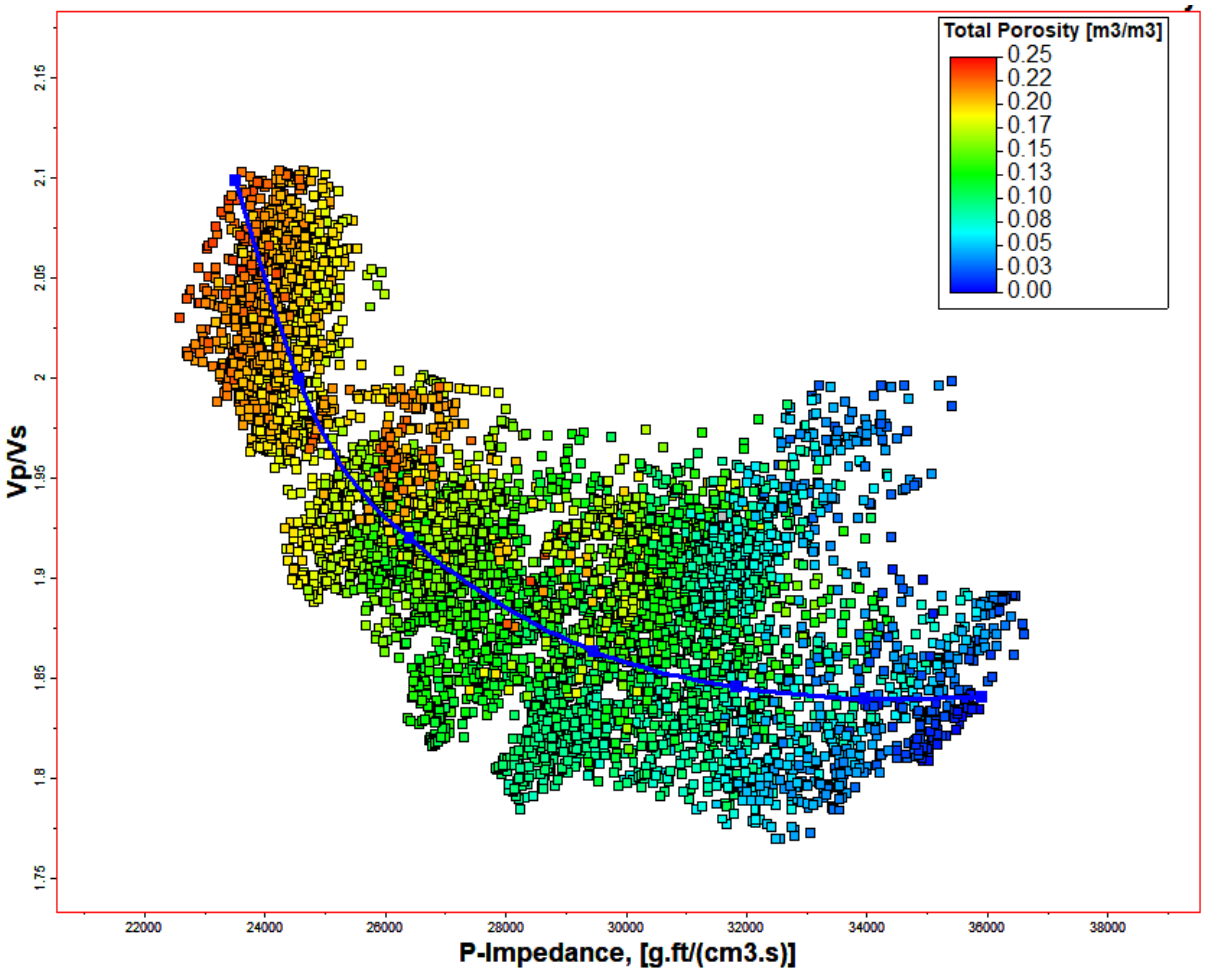


Figure 3.11. Relationship between Vp/Vs and P-Impedance colored by porosity (hot colors are higher porosity).

To better define rock properties and types, the gamma ray is compared with acoustic data to derive any possible relationships. Having a derived gamma ray log using seismic inversion will allows for proper definition of clay/mud rich rocks that are typically associated with low permeability and sealing rock. As seen through mudlog data, and other available core and logging data, the shallower part of the system is mainly a siliciclastic system defined by abundant sandstones and shales. In contrast, evidence of volcanic activity is seen mainly in the basement part of this system, structurally impacting the deposition of sediments and development of any

faults. In addition, volcanic rocks were encountered in various well across the basin (such as the Arawa #1 well). However, the depth of those rocks fall mostly below the normal en-echelon system that we are studying, and for that reason, will not impact our definition of rock facies.

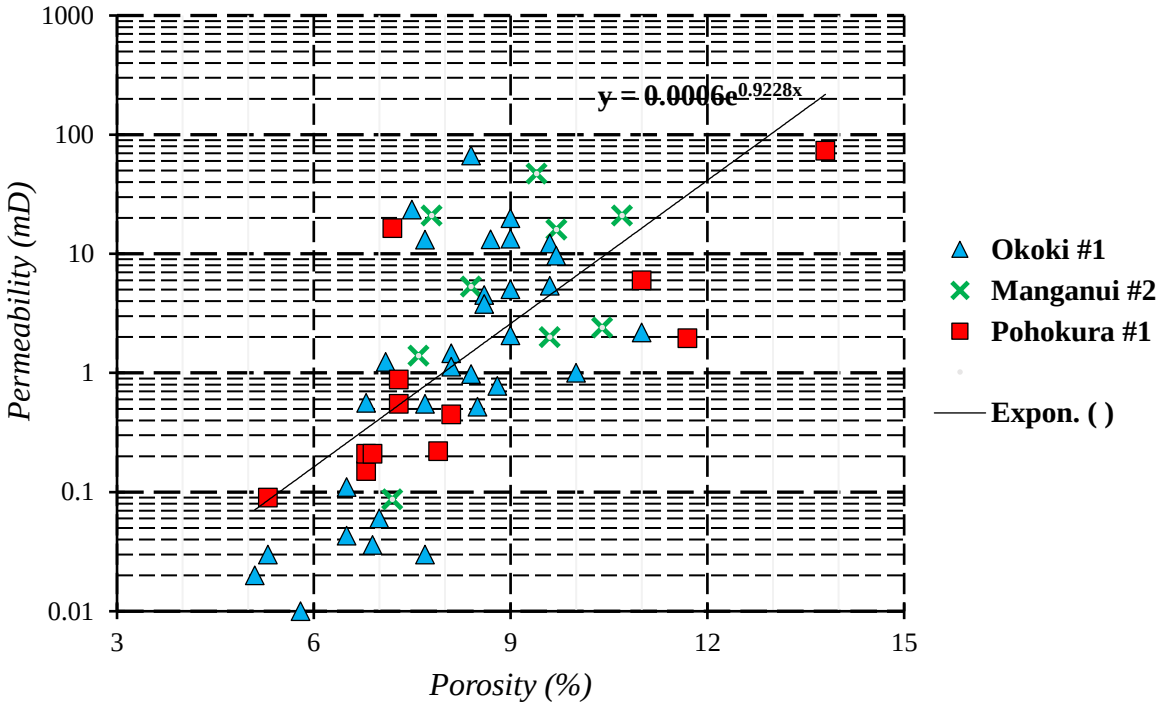


Figure 3.12. Porosity-permeability relationship from core plugs for different wells.

Figure 3.13 is a cross-plot of logged gamma ray and calculated P-impedance using density and slowness logs. Colors represent the distribution of porosity with hot colors (red) as high porosity rocks, and cool colors (blue) as tight formations. The relationship between porosity and gamma ray response is easily established, predominately sandstone rocks, defined by low gamma ray, high porosity, and high P-impedance. The trend (black line) between the P-impedance and the gamma ray logs is not very useful for the medium gamma ray range (between 60 and 100 gAPI). Despite the scatter of the data for lower P-impedances, the trend associated with high impedance and low gamma ray allows us to define rocks with lower gamma ray (mostly sandstone) associated

with higher porosity and permeability. The latter intervals are in general referred to as reservoir rocks, despite lack of hydrocarbon stored. Note that encountered volcanic rocks, mainly in the Arawa #1 well are seen to be characterized by high porosity, low gamma ray and medium impedance, hence do not fit the model.

Similarly, Figure 3.14 shows the variation of density as a function of P-impedance colored by the volume of shale (Vshale) for various wells. The plot shows two major trends, a shale trend (black) associated with higher volume of shale and a sand trend (yellow) corresponding to a low volume of shale. The shale trend tends to have a lower P-impedance and higher density corresponding to a more compacted, less porous rock. Hence those relationship established between various logged rock properties and acoustic data can be useful when applied to seismic data to invert similar rock properties such as a porosity index and Vshale.

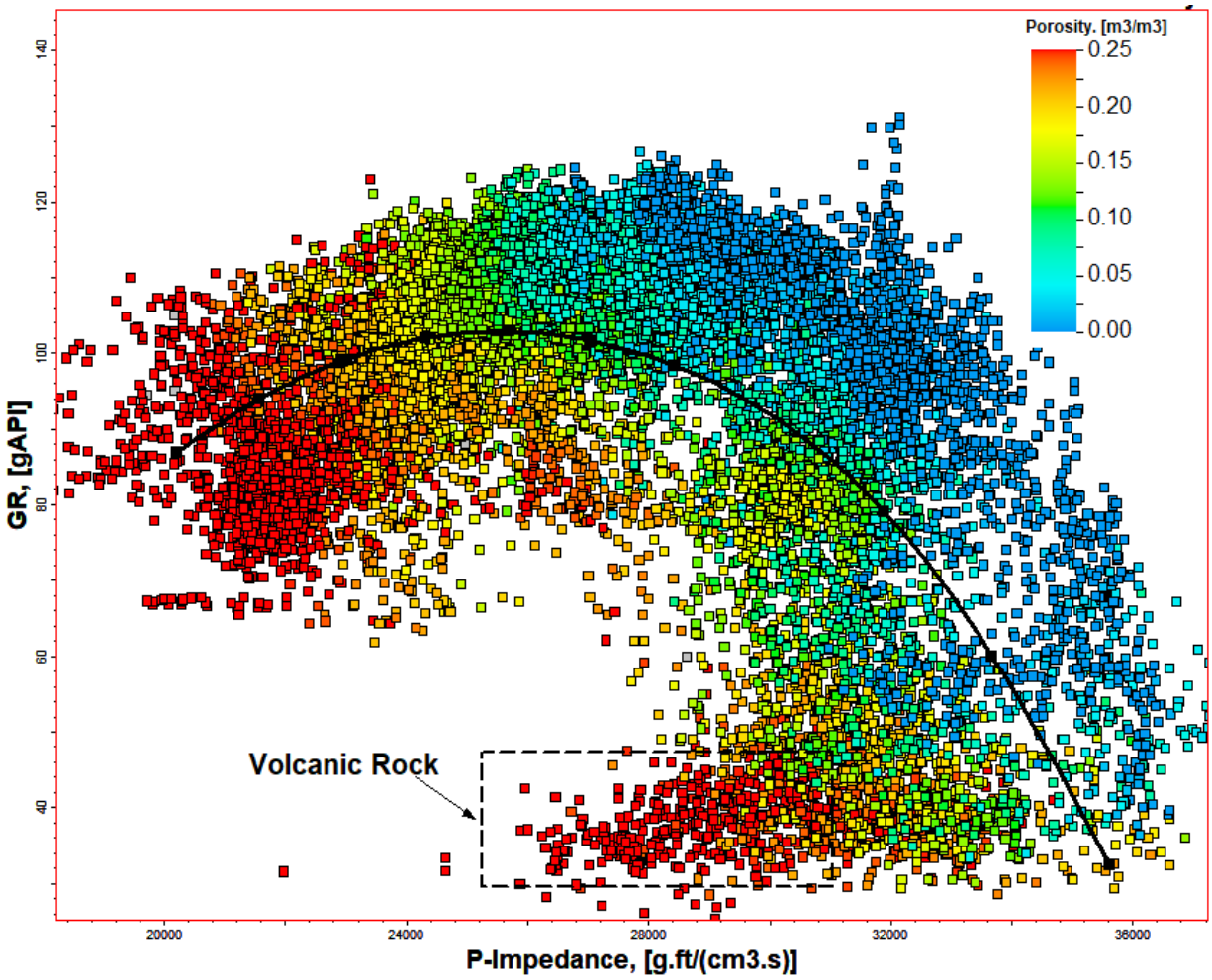


Figure 3.13. Plot showing relationship between gamma ray and P-impedance colored by derived porosity for the main wells in the area.

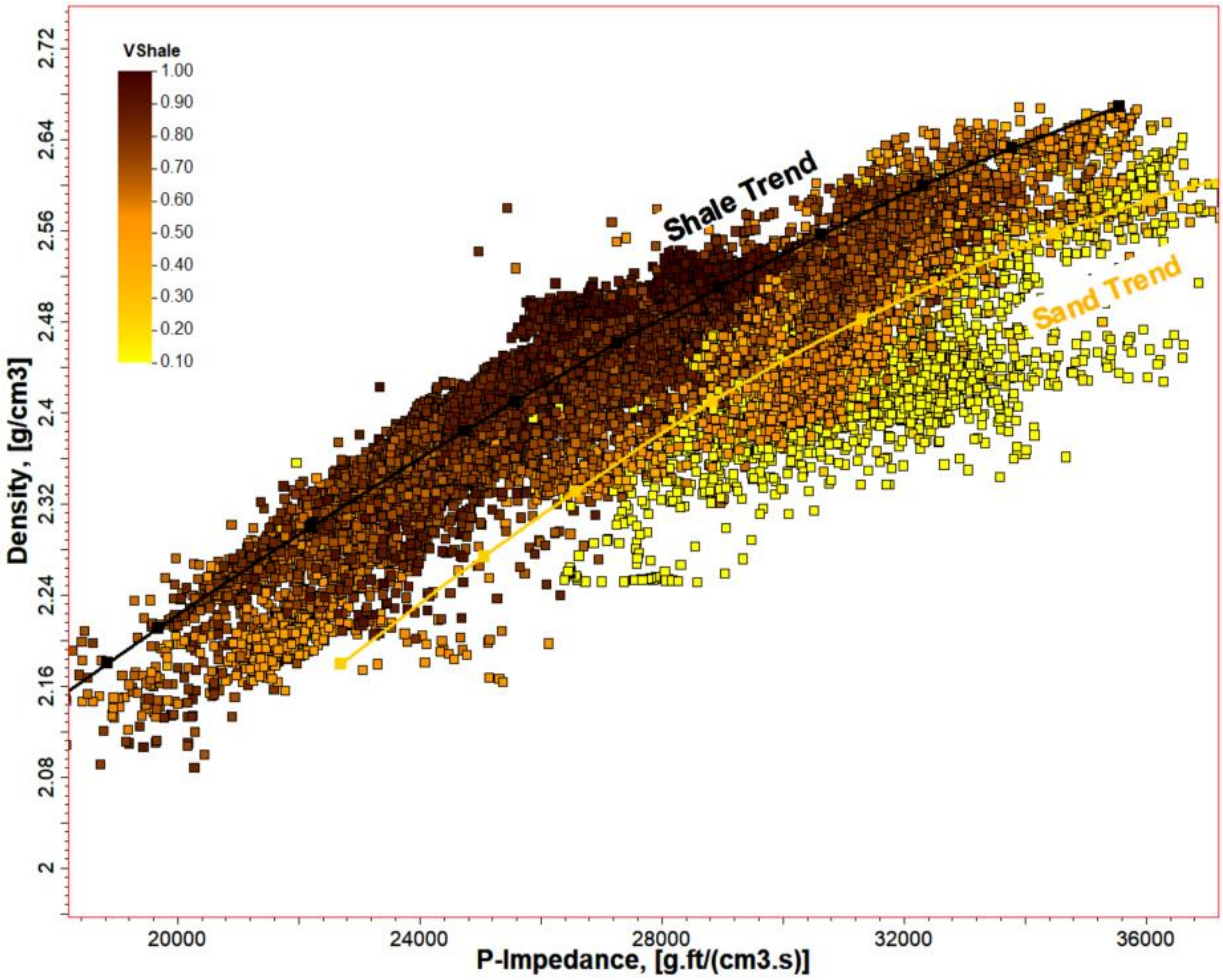


Figure 3.14. Definition of shale and sand trend using the density and P-impedance correlation colored by volume of shale.

6. INVERSION RESULTS

Inversion results include deriving Vs and density volumes which then can be used to derive other rock properties. As a quality-control measure, and to ensure a good overall predictability, a comparison between predicted properties (such as P-Impedance, S-Impedance, and density) and actual log data at each well location is needed. A set of blind well(s) can typically be used to test the accuracy of the model. Figures in the appendix show the correlation at each well location of the predicted P-impedance, S-impedance, and density with the original log data. An average correlation factor exceeding 95% with less than 15% error confirm the results seen. In addition,

Figure 3.15 shows a cross-plot of original vs predicted P-impedance for every log showing a near to 45º slope by the regression line, indicating a good predictability for our results. All inverted volumes are then converted to depth using a calibrated velocity model from well log data and check-shot data from the Arawa #1 well.

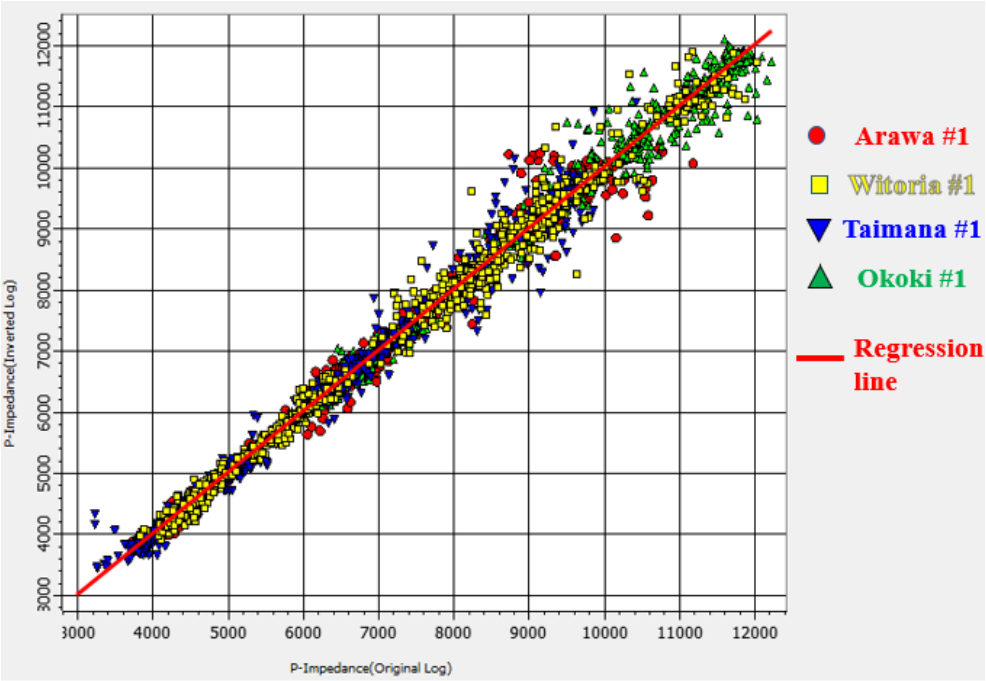


Figure 3.15. Relation between original and predicted P-impedance for various wells.

Other rock properties were estimated; a porosity index volume was generated with this inversion which is an indication for the distribution of sand within the subsurface. Calibration of this index is needed to be able to derive actual porosity results from seismic inversion. In addition, a gamma ray volume was derived from the seismic inversion volumes covering mainly the faulted area near the Arawa #1 well. Figure 3.16 is a comparison between the porosity, P-impedance, and gamma ray volumes at the inline defined on the map. This cross-section is NE-SW passing through the Arawa #1 well showing the major well tops on the upthrown side of the faulted system. Note

how the inversion honored the faulting and the associated displacement as an initial strata model containing those interpreted horizons was built prior to the inversion.

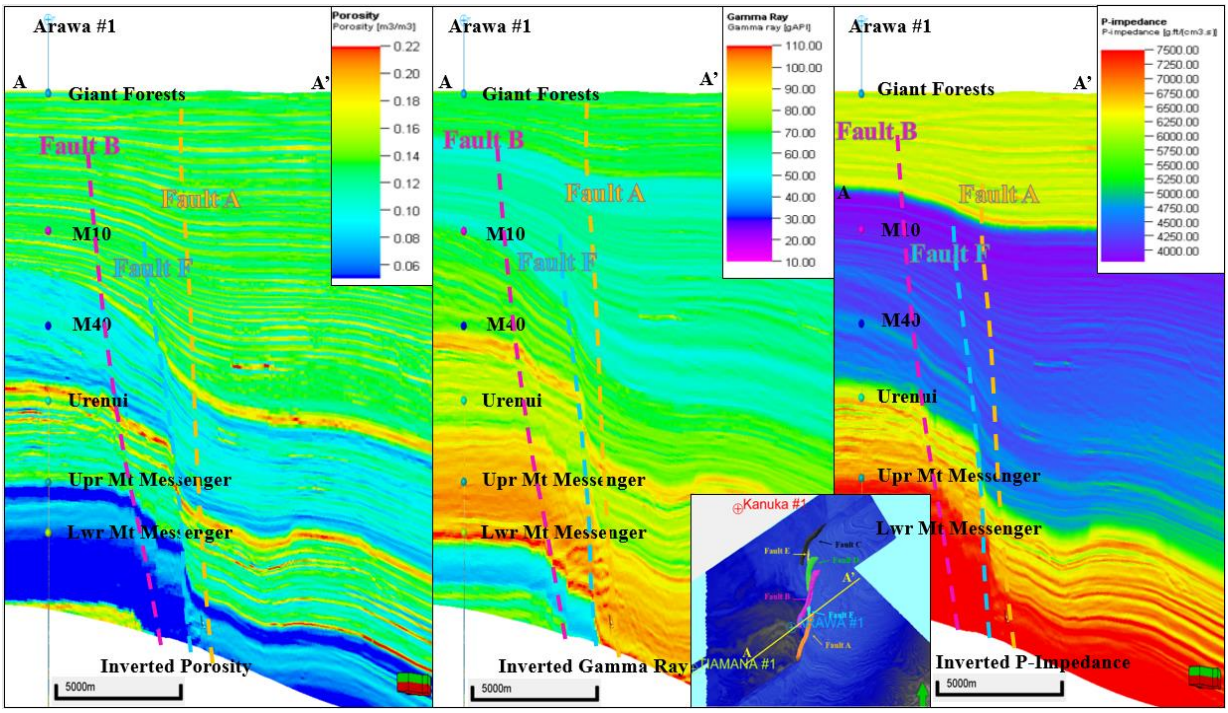


Figure 3.16. Comparison between (from the left to right) the porosity, gamma ray, and P-impedance volumes at the inline passing through the Arawa #1 well based from the inversion volumes.

A definition of facies variations is needed based on available core and cuttings collected. Figure 3.17 is a cross-plot of gamma ray and colored by defined facies. The facies definition used is derived from the mudlog reports of Arawa #1 well, the closest well to our fault system, and is characterized by four siliciclastic rock types (sand, shale or mudrock, interbedded rock, and siltstone) and a fifth volcanic rock (referred to as tuff). Volcanic rocks will not be modeled in this exercise and only a siliciclastic definition will be adopted considering the depth at which those volcanic rocks are seen. The cross-plot shows a very good definition of those facies with the porosity and gamma ray logs, which allows for a proper definition of those facies on the inverted seismic volumes (of porosity and gamma ray).

Using this relationship between porosity and gamma ray response, facies can then be derived from seismic data using inverted volumes. Figure 3.18 shows two (2) cross-sections through the derived facies volume highlighting the main faults and their associated transfer zones. Facies data available from the nearest well, Arawa #1, indicates a system that is dominated by tight shale and siltstone. However, the cross-section through the downthrown side shows a much more sand dominated system. Seismic inversion predicted sandy formations on the downthrown side, showing a structurally controlled deposition with channels and fans dumping sand within the growth units. The M10 through M40 formations, which were picked as subdivisions of the Giant Forests sequence, are the main sand-rich formations that can be great reservoirs considering their thickness, their porosity, their stratigraphic trapping, and potential structural trapping if no migration is possible due to sealing faults. This will be examined into further details by examining at fault juxtaposition and SGR of faults.

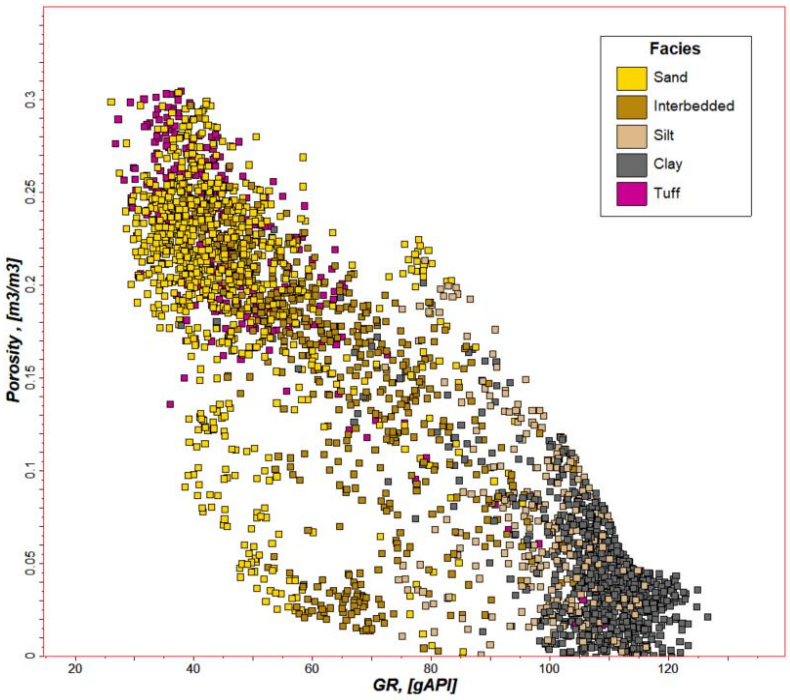


Figure 3.17. Porosity vs gamma ray colored by facies from the mudlog data available for the Arawa #1 well

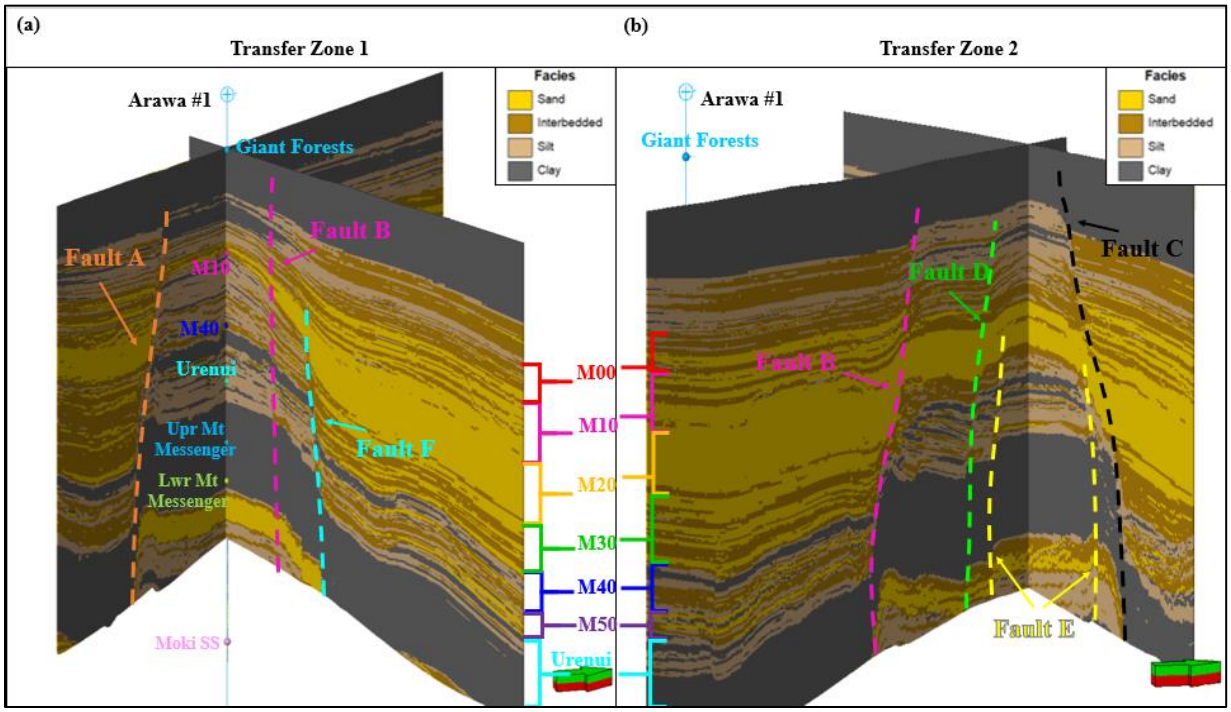


Figure 3.18. 3D view of facies distribution at both transfer zones.

7. FAULT SEAL ANALYSIS

a) 1D Well Juxtaposition Analysis

Knipe (1997) describes seal diagrams for normal faults as a three-dimensional visualization of fault throw and stratigraphic units. With the increase of throw associated with more faulting, different stratigraphic units get juxtaposed to others by tracing the footwall in the direction of displacement. Hence, when reservoir rocks are juxtaposed to tight rocks, such as shales or salt, the reservoir rocks are assumed to be sealed due to their associated stratigraphic juxtaposition.

Figure 3.19 is a seal diagram derived from the facies derived from well log data for the Arawa # 1 well. Facies were derived using a neural network by integrating gamma ray, density, porosity logs, and the described facies from the mudlog report. Juxtaposition analysis is conducted assuming a maximum throw of 800m based on the analysis of Fault A. As a result, multiple combinations of facies can be derived, but the sand to sand juxtaposition would be the most important for leaking potential. The reasoning behind considering only sand facies is based on their porosity value (averaging 20%) and corresponding permeability (>1000 mD). Figure 3.20 shows only significant combinations highlighting in green, areas of potential leaking (a) and areas of red (sand-shale), sealing potential (b). As seen in Figure 3.20 the system has a much higher tendency for sealing for the M00, M10, and M40 sands with minimal leaking potential. This analysis assumes that siltstone and interbedded formations tend to be more sealing rocks, and are thus not counted as reservoir rocks. However, this rock typing might not be sufficient, and a permeability index for each would be needed to more accurately assess the sealing potential. Note the Mokau sand was not accounted for mainly since this sand is below the shallow normal faulting system and is more impacted by basement faulting.

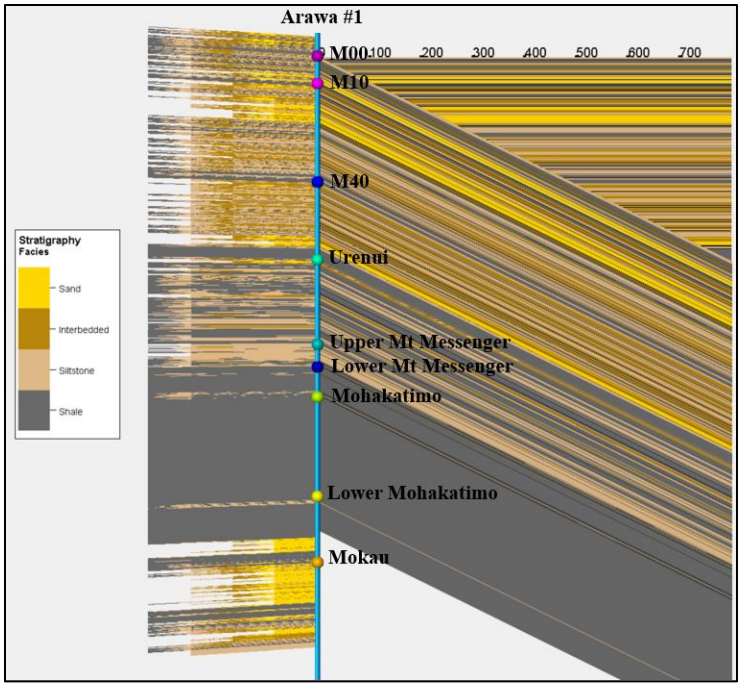


Figure 3.19. Seal diagram for the Arawa #1 well based on derived facies logs.

This 1D juxtaposition analysis can be a quick method to account for fault throw and sealing potential of certain reservoirs. However, the fundamental assumptions of this analysis are that throw, or displacement, is constant along the faults and that facies do not change laterally. However, from previous analyses, displacement along any of the faults within our system is far from being constant. Displacement tends to reach a maximum towards the middle of the fault, and a minimum at the both tips. In addition, the overall displacement profile of the system shows a decrease of displacement towards the north north-east, probably associated with initiation of faulting (from the south). At each of the transfer zones, displacement is significantly lower, causing folding, rotation, and even faulting to occur, thus making it a complex system to assess sealing potential. Hence a more robust sealing 3D juxtaposition analysis prediction method is needed.

Lastly, as seen in the inversion results of facies, seismic inversion predicted sandstone facies at the downthrown blocks. The amount of sand predicted is far from the available thin layers

of sand on the upthrown block (Arawa #1 well), hence, making 1D juxtaposition limited. Variations of facies across the fault system, most probably associated with structure, and the observed growth units, are never predictable using only well log data, and can be only completed using 3D seismic data coupled with a robust interpretation and inversion model.

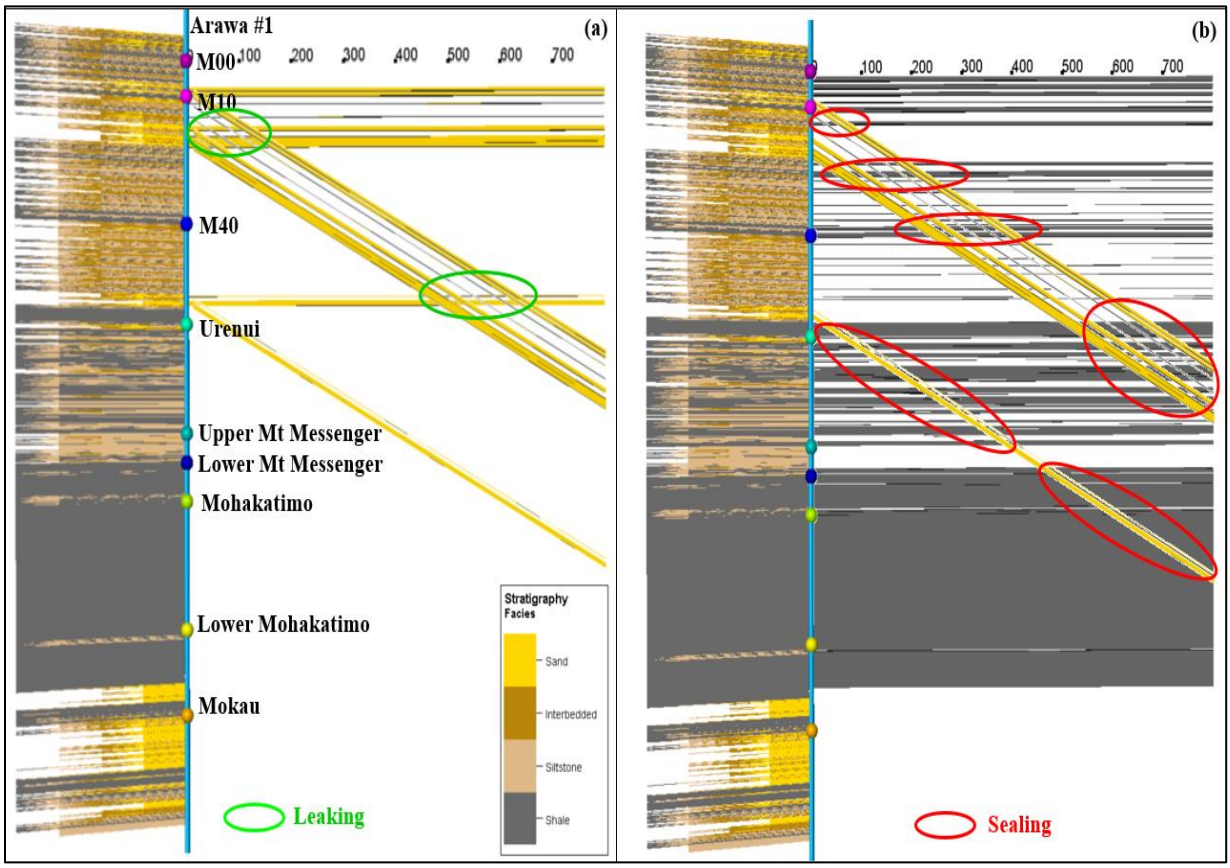


Figure 3.20. Significant combinations highlighting in green for areas of potential leaking (a) and area of red (sand-shale), sealing potential (b).

8. CONCLUSION

The Parihaka fault system consists of a set of three en-echelon faults trending NE-SW. The displacement associated with these faults shows an increase along the southern part during the Pliocene, and to the northern part during the Pleistocene. This change in displacement can be seen

in changes of bed thickness on the downthrown block and is possibly due to the rotation of the stress field.

The relay ramps connecting those faults indicate that faults gained the bulk of their length with initially small displacement. As displacement increased, the ramp lengths increased, thus connecting the major faults and causing faults to rotate and terminate against each other. Additional increases in displacement, beyond the early displacement, is shown not to translate into additional fault length increase. The width of the ramps is predefined by the original location of the faults. With additional displacement, beds within the ramps rotate about 6 degrees causing the beds to break and form smaller faults to accommodate for the additional faulting. The development of the smaller faults can be seen using seismic dip attributes.

Seismic attributes can improve the understanding of transfer zones characteristics and derive structural properties. Coherence show a positive correlation between variance and displacement. Below a certain variance value (0.6), displacement is consistent and can be calculated. This has important implications for smaller faults such as within the relay ramps and fault splays where variance can be used to detect fault displacement. Seismic curvature provides a good indication of the folding associated with the faulting. Positive curvature indicates anticlinal features, whereas negative curvature indicates synclinal features.

The application of seismic attributes to structural interpretation of transfer zones can assist in better understanding the details of the structural geometry and history of the study area. Different attributes can detect faulting propagation, deformation transfer, and bed rotation. These features as well as the effects of lithological variation on structural geometry can explain the variation in deformation styles in the fault system.

b) 3D Faults Sealing Analysis

As seen in the 1D juxtaposition analysis, a more detailed and robust model is needed to assess fault sealing potential mainly due to facies variation, displacement variation, and relay ramp related folding. This section will attempt at providing a more complete approach to fault sealing using 2 methods: 3D juxtaposition and SGR estimation.

Similar to the 1D workflow, the 3D juxtaposition workflow uses facies derived from seismic inversion mapped on each fault plane for both the upthrown and downthrown sides. The least permeable stratigraphic unit at each location, from either the upthrown or downthrown side, is then mapped onto the fault for seal analysis, assuming sand being the most permeable, and interbedded units are more permeable than siltstone and shales. Figures 3.21 (a), 3.22 (a), and 3.23 (a) show a 3D visualization of the least permeable facies along each of the faults (Faults A, B, and C respectively). The upthrown stratigraphic units are then traced onto the fault to allow for proper understanding of facies variation. A sand on sand juxtaposition, between upthrown and downthrown blocks, is considered a major migration pathway and is then contoured in black. For Fault A, most of those high permeable pathways are seen in M10 and M20, with an increase in thickness towards the northern end. M00 and M30 have few sand juxtapositions mainly seen on the northern end of the fault. Similarly, for Faults B and C, the main area of migration is seen to be across the M10 and M20 intervals (only M20 for fault C), with few permeable zones for M00, and some deeper part of M20. Similar to Fault A, Fault B shows an increase in permeable thickness on the northern side. This is most probably associated with the folding caused by relay ramps. Fault C however, shows a more continuous and uniform distribution of those sand juxtaposed rocks.

The second method used here to assess fault leaking or sealing potential is the shale gouge ratio method (or SGR) (Yields et al, 2002). This method is based on the capillary entry pressure for different pore sizes. As a fault gets displaced, material such as clay gets smeared along the fault plane within the fault core zone. As clay content within the fault damage is estimated based on the thickness and smearing of clay rich beds, a 15% to 20% of clay material is assumed enough to seal the fault. Because clay exhibits small pore sizes, its entry pressure is increased, and can thus support a higher hydrocarbon (or any over-pressured fluid) column. SGR is calculated based on the inverted gamma ray volume from which a volume of shale is derived and mapped onto the faults. SGR will be estimated based on the clay beds thickness, the amount of displacement, and the probability that clay smear is continuous.

Figures 3.21 (b), 3.22 (b), and 3.23 (b) shows the estimated SGR percentage for each fault (Faults A, B, and C respectively) based on the available inversion data. As it was discussed, an SGR ratio of less than 20% is considered to be a migration pathway. Hence, SGR less than 20% is then colored in light blue and highlighted for each fault with black boundary. The areas highlighted for each fault, having low SGR, are seen to match the location of sand to sand juxtaposition. Similarly, those areas tend to be thicker on the northern edge of Fault A and B, and on both edges of Fault C (thinner towards the center of the fault). This is related to the lower displacement amount at each tip of fault, and the higher displacement towards the center of the fault. However, the juxtaposition method shows a much wider, more continuous, and longer surface area of highly permeable rock compared to the SGR method.

In addition, as seen in both methods, the highly permeable areas tend to be mostly located on the edge of each fault. This observation matches the location of the transfer zone, as formation displacement can vary across those zones, and the existing of other faults can complicate the

sealing analysis. For that purpose, a transfer zone analysis approach is suggested to a better understand the sealing potential of transfer zones.

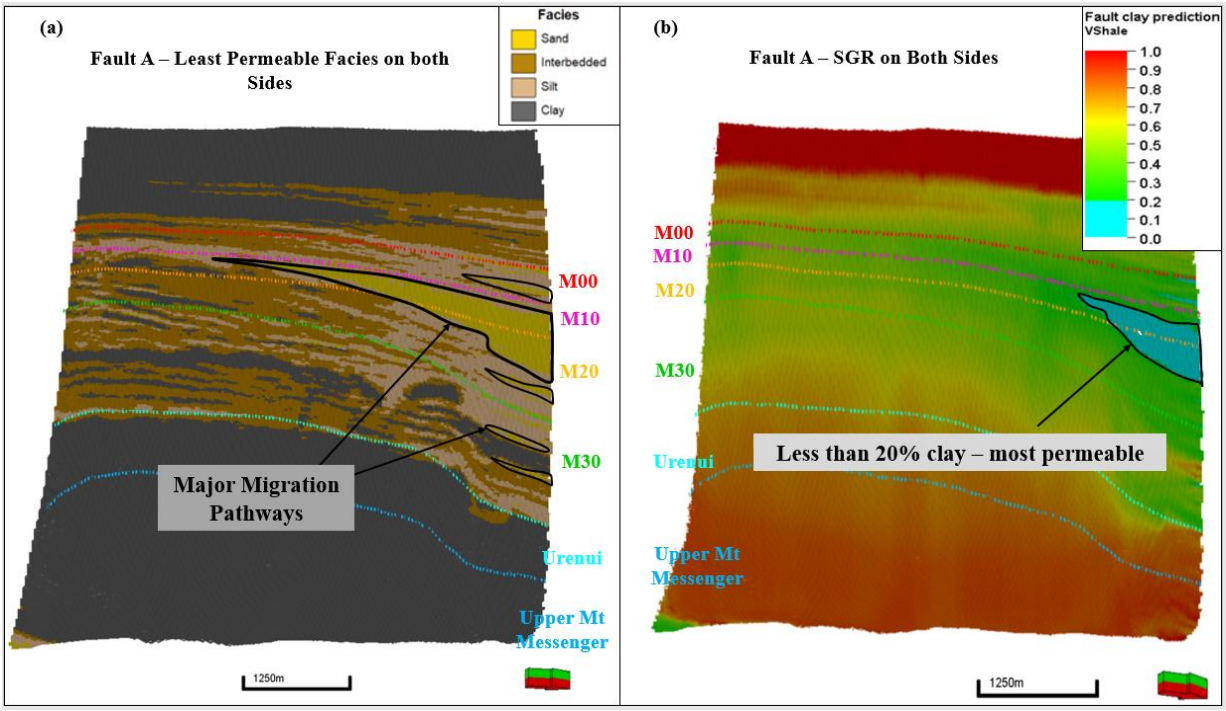


Figure 3.21. Looking face on the fault plane (a) 3D visualization of the least permeable facies along fault A, (b) 3D visualization of the SGR estimated for Fault A.

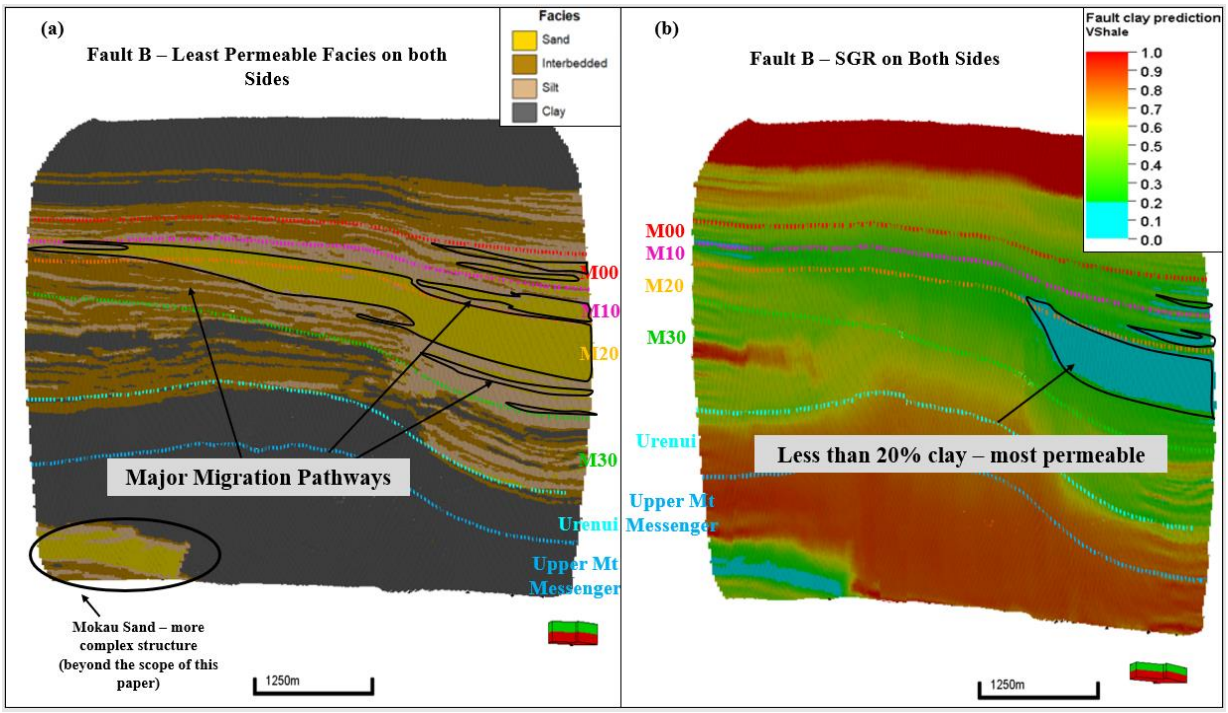


Figure 3.22. Looking face on the fault plane (a) 3D visualization of the least permeable facies along fault B, (b) 3D visualization of the SGR estimated for Fault B.

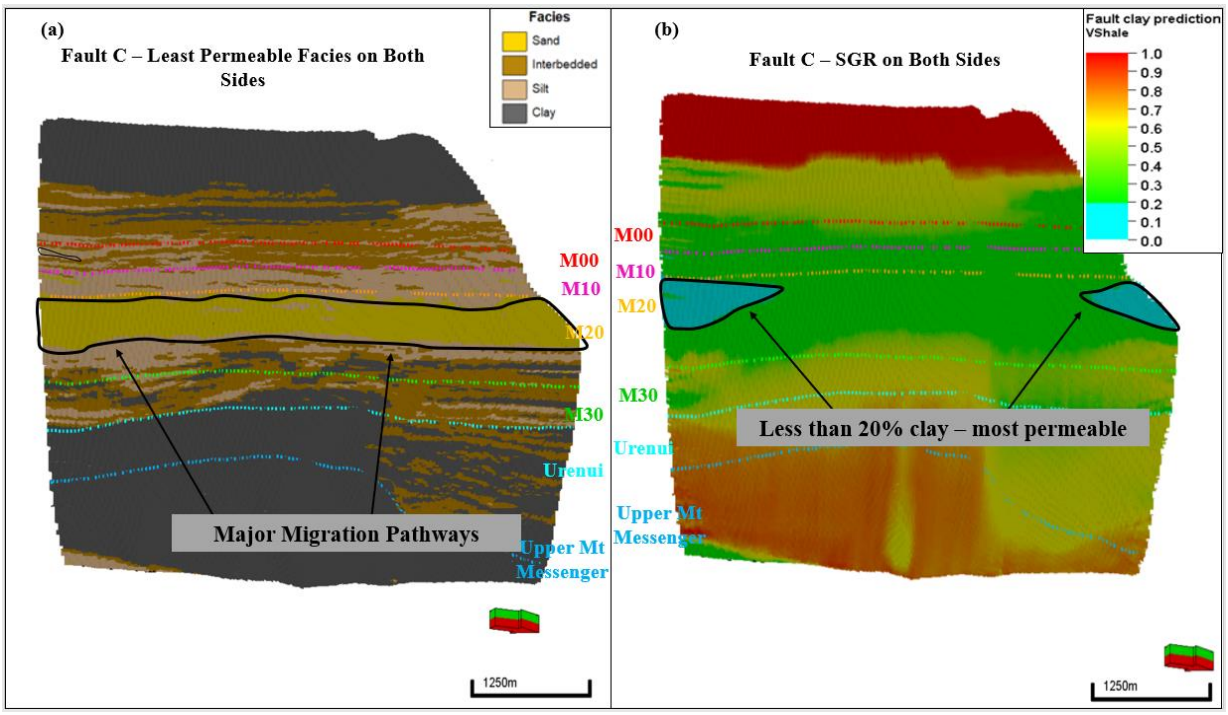


Figure 3.23. Looking face on the fault plane (a) 3D visualization of the least permeable facies along fault B, (b) 3D visualization of the SGR estimated for Fault C.

c) Transfer Zone Sealing Analysis

Transfer zones have always been considered as great migration pathways connecting the upthrown and downthrown sides of the any formation, most of the time, in a smooth variation of displacement magnitude (Morley et al. 2004; Peacock et al. 1994). Depending on rock properties, laterally associated with lithology (will be discussed in more detail in the next chapter) and degree of deformation, transfer zones can serve as excellent vertical migration pathways considering the degree of fracturing that they undergo associated with folding, rotating, and stretching beds. However, it has been shown in many locations that transfer zones are great reservoirs and traps as well. Their sealing potential is driven by the amount of faulting and displacement that they undergo, and thus, their compartmentalization tendencies.

To assess sealing potential of transfer zones within our area of analysis, our workflow is based on using, similar to the fault sealing analysis, both the juxtaposition and SGR methods. However, those parameters are considered on a map scale for each individual zone, hence carrying with it a pseudo 3D understanding.

Figures 3.24, 3.25, 3.26 are map views of the M00, M10, and M20 intervals, respectively, colored by sand facies interval thickness (darker is thicker) and assessed for sealing potential using both methods: (a) stratigraphic juxtaposition and (b) the SGR method. Each map contains the fault traces in black and an average fault property for each interval. Figures 3.34(a), 3.25(a) and 3.26(a) show the permeable facies, sand facies, thickness along every fault with darker color being thicker sand package. Figures 3.24(b), 3.25(b) and 3.26(b) show the average SGR ration for each fault with less than 20% SGR colored by light blue. Green arrows indicate migration pathways while red arrows indicate sealing, at different locations from the downthrown to the upthrown side of every fault.

Similar to the fault sealing analysis, results using the transfer zone analysis indicate variations in properties for both methods, such that the stratigraphic juxtaposition method is a more conservative method in terms of fault sealing potential. Table 3.1 summarizes the analysis results for each transfer zone, at each zone, and for both methods. Almost all transfer zones results indicate a leaking potential with only transfer zone 1 for M20 using the SGR method showing a sealing zone. As displacement increases, transfer zones develop internal faults, referred to as breach zones, as the ramp is unable to account for an increase in displacement without faulting. The juxtaposition method for this breach fault (fault F), indicates permeable rocks, such as sand facies, on both sides of the fault with medium thickness thus allowing fluid migration. This can be due to the lower displacement than observed on the major faults.

However, using the shale gouge ratio method, this fault is estimated to have about 30-40% shale gouge within its fault core, hence, having potential sealing capability for M20. Assuming that the rock is not vertically fractured to cause vertical fluid seepage, transfer zone 1 can potentially be assessed as a structural trap or a reservoir compartment, defined by the thick downthrown sand, and the sealing fault (Fault F which is a breaching fault developing between Fault A and B). Similarly, the compartment formed within the close proximity to transfer zone 2 defined by the closure associated with Fault B and D can be as well another structural trap for interval M00 and M10. Based on the clay smearing potential, this is a sealing membrane.

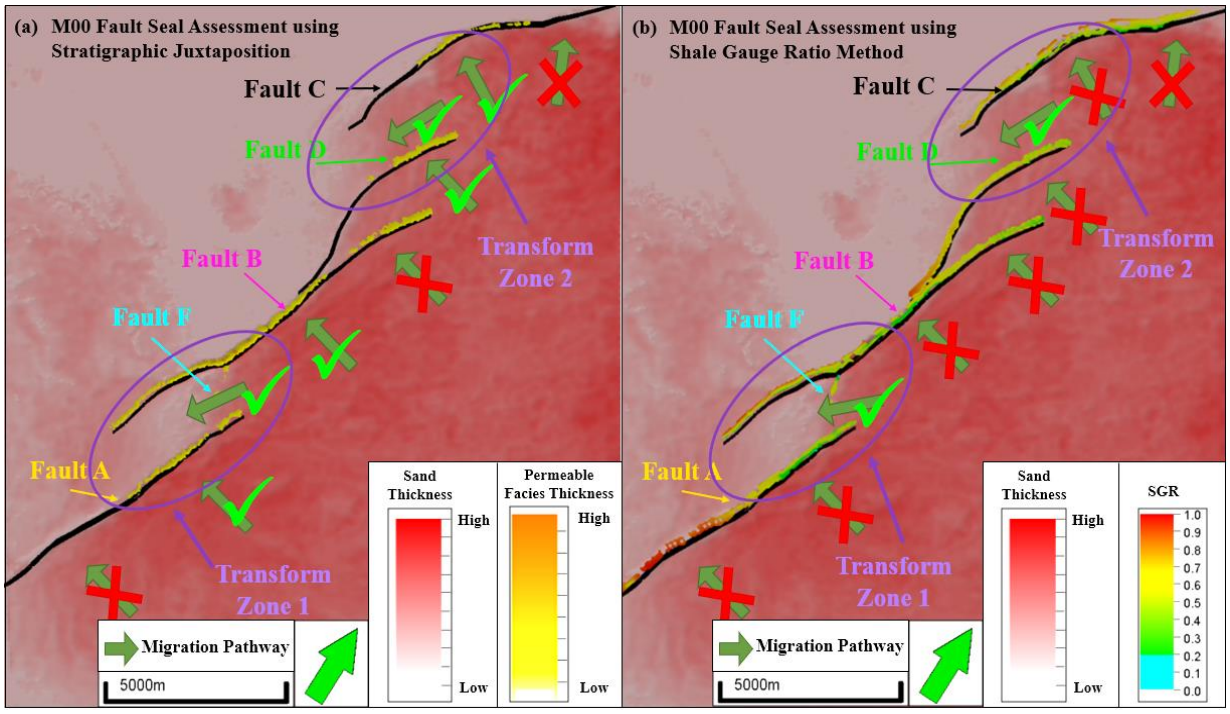


Figure 3.24. Map views of the M00 intervals colored by sand facies interval thickness (darker is thicker) and assessed for sealing potential using both methods: (a) stratigraphic juxtaposition and (b) SGR method.

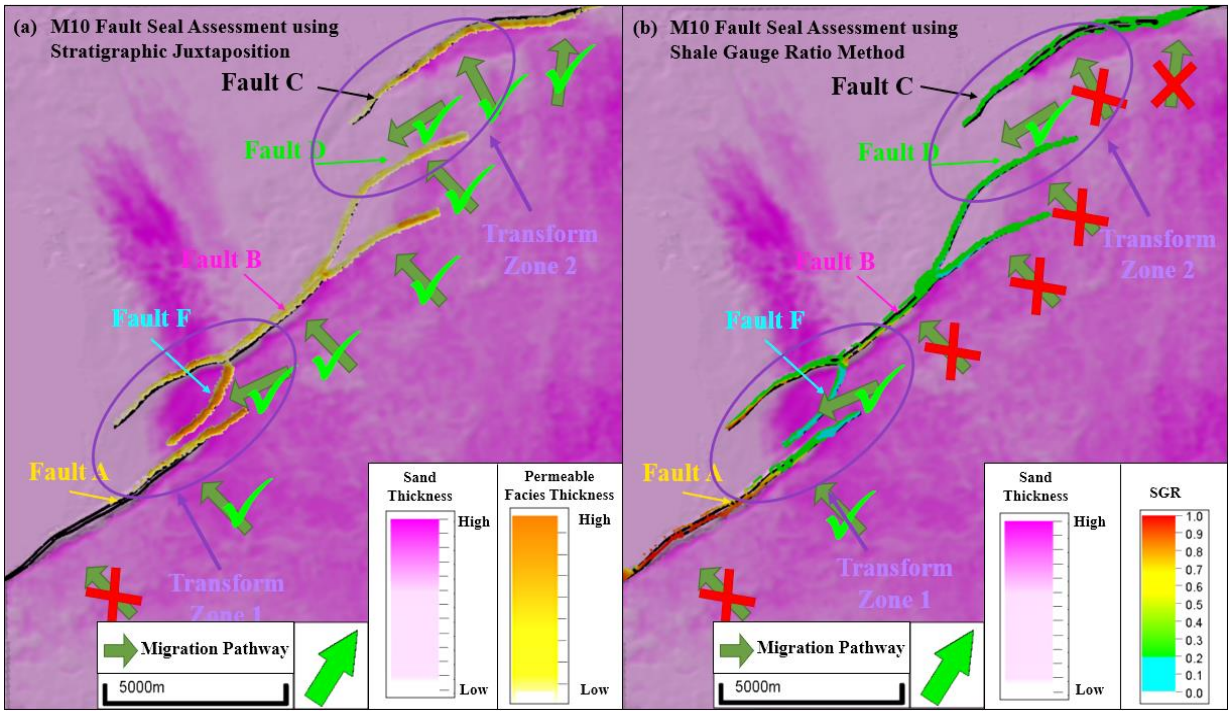


Figure 3.25. Map views of the M10 intervals colored by sand facies interval thickness (darker is thicker) and assessed for sealing potential using both methods: (a) stratigraphic juxtaposition and (b) SGR method.

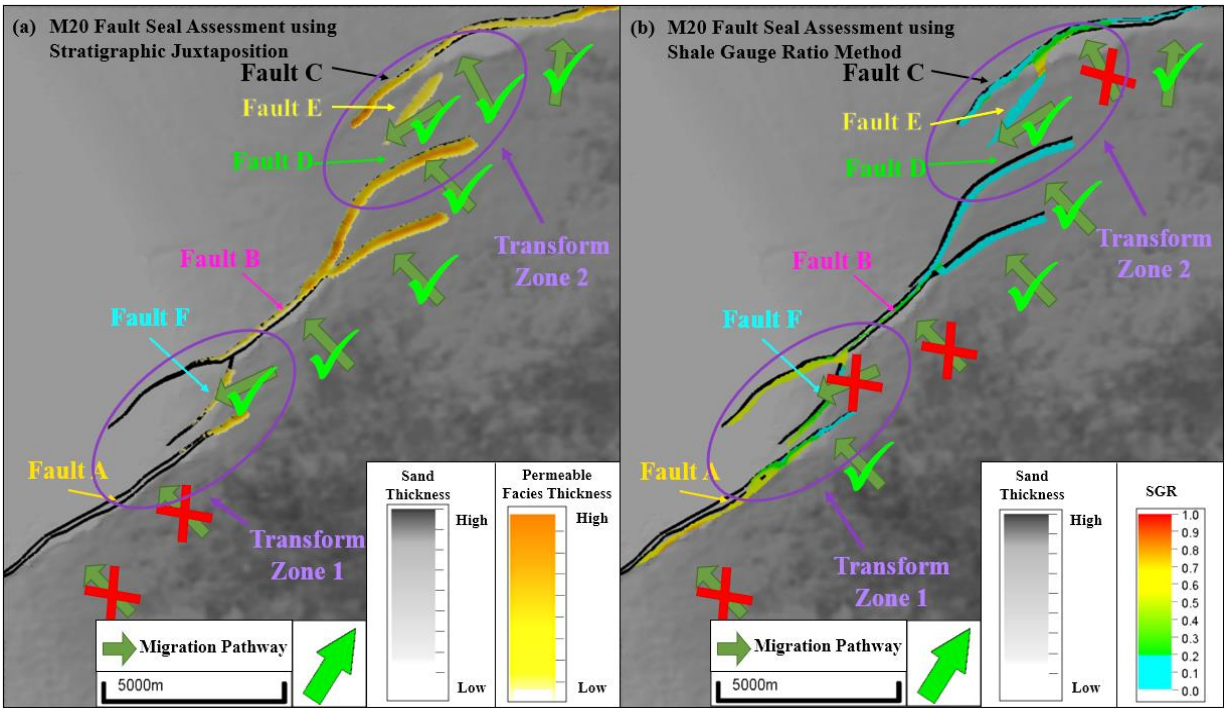


Figure 3.26. Map views of the M20 intervals colored by sand facies interval thickness (darker is thicker) and assessed for sealing potential using both methods: (a) stratigraphic juxtaposition and (b) SGR method.

Table 3.1. Summary of the transfer zone analysis results at each zone using both stratigraphic juxtaposition and SGR methods.

Formation	Transfer Zone	Stratigraphic Juxtaposition	SGR
M00	**TZ 1**	Leaking	Leaking
	TZ 2	Leaking	Leaking
M10	**TZ 1**	Leaking	Leaking
	TZ 2	Leaking	Leaking
M20	**TZ 1**	Leaking	Leaking
	TZ 2	Leaking	Sealing

9. CONCLUSIONS

This chapter assesses fault sealing potential which is a critical component of any exploration risk analysis exercise. We developed a workflow based on derived rock property volumes (such as gamma ray, and porosity) from seismic impedance inversion to define rock types and facies. As a result, a 3D analysis can be performed providing a much more understanding on sealing potential compared to the traditional 1D juxtaposition method.

The limitations of the 1D juxtaposition method are that it does not account for the changes in displacement along the fault, such as the changes seen in transfer zones. By definition, transfer zones, and ramps that connect the upthrown and downthrown blocks by transferring displacement beneath them. Based on the inversion results, we find more abundance of sand facies on the downthrown side of the faults associated with depositional settings, controlled by structural changes. This variation in lithology can only be accounted for using a 3D fault sealing model.

Two methods were used to determine sealing potential: (a) stratigraphic juxtaposition and (b) SGR estimation. Stratigraphic juxtaposition indicates a higher tendency of faults to leak and sand is available on both sides of the fault. SGR estimation indicates that most faults are sealing with at least 20% clay smear, except in transfer zones. Sandy formations have been shown to be leaking at the edges of the fault caused by transfer zones, where displacement is lower.

As a result of our analysis, transfer zones can be migration pathways allowing for fluid migration from one side to the other of the fault system. However, in cases where transfer zones undergo significant deformation, faulting can develop along those ramps breaking them into smaller blocks and thus creating, in some instances, sealed compartments. Other sealed compartments can also be found near transfer zones caused by the splay of fault tips and significant displacement that those faults take.

Finally, the work presented here assumes that major migration pathways are associated with seismically visible faults. However, rocks can break and fracture into many splays and sub-seismic faults that are harder to map and assess for sealing capacity. In addition, dependent on the lithological variation of the rock, certain lithologies have a higher tendency to break or develop vertical fractures, which then can create vertical migration pathways for the fluid in the system.

CHAPTER 4: LITHOLOGICAL CONTROLS ON TRANSFER ZONES

Understanding fault geometry and shape is key to elucidating the deformation history that an area might have undergone. In this chapter, we will use experimental models in determining fault geometry, shape, and other properties associated with the formation of transfer zones particularly for convergent fault system. The work will first study the impact of connecting fault bends or the relative location of convergent faults on the variability of deformation and distribution of faulting and fracturing associated with extension. Secondly, clay and cement like materials were used as analogs for ductile or soft and brittle or hard rocks respectively. Results from those experiments address the lithological impact on fracturing using brittle and ductile layers. Then natural examples from outcrops and seismic data are analyzed to show similarity with experimental models.

1. INTRODUCTION

Analogue experimental models present a simple way to model structurally complex problems and better understand their geometries and history. Multiple experiments have been conducted to simulate the formation of rift basins using quartz sand, representing a brittle layer (Sagy and Hamiel 2016, Basile and Brun, 1999, McClay et al, 2002, and Hus et al 2005) and others using wet clay for a better definition of the fault at the surface (Dooley and Schreurs 2012, Mitra and Paul 2011, Paul and Mitra 2013, and 2015). The choice of using wet clay-like material is for a better definition of fault geometries (Paul and Mitra, 2013) where clay is an analog for a more ductile formation (Naylor et al, 1986).

Dooley and Schreurs (2012) summarize the use of wet clay and dry sand in experimental models where clay is generally agreed to deform according to the Coulomb failure criterion with appropriate cohesive strength and optimal density (1.6-1.63 g/cm^3). However, dry sand deforms

mainly by frictional sliding with little folding but allows for easy placement and growth unit visualization. In these experiments, a more brittle material was needed to study the impact of faulting in hard rocks such as carbonates. For that reason, cement, with relatively lower density than clay and higher cohesive strength was used in the experiment.

The geometry of pull apart basins have been studied for different setups including using a rigid block such as plexiglass and foam base (Zwaan et al 2016), hard clay with pre-existing cuts (Paul and Mitra 2013) or a rubbery sheet (McClay et al 2002). Results show that the final geometry of the transfer zone is controlled by multiple parameters including pre-existing faults, direction of stress, fault propagation, amount of displacement, fault interaction, material strength, and the presence of a detachment layer.

Ferrill and Morris (2008) examined outcrops from southeast Texas to address the impact of mechanical strength of different lithologies on fault propagation and relay ramp growth. They grouped lithologies observed into two groups, competent lithologies such as dolomite and limestone, and incompetent lithologies such as shale and anhydrite. Similar to the work of Peacock (2002) and Fossen et al (2016), faults are believed to initiate in rock that is more competent and then propagate and bend when reaching less competent rocks. Figure 4.1 summarizes the work that they did where it shows the different fault geometries and relay ramp deformation due to the variation in mechanical strength associated with different lithologies. The plots shown present three cases, representation of faulting within competent strata, incompetent strata, or mixed strata.

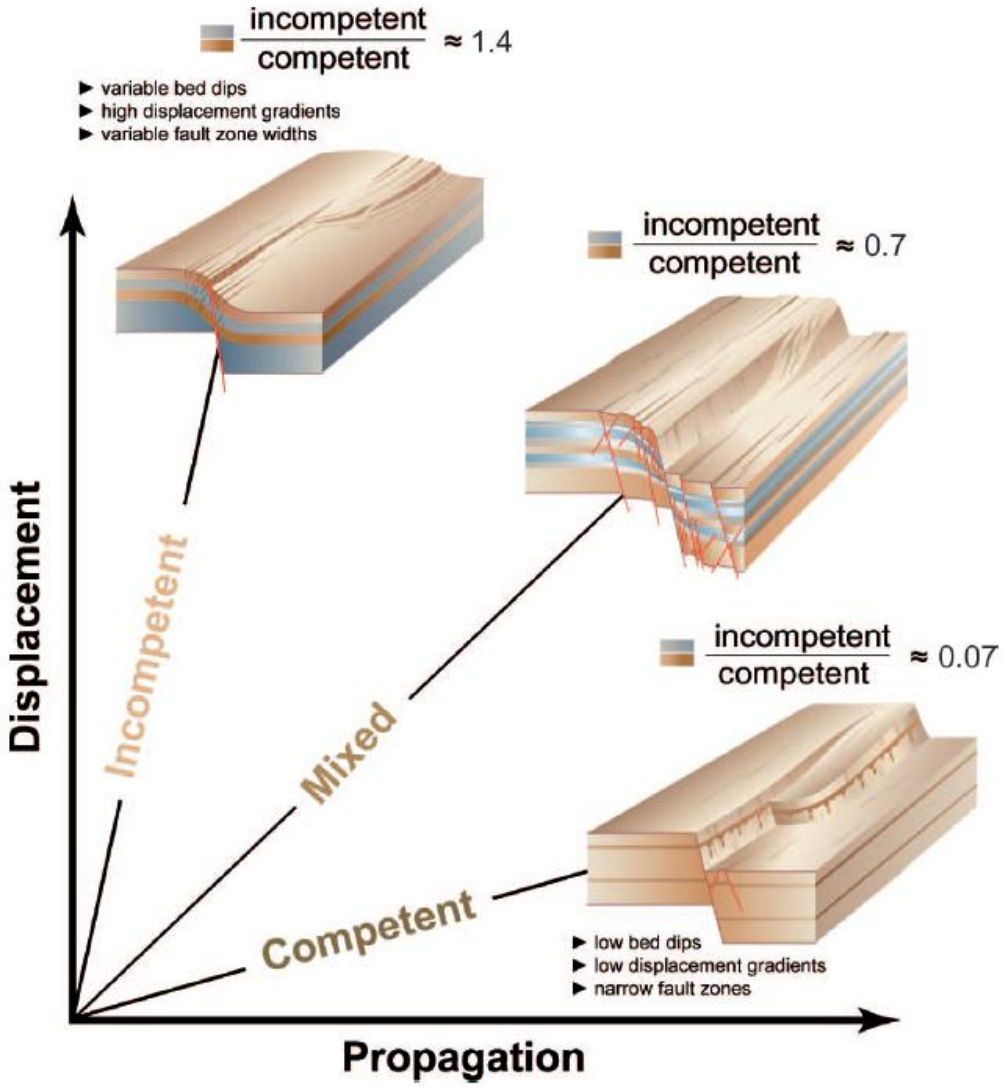


Figure 4.1. Influence of mechanical stratigraphy on fault growth and for relay ramp development (Ferrill and Morris, 2008)

Competent strata is mainly carbonate rocks similar to the Edwards Limestone. Beds described in that area show little tilting, generally less than 5˚, with minimal changes caused by faulting. Faults tend to develop in the footwall and hanging wall, exhibiting catalclastic texture and irregularity of the fault surface due to fault segmentation. Calcite cementation indicates multiphases of deformation.

Ferrill and Morris's (2008) second end member includes incompetent strata such as the Del Rio, Buda, and Eagle Ford formations. Outcrop observations show the steepening beds towards a major fault with small antithetic normal faults. The dip steepens further up to 45˚ within the main fault zone creating monocline and different scale fractures.

Ferrill and Morris's (2008) third end member to mixed lithologies such as the Glen Rose formation. The deformation is intermediate to the other two cases exhibiting rotated beds, steeply dipping faults, synthetic dip planes with small displacement faults, and shale being smeared along the fault planes.

These outcrop observations provide insight into the structural deformation by which relay ramps transfer slip from one fault to the other. Those observation match what was observed in experimental models in regard to lithological implications on transfer zone evolution. Note that experimental models can be used as analog to natural examples and they serve to better visualize the deformation. However, there are certain limitations of those models, particularly when it comes to scaling, fracture density and distribution, and bed deformation. Results seen in experiments do not necessary existing in nature.

2. EXPERIMENTAL SETUP:

The setup used in my experiments is similar to the setup described by Paul and Mitra (2013) and Bose and Mitra (2010) where clay is placed in between two backstops, one is fixed while the other one is pulling away at a constant rate of extension. The initial box dimension is set at 20 by 12 inches where the longer edges are unconstrained to eliminate any boundary effect caused by drag on the edge of the model. Flat plates overlying each other were attached to each backstop such the one attached to the moveable backstop has a defined cut to simulate pre-existing basement faults or localized zones for fault initiation. The setups of those plates allow for the formation of

convergent faults dipping towards each other with a mini-basin inbetween. Three different preexisting geometries were tested where the angle connecting both faults is respectively 90º, 105º, and 135º. The purpose is to study the impact of the transfer zone length for approaching convergent faults.

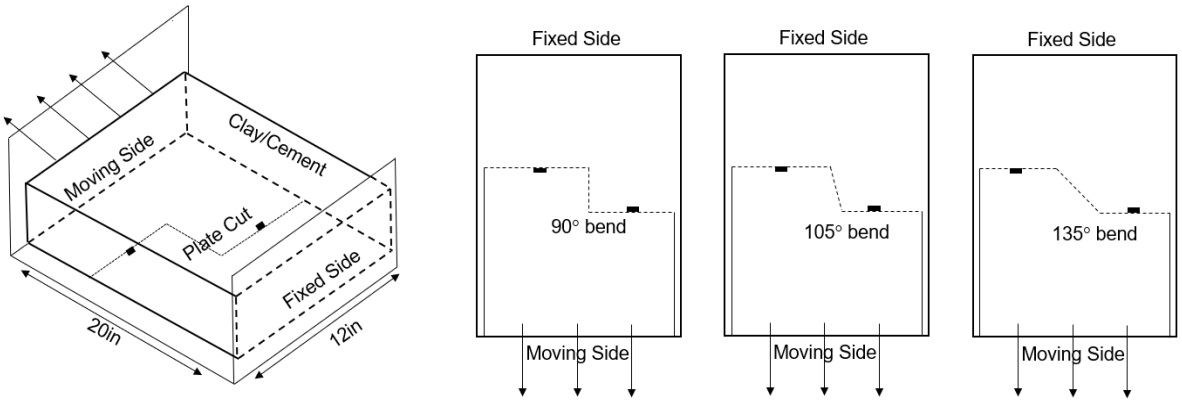


Figure 4.2. Experimental setup showing a 3D view of the apparatus used and the three plate cuts used study bend angle impact.

In order to study the lithological importance in fault growth and distribution, a soft wet clay material with a density of 1.60 to 1.65g/cm^3 (similar to Bose and Mitra, 2010) was used to simulate ductile formations such as the Eagleford Shale described by Ferrill and Morris (2008). Similarly, to capture the brittle competency of the Edwards Limestone, hard clay mixed with cement material was used. The experiment was conducted at constant room temperature with high humidity to limit the effect of water evaporation, hence material hardness, and water was added, particularly to the cement material, for optimal workability and consistency.

Table 4.1. Summary of the experiments conducted and their corresponding properties.

Experiment	Material	Bend (Degree)
1	Ductile	90
2	Ductile	105
3	Ductile	135
4	Brittle	90
5	Brittle	105
6	Brittle	135

A total of 3 inches of material was placed on the plates and flattened to have a smooth surface and edges and eliminate air bubble in it. As the experiments begin, pictures were taken at different timesteps from the top of the clay or cement material, and a 3D scanner placed above the experiment is used to capture light reflected from the clay and compute coordinates of the surfaces using the triangulation method (Bose and Mitra, 2010 and Paul and Mitra, 2013). Data points were then taken into Petrel to be visualized and a where a 3D model was built to understand the different cases.

3. EXPERIMENTAL RESULTS

a) Ductile Models:

A total of three experiments with ductile like material were conducted, each corresponding to the three different fault setups. Observations at the end of the experiments show an overall subtle structure with a faulted zone at the location of pre-existing faults. Those faulted zones, similar to what was described by Bose and Mitra (2010) are characterized by many small displacement faults. At the beginning of the experiment, the main faults propagate to the top of the clay with a gentle drape trending mostly perpendicular to the extension direction (east-west). Those faults do not form right above the plate edges but tend to be associated with the folding of the clay caused by

the increase in accommodation. As the secondary synthetic and antithetic faults develop, the orientation of those faults rotates to NW-SE to allow for the transfer of displacement. The width of the fractured zone increases with the progressive evolution of the structure showing a wide gentle "damage zone" characterized by small connected faults, turned beds, and highly fractures zones. Figure 4.3 shows the shape of the final structure of the relay ramp of Experiment 1 showing turning beds up to 30º dip.

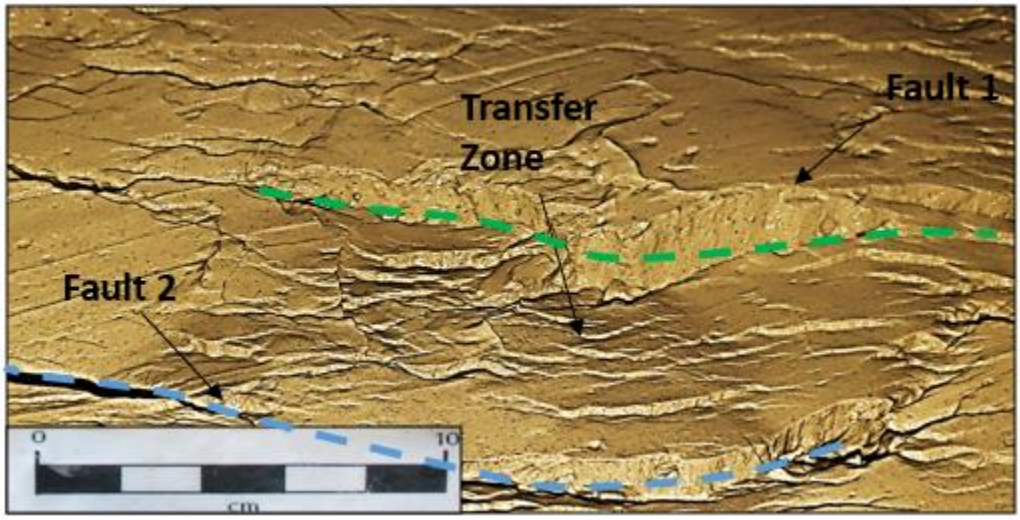


Figure 4.3. 3D view of the transfer zone at the end of Experiment 1 showing the bed tilting and significant faulting with the relay ramp.

Figure 4.4 shows a detailed evolution of the structure at three stages (A, B, C corresponding to beginning of faulting, midway, and final faulting stage) using top pictures and by tracing the fault geometries. By examining fault density, the distribution of the mapped faults shows a much different final condition for the three cases. Experiment 1 shows a near vertical separation of fractures at the 90º location where fractures are mainly east-west. Compared to Experiment 2, fractures within the transfer zone trend NW-SE at about 45º. For Experiment 3, the distribution of is almost homogeneous in pseudo E/SE-W/NW trend indicating that the two major faults are connected and are acting as a one big major fault zone

In addition, the moving block of the experiments shows a much higher fracture density that keeps on increasing with the increase of displacement. This density is characterized by antithetic faults to the major displacement direction and rollover structures. The increase of fractures is greatly related to the folding associated with the increase in deformation. Clay material have high ductility but low cohesion which causes it to bend and breaks easily.

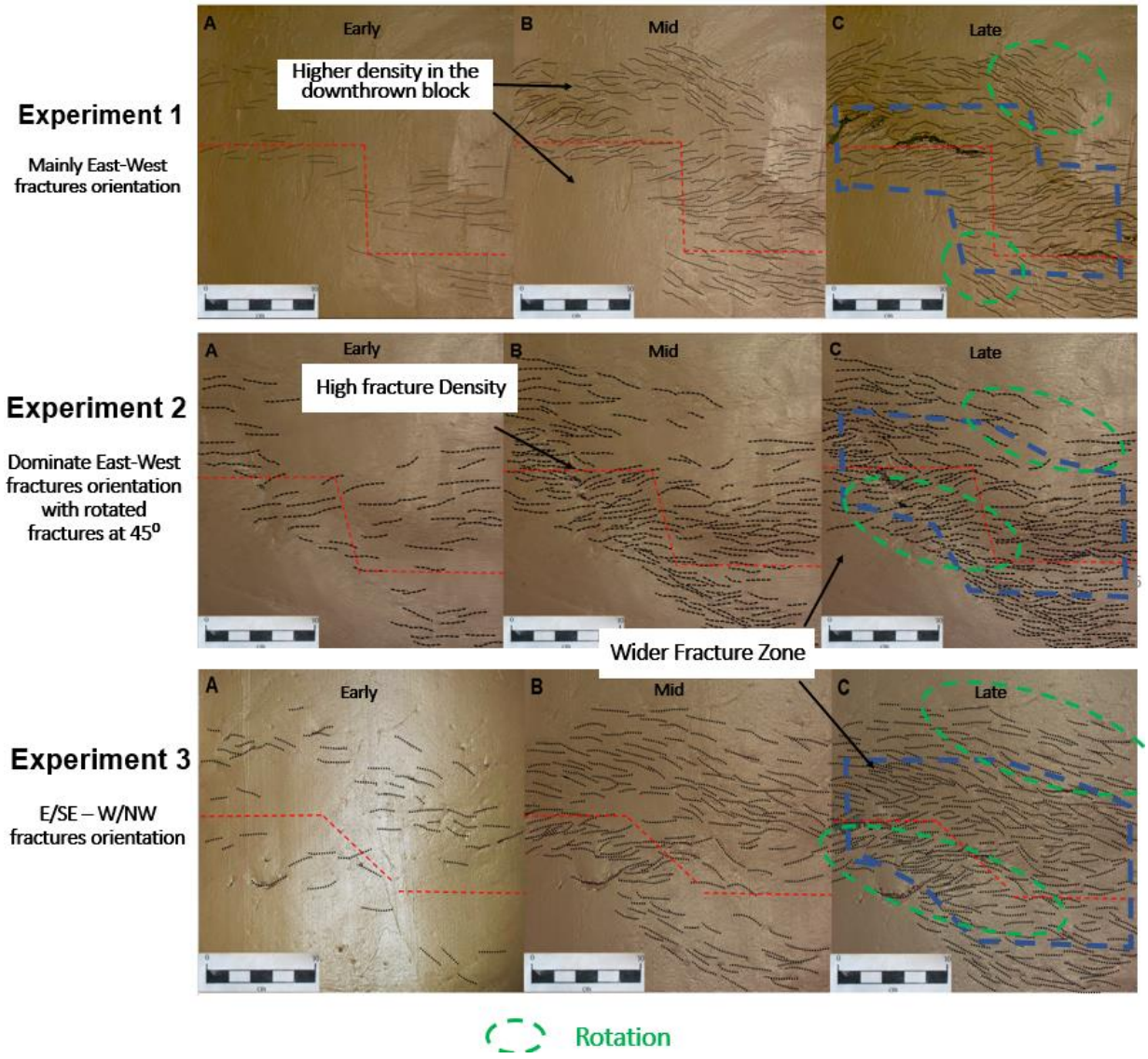


Figure 4.4. Detailed evolution of the structure at three stages (early, mid, and late corresponding to beginning of faulting, midway, and final faulting stage) for Experiments 1, 2, and 3.

The final structure of each experiment was modeled and built in Petrel for a better visualization of the internal geometries within the transfer zone (Figure 4.5). Experiment 1 defined by a 90º bend angle, is characterized by two folded and faulted zones, or grabens, that are dipping towards each other and separated by a saddle-shape ridge between the two zones. The orientation of the ridge is east-west aligning with the orientation of the pre-existing fault and the overall orientation of the faulted zones. However, faults on the edges of the transfer zone tend to be curved forming a NW-SE trended basin at about 35º.

As the angle within the bend increases (Experiment 2 and 3), indicating a smoother transfer from one fault to the other, the basin takes a more continuous shape connecting the two grabens with a much smaller ridge and almost East-West trending basin (less than 15º for Experiment 3). Fault displacement is then seen to be transferred from one fault to the other through a series of sub-parallel en echelon faults.

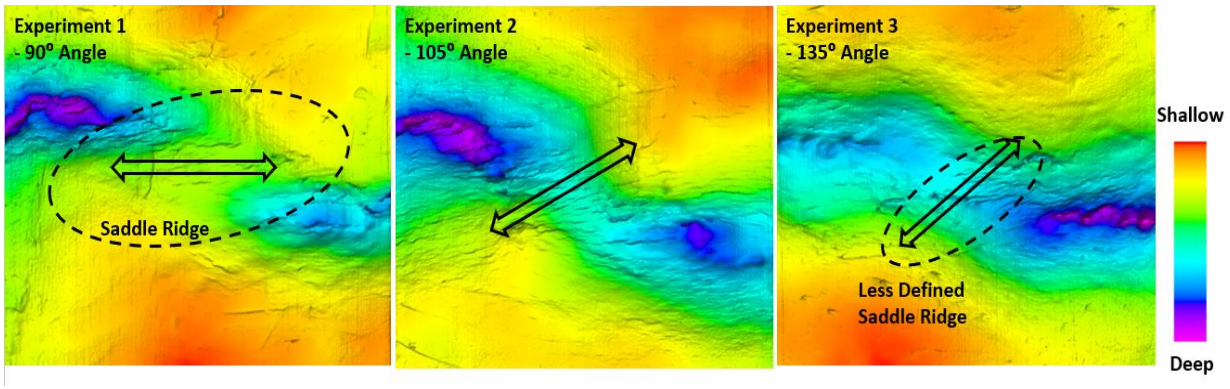


Figure 4.5. Final topographic map of each experiment (1, 2, 3) modeled and built in Petrel showing deeper parts of the basin in purple.

b) Brittle Models:

For Experiments 4, 5, and 6, brittle lithologies were simulated by using cement like material. Results from the three experiments show a very well defined major fault on top of the pre-existing cut at the plate edge. Most of the displacement is transferred through the transfer zone

using the major faults such that the width of the damage zone is relatively narrow. For all three experiments, faulting initiated right above the plate and extends to the cement surface. Those minor faults very soon connect with each other creating the major faults. The orientation of those faults is mainly east-west (perpendicular to the extension direction) and they tend to curve into the transfer zone as they approach it. Little to no folding of beds is seen with the brittle experiments such that most of the rotation is taken place within the relay ramps that connect the upthrown and the downthrown blocks.

By comparing the three experiments, the orientation of the faults and the development of secondary fault is seen to be controlled by the angle of discontinuity in the basement. At the 90º bend, the two faults remain E-W and curve towards each other at to the pre-existing cut location. Experiment 4 was continued beyond the amount of extension than that the other 2 experiments had undergone to investigate the ultimate geometry of the faults. Figure 4.6 shows the two faults curving into each other caused by the increase in extension.

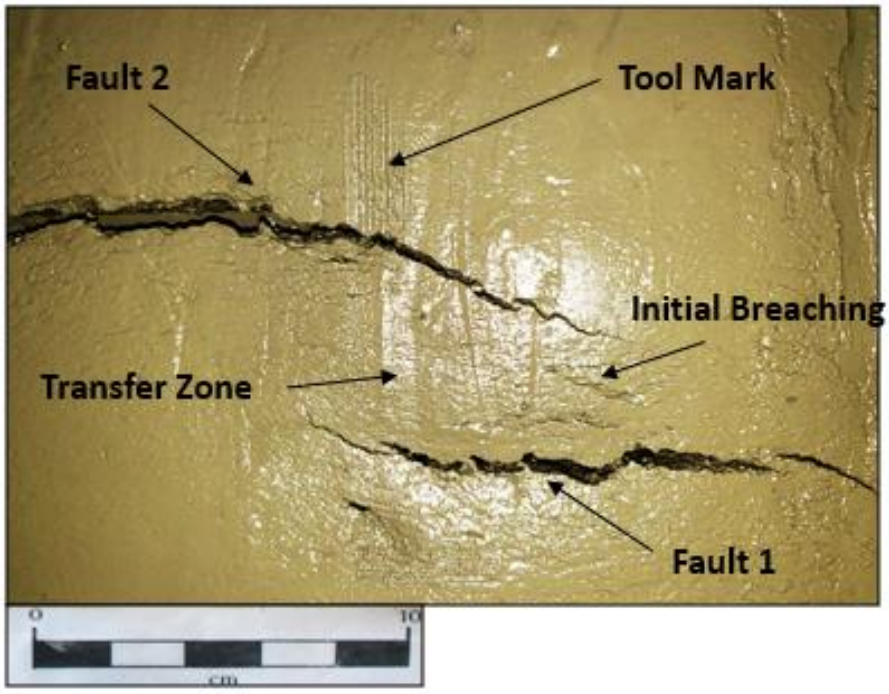


Figure 4.6. Transfer zone for Experiment 4 beyond the original extension desired showing the faults curving into each other

For Experiments 5 and 6, the transfer zone is characterized by the formation of secondary faults that cut through the transfer zone and deform it. The orientation at which those faults form as well as their density and length is associated with the angle of the bend at basement. At 105º, two major secondary faults develop at about 30º NW-SE due to the brittleness of the relay ramp and its inability to accommodate the additional extension. For Experiment 6, the transfer zone is characterized by multiple secondary faults predominately East-West trending along the angle of the bend. Similar to the ductile experiment (Experiment 3), the moving block of the cement cake tends to be better connected and act as a major fault line.

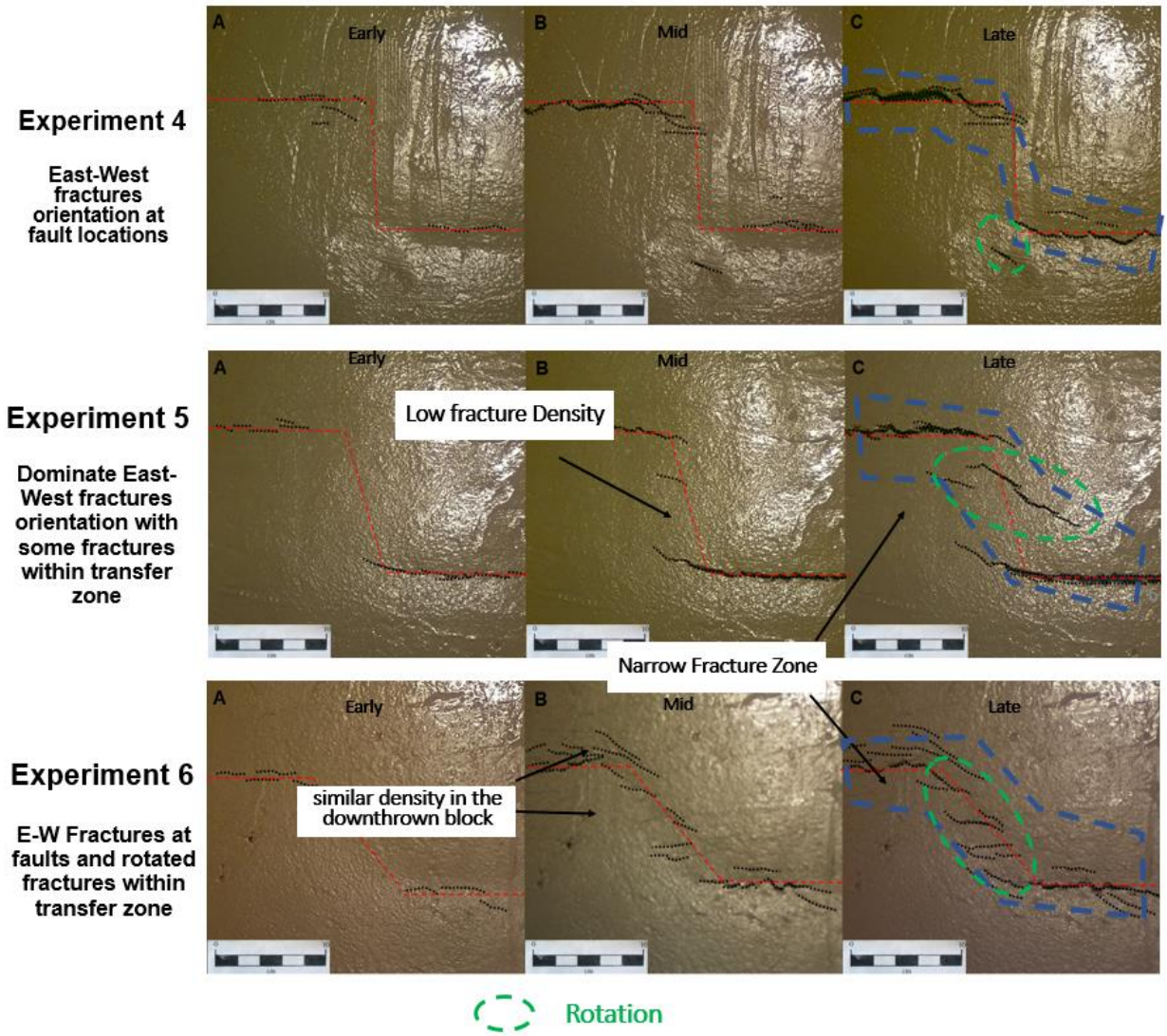


Figure 4.7. Detailed evolution of the structure at three stages (early, mid, and late, corresponding to beginning of faulting, midway, and final faulting stage) for Experiments 4, 5, and 6.

Similar to Experiments 1, 2, and 3, a detailed Petrel model was built to understand the geometry of the transfer zone. Figure 4.7 shows a final structure of the transfer zone for each of the experiments. Experiment 4 and 5 shows a very subtle change in the structure going from the upthrown to the downthrown block where the majority of the deformation is happening at the fault location and the relay ramps are slightly tilted to transfer the displacement from one block to the other. However, Experiment 6 shows a different geometry with a more continuous basin like

morphology along the transfer associated with an increase of faults density. The final shape of this experiment is similar to Experiment 3 where the geometry indicating a continuous distribution of displacement along the faults and within the transfer zone. Displacement is predominately at the major faults but is present at the secondary fault locations as well.

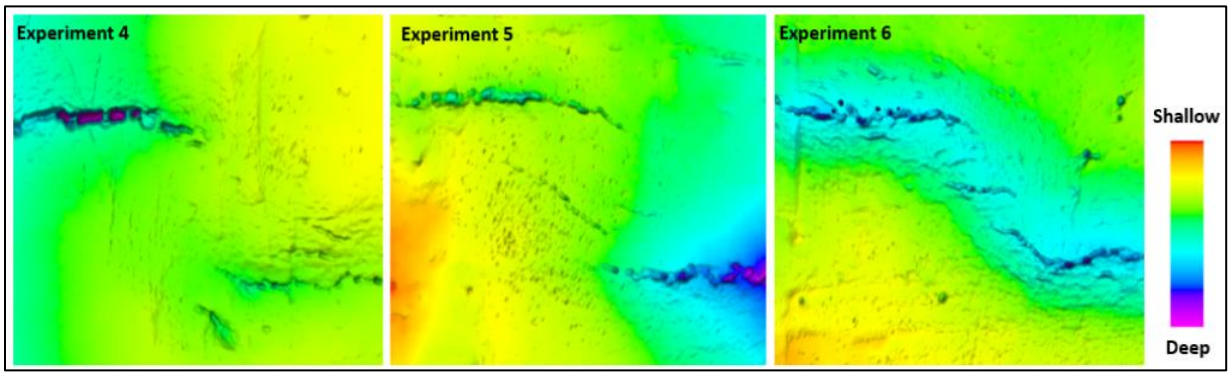


Figure 4.8. Final structure of each experiment (4, 5, and 6) modeled and built in Petrel showing deeper parts of the basin in purple.

c) Deformation Variations:

Studying the deformation distribution for each experiment helps understand the mechanism by which those transfer zones were created. 3D scanner data were taken at each stage to determine the shape of the relay ramps. Those readings were then georeferenced and converted to pointset coordinates that present the surface at a 0.015 inch point density. The surface at each stage is then subtracted from the previous created surface to determine the location and amount of displacement undertaken by the clay and cement models within each interval. Observations for the ductile and brittle models corresponding for the 90º angle (Experiment 1 and 4) can be seen in Figures 4.9 and 4.10 where hot colors represent high displacement.

By comparing the two experiments, the ductile experiment (clay) shows a much wider zone of deformation with a maximum deformation along the fault zone at stages 1 and 2. As deformation increases, the width of that zone is reduced remarkably such that most of the deformation is

localized to the major faults. This indicates that most of the folding and bed tilting happens early on in the evolution history of the transfer zones such that once major faults are defined, the majority of displacement takes place along those faults.

In contrast, for the brittle experiment (cement), the majority of the displacement occurs within a very narrow zone around that fault. This narrow bends get thicker with the increase in displacement to form a well-defined and connected fault plane. Hence, most of the displacement is happening along the major faults where surrounding beds remain relatively flat. Stage 1 shows a light tilting and folding of bends, indicating, similar to the ductile case, that the initial stage is characterized by folding. However, with brittle rock, the mechanism of faulting is caused by pre-existing faults as opposed to folding of the ductile beds.

Those results for the brittle experiments support the fault segmentation idea where the final shape of the fault will depend on the linkage of smaller faults (Peacock 2002). As Fossen et al. (2016) put it, the growth of faults is uneven and depends on the stress perturbation around the fault, caused by drop or increase of stress due to neighboring faults. As large-scale fault are forming, small embryonic segments are connecting to transfer and accommodate for the displacement. This understanding of fault linkage mechanism provides significant implications on fault interpretation, structural analysis, and fault growth history.

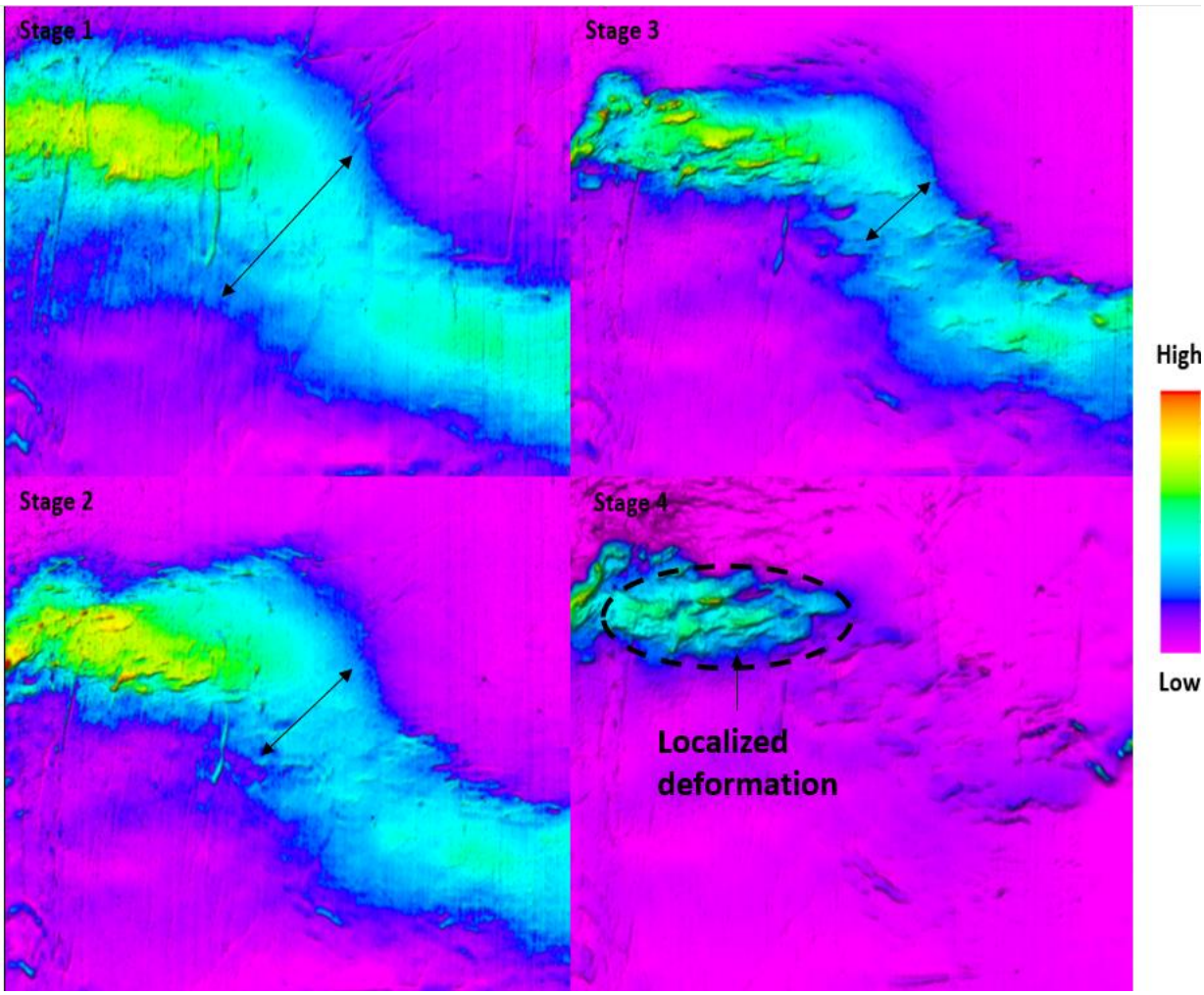


Figure 4.9. Displacement increase at each stage for Experiment 1 (stage 1 is at the beginning and stage 4 is at the end of the experiment).

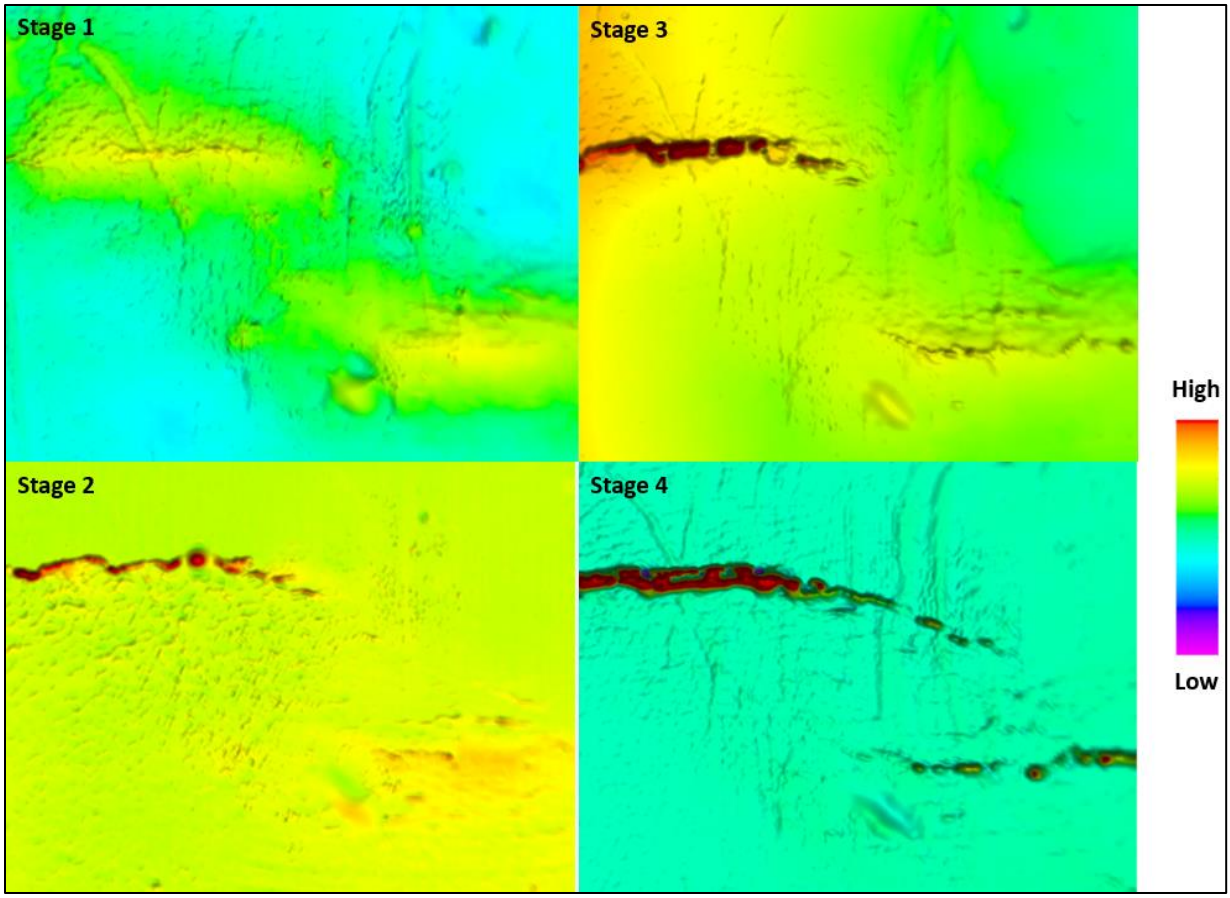


Figure 4.10. Displacement increase at each stage for Experiment 4 (stage 1 is at the beginning and stage 4 is at the end of the experiment).

4. NATURAL EXAMPLES

Surface natural examples can be used to study the transfer of displacement along faults using LiDAR data from the USGS. Two sites were chosen to be examined: Yucca Mountain just northeast of the Death Valley National Park in Nevada and the Uncompahgre uplift west of Grand Junction stretching between Colorado and Utah. The two sites are characterized by en-echelon faulting in volcanic (competent) and sandstone and salt (incompetent) rocks respectively.

The region of the Yucca Mountain, located in southern Nevada, is defined by partially detached Pre-Cenozoic basement deep-seated faults striking north-west within the southern part of the Walker Lane belt in Nevada (Schweickert and Lahren,1996). The overlaying Cenozoic

section is defined by volcanic deposits and deformed by normal faulting and rotational shear. Overall, the Yucca mountain area is defined by a graben, with the majority of antithetic faults to the east and a dipping range front fault on the west side (Fridrich, 1999). Stuckless and Levich (2007) defined the region by eight physiographic elements including Yucca Mountain and the Crater Flat. The flat is a small basin, 6 to 11km wide and 24km long, stretching north-south and bounded by the Yucca faults on the east and Bare mountain on the west (Struckless and Levish, 2007). Faults within the flat are defined by a pseudo radial complex to the north caused by the southward clockwise rotation with a small component of oblique offset with no major strike slip character (Fridrich, 1999). Analysis of fault deformation indicates origination of stress around 9 Ma defined by subsidence of the basin and on-going extension. The stratigraphic column within the crater flat is defined by thick volcanic tertiary rocks, mainly defined by well stratified rhyolites and quartz latites reaching up to 610m thick

The Uncompahgre uplift is a structural uplift that stretches between Colorado and Utah separating the Piceance and Paradox basins. The uplift is associated with the Ancestral Rockies orogeny defined by a Precambrian northwest oriented feature that impacted fault orientations at a later stage (White and Jacobson, 1983). Studies of White and Jacobson of different cross-sections along the uplift shows a set of subparallel reverse faults transferring the throw to one major fault toward the north. This theory was later revised by Kluth and Duchene (2009) proposing basement-involved thrust faults associated with salt movement and welding. Salt might have been displaced by a growing synorogenic wedge, creating salt walls and moving from the proximal to less proximal mini-basins. The rocks within the uplift post salt deposition consist of shales, carbonates, and other marine deposits (Elston and Shoemaker, 1960). Modeling of kinematic and dynamic deformation of the anticline shows a varying dipping of flanks between 0 and 12 degrees along the

central region in the south and decreasing to 0 to 3 degrees in the north. This modeling indicates rigid-body rotation of the blocks and shortening associated by the compression of the crust during the Laramide.

Hence those two areas present great analogs to study the impact of lithological mechanical properties on the deformation style within the transfer zones. Figures 4.11 and 4.12 show a comparison between the two studied sites showing elevation surfaces derived from LiDAR data. The Yucca faulting style is comparable to the observation made by Ferrill and Morris in South Texas for competent rock indicating minor changes in dip along the relay ramps and minor normal faults cutting through it and connecting the two major faults. This is characterized by a low displacement gradient and defined major faults take on most of the displacement as seen in the experimental models. However, by examining the Uncompahgre uplift, the faulting style within the transfer zone varies where beds are further rotated and more steeply dipping. The displacement from one fault to the other is transferred to a set of smaller en-echlon faults that cut through the relay ramp and results in fractured rocks. As seen in the experiments, the softer the lithology, such as salt and sedimentary rocks (shale and sandstone), the higher the number of faults that are created within the transfer zone to accommodate for the increase in displacement.

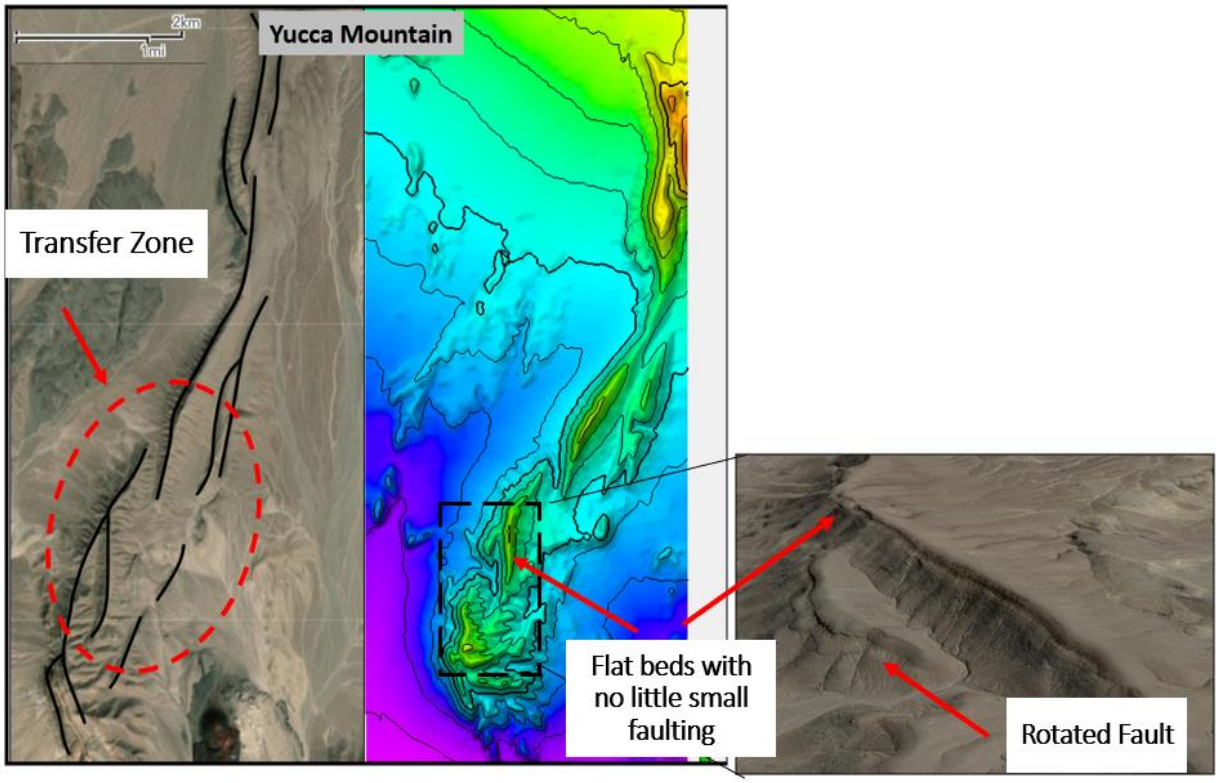


Figure 4.11. Structural map at the Yucca Mountain (brittle rock) showing transfer zones and faulting style using LiDAR data.

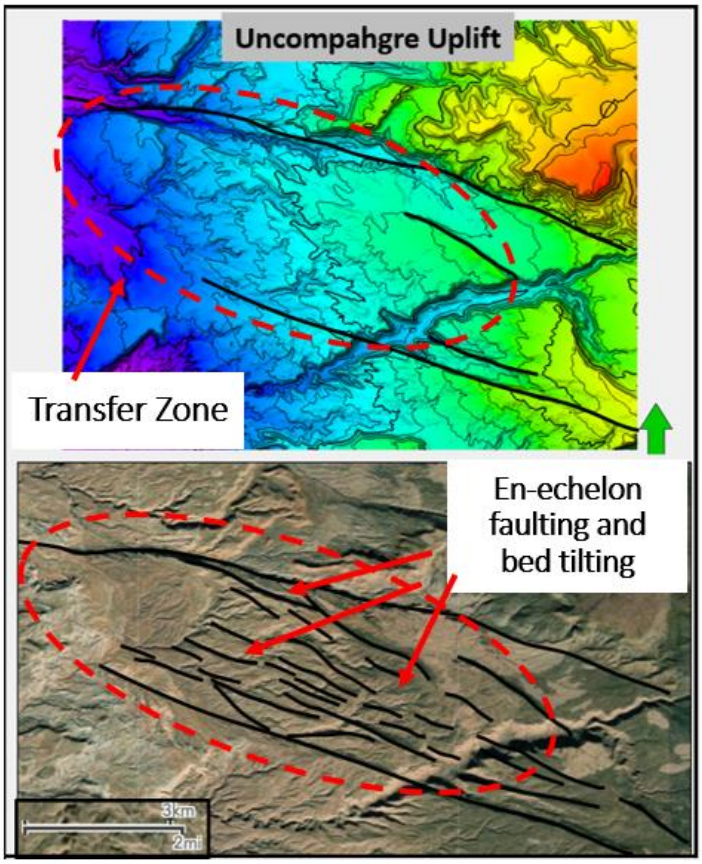


Figure 4.12. Structural map at the Uncompahgre uplift (ductile rock) showing transfer zones and faulting style using LiDAR data.

5. SEISMIC EXAMPLE

Seismic data can be used to illustrate similar observations. Figure 4.13 shows the seismic dip attribute extracted along an interpreted horizon for the Parihaka fault within the Taranaki Basin. That Parihaka fault is located within the northern part of the Taranaki Basin and characterized a set of three en-echelon northeast-southwest dipping faults. The displacement along the fault, can reach up to 1.8 km of vertical displacement during the Plio-Pleistocene time (Giba, 2012).

The stratigraphic column within the Taranaki Basin is defined by Late Cretaceous terrestrial and transgressive marine sediments which extended into the Paleocene and Eocene

periods, followed by carbonate deposition of the Ngatoro group during the Oligocene. During the Noegene period, the sedimentary record indicates the deposition of the Waitti Group and the overlaying Rotokare Group which are characterized by marine and terrigenous deposits due to the regression of the shelf (Thrasher, 1992). The horizon shown in Figure 4.12 represents one of the strongest reflector seen within the Rotokare Group that has been faulted by the Parihaka fault.

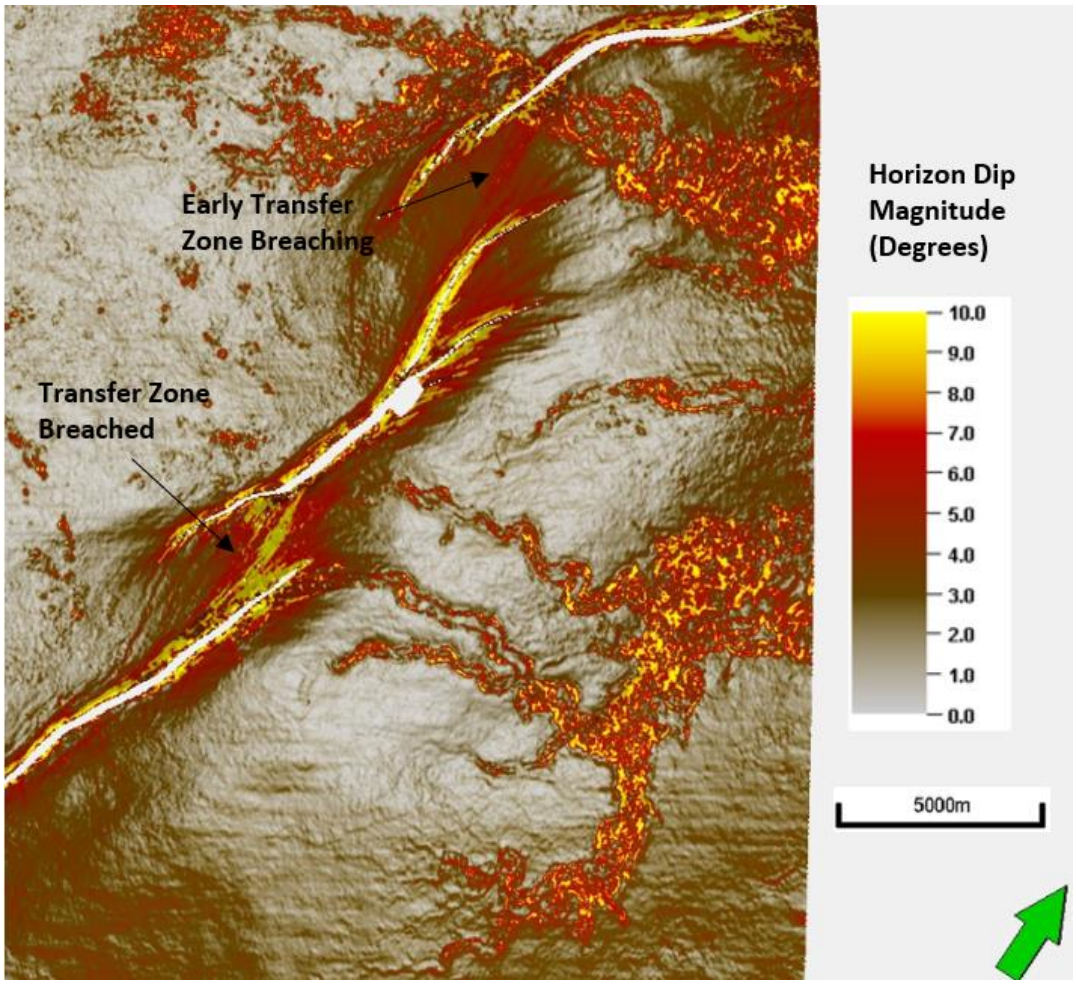


Figure 4.13. Dip attributes extracted along an interpreted horizon of the Parihaka fault offshore New Zealand.

As seen on the seismic attributes map, the transfer zones between the three main faults is characterized by the existence of smaller scale faulting. As faults approach each other, displacement is seen to be distributed within the relay ramp by splay features of the faults. Relay

ramps are seen to be defined by rotated beds, highly fractures zones, and breached faults that connect the major two faults. As seen in the lithological description of the wells penetrating this area, the sedimentary record is defined by the alternating of shales, sands, and carbonate sediments that behave more like an incompetent rock. Hence, the faulting style associated matches the clay experiments that were defined by a distribution of displacement over a large population of faults defined by rotated beds. Figure 4.14 is a dip magnitude map generated for all six (6) experiments using the topographic data collected using the laser scanner. The figure shows a variation of dip at fault and fracture locations. For the cement experiments, little rotation is seen, as excepted for brittle rocks, thus showing only localized dip magnitude change. However, for the clay experiments, the dip magnitude shows a wide range of fractures distribution corresponding to the tilting and fracturing of the beds. Similar to seismic dip magnitude for the Parihaka fault in figure 4.13, the dip magnitude indicates the location of the fault, shows clearly the distribution of fractures and splays, and defining breaching geometries. Hence, the comparison between the two figures indicate that the Waiti Group in the Taranaki Basin deformed as a ductile layer characterized by tilting of beds specially within transfer zones, and a distribution of fracturing mainly around faults.

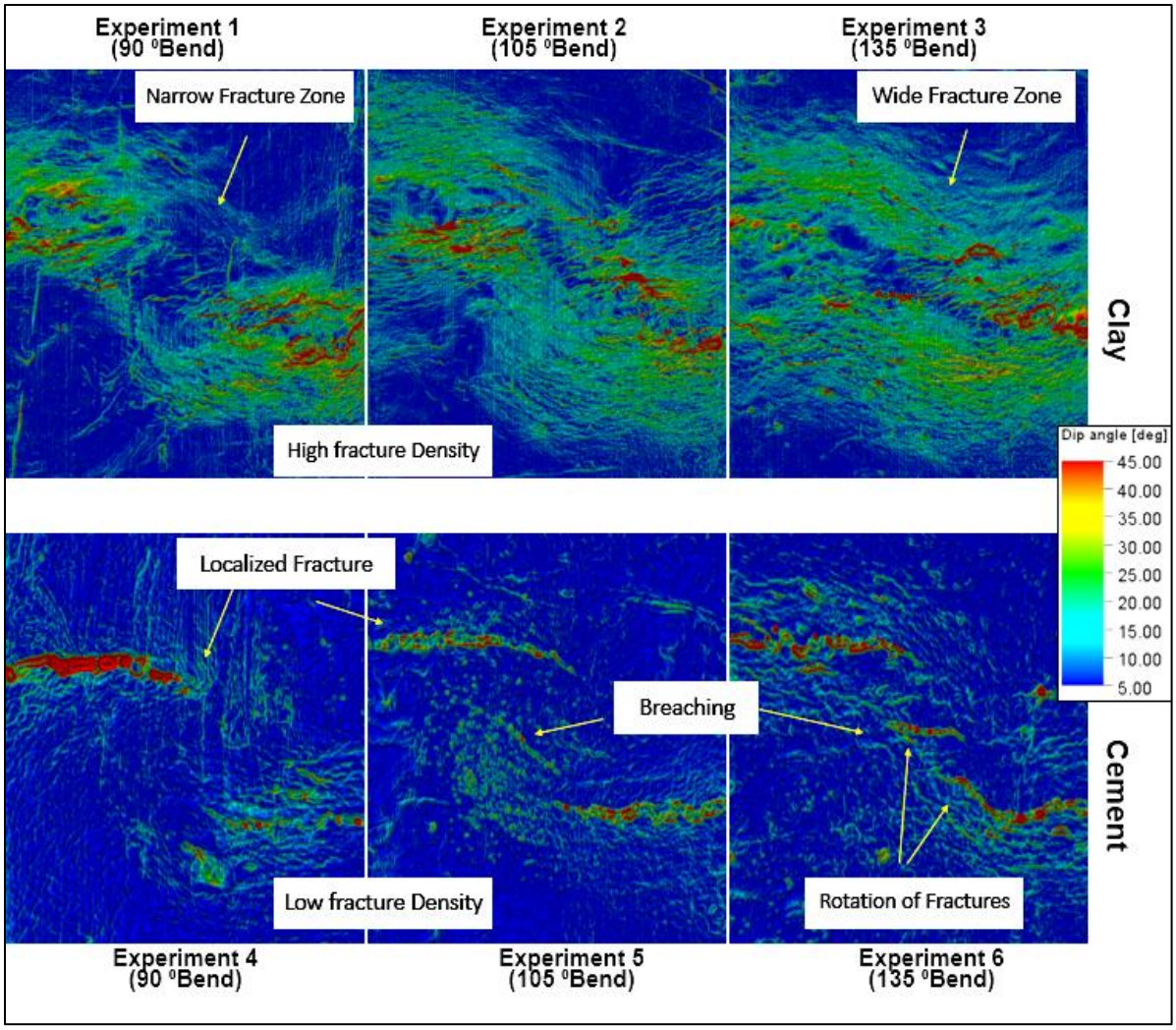


Figure 4.14. Dip magnitude calculated for experimental models using topographic data collected during laser scanning at the end of each experiment.

6. RESERVOIR POTENTIAL

As seen in the outcrop description, ductile experiments are an analog for ductile formations such as shales while as the brittle experiments are analog for a harder rock such as carbonates. However, it is very rare to have one type of rock dominating the deformation pattern. In most cases, a mix of both or other lithologies are common such that the actual deformation style is in between the deformation styles observed in those experiments.

=

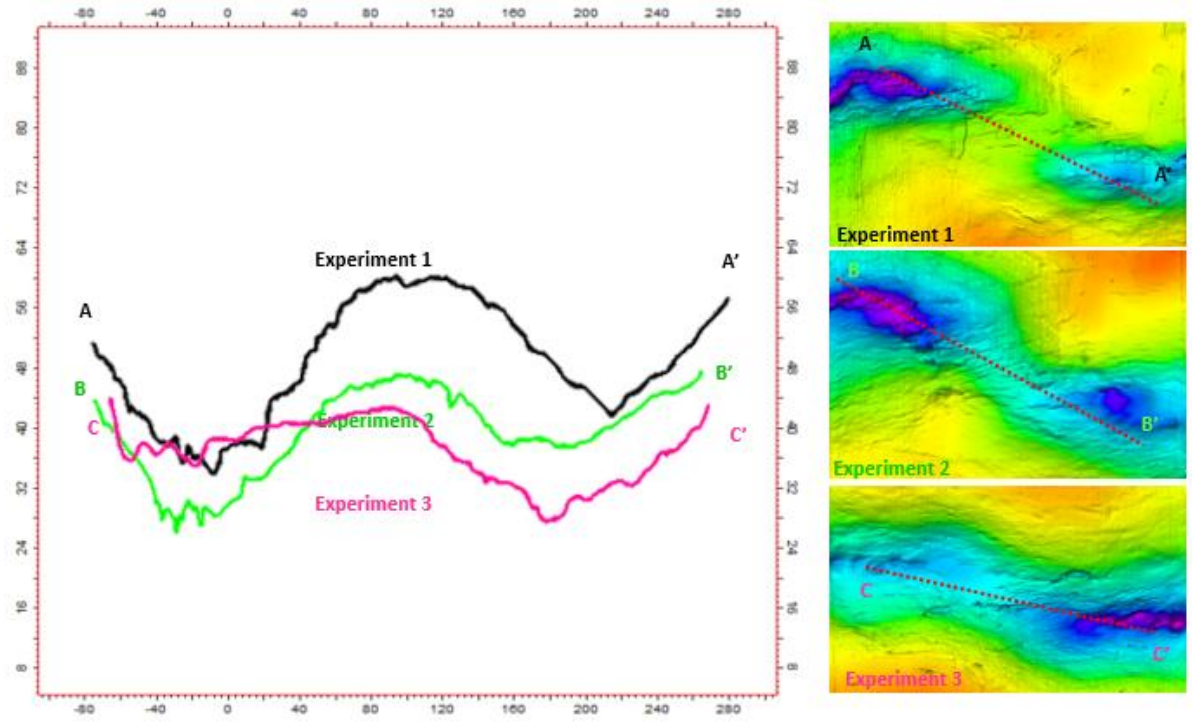


Figure 4.15. Surface profile for Experiments 1, 2, and 3 along the relay ramps at section AA', BB', and CC'.

While analyzing the experiment models, the ductile experiments led to the development of a pull-apart basin within the transfer zone that is characterized by an anticline with a two or four-way closure. In contrast, the transfer zone geometries observed with the brittle experiments, are defined with tilted relay ramp that are gently dipping and occasionally cut by faults. The formation of compartment or a sealing reservoir within those zones is only possible sealing faults that cut through the ramp and provide a trap for hydrocarbon accumulation.

In addition, the variation in pre-existing basement faults, control the geometry and volume associated with those traps. For instance, the anticline created during Experiment 1 is much larger than the other two anticlines developed in Experiments 2 and 3. This is caused by the connectivity of faults such that steep folds were created to accommodate for the displacement along those faults.

Figure 4.15 shows a comparison of the profile of the clay surface for all three cases as analog for potential hydrocarbon traps. Hence, Experiment 1 shows the highest potential for reservoir storage.

However, when assessing any petroleum system, the sealing potential of the reservoir plays a role in determining the success of any exploration activity. Ductile experiments were characterized by many multiple small faults that many had little displacement. Figure 4.16 is a 3D view of the anticline across the transfer zone derived from Experiment 1. The picture is representation of the shape of the top of the clay layer where warm colors represent deeper surface. As clearly seen in the picture, the ridge separating the two grabens within the transfer zone is cut by faults running east-west and causing significant displacement at the top of the anticline. Assuming that similar situation is for a reservoir formation, the anticline then has a high risk of being depleted and hydrocarbons to have seeped through the faults at the crest. However, and assuming that the ductile layer is a shale, this anticline would still have a certain risk, possibly lower, associated with the amount of displacement at those faults that can juxtapose reservoir to reservoir beds and thus causing hydrocarbon migration or seepage.

For the same experiment conducted with the brittle analog, Experiment 4, the transfer zone geometry is gently dipping, connecting both faults with no major folding or bed tilting. As mentioned, the sealing mechanism of those reservoirs is driven by the existence of a fault cutting through the ramp. However, the ramp itself can be a fairly good reservoir if the surrounding rocks have sealing capabilities. Hence, the risk associated with this type of trap is related to the degree of deformation that the relay ramp has gone through and the overlaying sediments permeabilities. Similarly, relay ramps can play great migration pathways for hydrocarbon migration particularly along well-defined faults from the downthrown to the upthrown block.

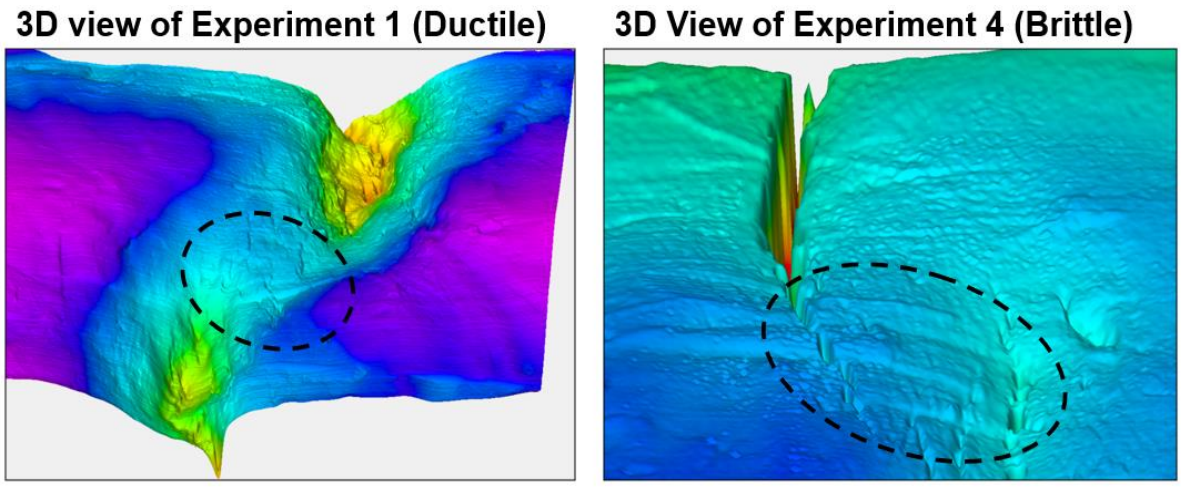


Figure 4.16. 3D view of the transform zone for Experiments 1 and 4 showing the structure and distribution of faults/fractures at the end of the experiment (late stage).

7. CONCLUSION

This chapter presents experimental modeling work done to understand transfer zone geometry and development using variable basement pre-existing fault geometries. Three basement fault orientations are used to define approaching convergent faults at 90º, 105º, and 135º. The variation of bend angel impacted the distribution of fractures and faults within the experiments. As a general observation, the shallower the angle that connects the two faults, the higher the tendency for both faults to connect early and behave as a continuous fault system. At the 90º bend angle, faults remained mostly independently taking the displacement within their zone of impact.

In addition, clay and cement materials were used to simulate ductile and brittle rocks, respectively, and study the impact of lithological properties on the growth mechanism of faults and relay ramps. Results for the ductile experiment showed a gentle large deformation zone characterized by folding and abundant distribution of small faults. The orientation of those zones varied according to their location relative to the transfer zone. By examining the displacement associated with each stage of the experiment, deformation starts over a wide area and narrows as

the displacement localizes close the deepest part of the formed graben. Compared to the brittle experiments, deformation is not driven by major folding but by pre-existing faults that form above the plate edges and connect to fault a continuous well-defined fault plane. Those experiments showed very little tilting or rotation of beds outside the relay ramp that showed gradual change from the upthrown to the downthrown blocks. As deformation increases, additional faults developed within the relay ramp, thus "breaching" it and causing internal faulting and tilting for the ramp. The distribution of deformation is consistently a maximum at fault locations and shows no major folding except for Experiment 6. This is caused by the geometry of the pre-existing fault geometry in the basement.

As seen in outcrops and in experimental models, the fracture density and bed tilting associated with the ductile layer is significant which poses a great risk for seal capacity within transfer zones. Observations from outcrops in the Edwards Limestone show similar characteristics to the experiment with a well-defined fault plane with no major tilting of beds. The impact of relay ramps on hydrocarbon exploration is significant as they can form anticline and ridges to trap oil migration. In addition, they can be great migration pathways or causes reservoir to leak hydrocarbons. This has been seen to mainly the case of transfer zones using the fault sealing analysis in the Parihaka seismic inversion model. As the definition implies, transfer zone are connectors of upthrown and downthrown blocks that transfer displacement from one fault to another, thus providing a pathway for fluid migration. As they tend to get more fractured and broken with the increase of displacement, and due to the lithological composition of those ramps, they provide additional enhanced permeability within them to assist vertical and horizontal migration.

CHAPTER 5: CONCLUSIONS

The work presented in this dissertation presents a comprehensive analysis of transfer zone properties and formation. It provides additional insights on transfer zone growth mechanisms for the Parihaka fault system in the Taranaki Basin through the use of seismic data and experimental models. The use of seismic attributes along with picked horizons provide a means of defining the deformation history of the transfer zone and the mechanism by which they developed. Curvature, seismic dip, and variance are all tools that helped determine the degree of rotation that the ramps have experienced along with the associated fracturing and faulting. Correlating those attributes to structural parameters such as structural dip, total displacement, and structural folding allowed for a better and more defined understanding of the structural complexity.

In addition, this dissertation is one of the few studies using seismic inversion to determine fault sealing and leaking potential. The workflow presented here used facies derived from seismic inversion properties to identify sealed reservoirs within the Taranaki Basin. My analysis shows that transfer zones can be major migration pathways using both the juxtaposition and SGR methods, where due to their gentle dipping beds, and tilted geometry, they reduce the capacity of faults to seal at their edges. Hence, significant deformation is needed to exceed the rotation of the relay ramp or alternatively to displace permeable layers along faults that breach the ramp, in order to achieve full sealing. SGR methods show different results based on the presence of tight shaley beds relative to highly permeable reservoir beds. I find that despite the existence of relay ramps, some transfer zones can act as migration barriers or structural traps.

The impact of pre-existing faults, as well as the mechanical stratigraphy impact the mechanism by which relay ramps form. I demonstrated this effect using experimental models that used variable pre-existing fault geometry and different types of material to model ductile and brittle

deformation. The study found that the shape of pre-existing faults impacts the location at which the faulting and fracturing within the transfer zone occur, leading to a wider deformation zone for non-overlapping and gently connected sub-extension faults. As the fault connecting the two pre-existing fault gets shorter, or the connection is abrupt, the deformation zone tends to be more contained along the fault zones. In addition, using brittle and ductile materials has shown a significant impact of lithology on the shape and mode of deformation of faulting. Brittle material leads to less tilting in beds, more significant displacement along faults, and a relatively lower amount of fracturing on either side of the transfer zone, where fault propagation is seen to drive growth of the zone. For ductile material, the beds are seen to be more folded with abundant presence of small faults that connect the two major faults. The growth mechanism seen herein is similar to what was described by Peacock and Sanderson (1990 and 1994) model on stages of relay ramp growth, such that fault splay and development of the smaller faults precedes the breaking of the transfer zone and thus the formation of a major fault that connects both of the initial major faults.

Despite having the Parihaka fault system as the main study area, the models and workflow presented in this dissertation allows for application to other areas and basins. It presents techniques and considerations that contribute to an increased understanding of transfer zone growth as well as to best methods to approach some of the related questions. Although some of the methods must be thoroughly and carefully carried in other areas, they are the most inclusive and complete work on transfer zones for extensional faults. Recommendation for future work is to expand the application of the workflows and methods developed in this research to other compressional and strike-slip areas.

REFERENCES

Allan, U. S., 1989, Model for hydrocarbon migration and entrapment within faulted structures: AAPG Bulletin, V. 73, no. 7, pp 803-811

Bahorich, M., and S. Farmer, 1995, 3-D seismic discontinuity for faults and stratigraphic features: The coherence cube: The Leading Edge, v. 14, no. 10, p. 1053–1058, doi:10.1190/1.1437077.

Basile, C., and J. P. Brun, 1999, Transtensional faulting patterns ranging from pull-apart basins to transform continental margins : an experimental investigation: v. 21.

Bellahsen, N., S. Leroy, J. Autin, P. Razin, E. Acremont, H. Sloan, R. Pik, A. Ahmed, and K. Khanbari, 2013, Tectonophysics Pre-existing oblique transfer zones and transfer / transform relationships in continental margins : New insights from the southeastern Gulf of Aden , Socotra Island , Yemen: Tectonophysics, v. 607, p. 32–50, doi:10.1016/j.tecto.2013.07.036.

Bense, V F, E H Van den Berg, and R T Van Balen. 2003. “Deformation Mechanisms and Hydraulic Properties of Fault Zones in Unconsolidated Sediments; the Roer Valley Rift System, The Netherlands.” *Hydrogeology Journal*.

Bose, S., and S. Mitra, 2010, Analog modeling of divergent and convergent transfer transfer zones in listric normal fault systems: AAPG Bulletin, V. 94, no. 9, pp 1425-1452, doi:10.1306/01051009164.

Bowers, G., 1995, Pore pressure estimation from velocity data: Accounting for overpressure mechanisms besides undercompaction: SPE Drilling and Completion, June 1995, pp 89-95

Caine, Jonathan Saul, J. P. Evans, and C. B. Forster. 1996. “Fault Zone Architecture and Permeability Structure.” *Geology*.

Chopra, S., and K. J. Marfurt, 2015, Is curvature overrated? No, it depends on the geology: First Break, v. 33, no. 2056, p. 45–55, doi:10.3997/1365-2397.2014021.

Clarke, Stuart M., S. D. Burley, and G. D. Williams. 2005. “A Three-Dimensional Approach to Fault Seal Analysis: Fault-Block Juxtaposition & Argillaceous Smear Modelling.” *Basin Research*.

Conneally, J., C. Childs, and J. J. Walsh, 2014, Contrasting origins of breached relay zone geometries: Journal of Structural Geology, v. 58, p. 59–68, doi:10.1016/J.JSG.2013.10.010.

Dooley, T. P., and G. Schreurs, 2012, Tectonophysics Analogue modelling of intraplate strike-slip tectonics : A review and new experimental results: Tectonophysics, v. 574–575, p. 1–71, doi:10.1016/j.tecto.2012.05.030.

Eaton, Ben A. 1975. “The Equation for Geopressure Prediction from Well Logs.” In *Fall Meeting of the Society of Petroleum Engineers of AIME*.

Egholm, D. L., O. R. Clausen, M. Sandiford, M. B. Kristensen, and J. A. Korstgård. 2008. “The Mechanics of Clay Smearing along Faults.” *Geology*.

Elstone D. P., E. M. Shomaker, 1960, Late Paleozoic and Early Mesozoic Structural History of the Uncompahgre Front, Geology of the Paradox Basin fold and Fault Belt, Third Field Conference.

Ferrill, D. A., and A. P. Morris, 2001, Displacement gradient and deformation in normal fault systems: v. 23, p. 61–638.

Ferrill, D. A., and A. P. Morris, 2008, Fault zone deformation controlled by carbonate mechanical stratigraphy, Balcones fault system , Texas: v. 3, p. 359–380, doi:10.1306/10290707066.

Fulljames, J.R., L.J.J Zijerveld, and R.C.M.W. Franssen, 1997. Fault seal processes: Systematic analysis of fault seals over geological and production time scales. In: P. M0ller-Pedersen and A.G. Koestler (Editors), Hydrocarbon Seals: Importance for Exploration and Production. Norwegian Petroleum Society (NPF), Special Publication 7. Elsevier, Amsterdam, pp. 51-59.

Fossen, H., and A. Rotevatn, 2016, Fault linkage and relay structures in extensional settings—A review: Earth-Science Reviews, v. 154, p. 14–28, doi:10.1016/J.EARSCIREV.2015.11.014.

Fridrich, C.J., 1999, Tectonic evolution of the Crater Flat basin, Yucca Mountain region, Nevada: in Cenozoic Basins of the Death Valley Region, Wright, L.A. and Troxel, B.W., eds., Geological Society of America Special Paper 333, p. 169 - 195.

Gersztenkorn, A., and K. J. Marfurt, 1999, Eigenstructure-based coherence computations as an aid to 3-D structural and stratigraphic mapping: GEOPHYSICS, v. 64, no. 5, p. 1468–1479, doi:10.1190/1.1444651.

Giba, M., A. Nicol, and J. J. Walsh, 2010, Evolution of faulting and volcanism in a back-arc basin and its implications for subduction processes: Tectonics, v. 29, no. 4, doi:10.1029/2009TC002634.

Giba, M., J. J. Walsh, and A. Nicol, 2012, Segmentation and growth of an obliquely reactivated normal fault: Journal of Structural Geology, v. 39, p. 253–267, doi:10.1016/J.JSG.2012.01.004.

Gibson, R.G., 1994. Fault-zone seals in siliciclastic strata of the Columbus Basin, offshore Trinidad. Am. Assoc. Pet. Geol. Bull. 78 (9), 1372–1385.

Haque, A. E., M. A. Islam, and M. R. Shalaby, 2016, Structural Modeling of the Maui Gas Field, Taranaki Basin, New Zealand: Petroleum Exploration and Development, v. 43, no. 6, p. 965–975, doi:10.1016/S1876-3804(16)30114-8.

Hus, R., V. Acocella, R. Funiciello, and M. De Batist, 2005, Sandbox models of relay ramp structure and evolution: v. 27, p. 459–473, doi:10.1016/j.jsg.2004.09.004.

Iacopini, D., R. W. H. Butler, S. Purves, N. Mcardle, and N. De Freslon, 2016, Exploring the seismic expression of fault zones in 3D seismic volumes: Journal of Structural Geology, v. 89, p. 54–73, doi:10.1016/j.jsg.2016.05.005.

Infante-Paez, L., and K. Marfurt, 2018, In-context interpretation: Avoiding pitfalls in misidentification of igneous bodies in seismic data: Interpretation, V. 6, No. 4, pp. SL29-SL42doi:10.1190/INT-2018-0076.1.

Ingram, G. M., , J. L. Urai,, and M. A. Naylor, 1997, Sealing processes and top sealing assessment: NPF Special Publication, v.7, pp. 165-174

King, P. R., and G. P. Thrasher, 1996, Cretaceous-Cenozoic geology and petroleum systems of the Taranaki Basin, New Zealand: Lower Hutt, N.Z. :, Institute of Geological & Nuclear Sciences, 244 p.

King, P. R., 2000, Tectonic reconstructions of New Zealand: 40 Ma to the Present: New Zealand Journal of Geology and Geophysics, v. 43, no. 4, p. 611–638, doi:10.1080/00288306.2000.9514913.

Kluth, C. F., and H. R. Duchene, 2009, Late Pennsylvanian and Early Permian Structural Geology and Tectonic History of the Paradox Basin and the Uncompahgre Uplift, Colorado and Utah, RMAG 2009 Special Publication, Rocky Mountain Association of Geologists.

Knipe, R.J., 1992a. "Faulting processes, seal evolution, and reservoir discontinuities: an integrated analysis of the ULA Field, Central Graben, North Sea." *Abstracts of the Petroleum Group Meeting on Collaborative Research Programme in Petroleum Geoscience Between UK Higher Education Institutes and the Petroleum Industry. Geological Society, London*

Knipe, R. J., 1997, Juxtaposition and Seal Diagrams to Help Analyze Fault Seals in Hydrocarbon Reservoirs 1: v. 2, no. 2, p. 187–195.

Knipe, R. J. 1997. "Juxtaposition and Seal Diagrams to Help Analyze Fault Seals in Hydrocarbon Reservoirs." *AAPG Bulletin.*

Larsen, P.-H., 1988, Relay structures in a Lower Permian basement-involved extension system, East Greenland: Journal of Structural Geology, v. 10, no. 1, p. 3–8, doi:10.1016/0191-8141(88)90122-8.

Lindsay, N.G., F.C. Murphy, J.J. Walsh, and J. Watterson, 1993. "Outcrop studies of shale smears on fault surface. The Geological Modelling of Hydrocarbon Reservoirs and Outcrop Analogues." *Blackwell Publishing Ltd.*

Lohr, T., C. M. Krawczyk, O. Oncken, and D. C. Tanner, 2008, Evolution of a fault surface from 3D attribute analysis and displacement measurements: Journal of Structural Geology, v. 30, no. 6, p. 690–700, doi:10.1016/J.JSG.2008.02.009.

Mcclay, K. R., and F. Dynamics, 2002, 4-D Evolution of rift systems: Insights from scaled physical models: V. 6, no. 6, p. 935–959.

Marfurt, K. J., 2010, The Shape of Seismic Interpretation, *in* Seismic Imaging of Depositional and Geomorphic Systems: 30th Annual: Society of Economic Paleontologists and Mineralogists, p. 241–294, doi:10.5724/gcs.10.30.0241.

Marfurt, K. J., 2015, Techniques and best practices in multiattribute display: Interpretation, v. 3, no. 1, p. B1–B23, doi:10.1190/INT-2014-0133.1.

Marfurt, K. J., 2006, Robust estimates of 3D reflector dip and azimuth: GEOPHYSICS, v. 71, no. 4, p. P29–P40, doi:10.1190/1.2213049.

Mitra, S., and D. Paul, 2011, Structural geometry and evolution of releasing and restraining bends : Insights from laser-scanned experimental models: v. 7, no. 7, p. 1147–1180, doi:10.1306/09271010060.

Morley, C. K., C. Haranya, W. Phoosongsee, S. Pongwapee, A. Kornsawan, and N. Wonganan, 2004, Activation of rift oblique and rift parallel pre-existing fabrics during extension and their effect on deformation style: examples from the rifts of Thailand: Journal of Structural Geology, v. 26, no. 10, p. 1803–1829, doi:10.1016/J.JSG.2004.02.014.

Morley, C. K., R. A. Nelson, T. L. Patton, and S. G. Munn, 1990, Transfer zones in the East African Rift system and their relevance to hydrocarbon exploration in rifts: AAPG Bulletin, v. 74, no. 8, p. 1234–1253.

Nakayama, K., and D. Sato., 2002. “Prediction of Sealing Capacity by the Equivalent Grain Size Method.” *Norwegian Petroleum Society Special Publications*.

Naylor, M.A., G. Mandl, and C.H.K. Sijpesteijn, 1986. Fault geometries in basement-induced wrench faulting under different initial stress states. Journal of Structural Geology, V. 8, pp. 737-752.

Nicol, A., C. Mazengarb, F. Chanier, G. Rait, C. Uruski, and L. Wallace, 2007, Tectonic evolution of the active Hikurangi subduction margin, New Zealand, since the Oligocene: Tectonics, v. 26, no. 4, doi:10.1029/2006TC002090.

Paul, D., and S. Mitra, 2015, Fault patterns associated with extensional fault-propagation folding: Marine and Petroleum Geology, v. 67, p. 120–143, doi:10.1016/j.marpetgeo.2015.04.020.

Paul, D., and S. Mitra, 2013, Experimental models of transfer zones in rift systems: v. 5, no. 5, p. 759–780, doi:10.1306/10161212105.

Peacock, D. C. P., 2002, Propagation, interaction and linkage in normal fault systems: Earth-Science Reviews, v. 58, no. 1–2, p. 121–142, doi:10.1016/S0012-8252(01)00085-X.

Peacock, D. C. P., and D. J. Sanderson, 1991, Displacements, segment linkage and relay ramps in normal fault zones: Journal of Structural Geology, v. 13, no. 6, p. 721–733, doi:10.1016/0191-8141(91)90033-F.

Peacock, D. C. P., and D. J. Sanderson, 1993, Estimating strain from fault slip using a line sample: Journal of Structural Geology, v. 15, no. 12, p. 1513–1516, doi:10.1016/0191-8141(93)90011-X.

Peacock, D. C. P., and D. J. Sanderson, 1994, Geometry and Development of Relay Ramps in Normal Fault Systems 1: v. 2, no. 2, p. 147–165.

Peacock, D. C. P., and D. J. Sanderson, 1995, Strike-slip relay ramps: Journal of Structural Geology, v. 17, no. 10, p. 1351–1360, doi:10.1016/0191-8141(95)97303-W.

Pei, Y., D. A. Paton, R. J. Knipe, and K. Wu. 2015. “A Review of Fault Sealing Behaviour and Its Evaluation in Siliciclastic Rocks.” *Earth-Science Reviews*.

Rajabi, M., M. Ziegler, M. Tingay, O. Heidbach, and S. Reynolds, 2016, Contemporary tectonic stress pattern of the Taranaki Basin, New Zealand: Journal of Geophysical Research: Solid Earth, v. 121, no. 8, p. 6053–6070, doi:10.1002/2016JB013178.

Reilly, C., A. Nicol, J. J. Walsh, and H. Seebeck, 2015, Evolution of faulting and plate boundary deformation in the Southern Taranaki Basin, New Zealand: Tectonophysics, v. 651–652, p. 1–18, doi:10.1016/J.TECTO.2015.02.009.

Roberts, A., 2001, Curvature attributes and their application to 3D interpreted horizons: First Break, v. 19, no. 2, p. 85–100, doi:10.1046/j.0263-5046.2001.00142.x.

Rotevatn, A., C. A.-L. Jackson, A. B. M. Tvedt, R. E. Bell, and I. Blækkan, 2018, How do normal faults grow? Journal of Structural Geology, doi:10.1016/J.JSG.2018.08.005.

Sagy, A., and Y. Hamiel, 2017, Three - dimensional structure and evolution of an asymmetric pull - apart basin: International Journal of Earth Sciences, v. 106, no. 5, p. 1619–1630, doi:10.1007/s00531-016-1374-4.

Sayers, C. M., G. M. Johnson, and G. Denyer. 2002. “Predrill Pore-Pressure Prediction Using Seismic Data.” *Geophysics*.

Sayers, C M., M J. Woodward, and R. C. Bartman. 2002. “Seismic Pore-Pressure Prediction Using Reflection Tomography and 4-C Seismic Data.” *The Leading Edge*.

Schweickert, R. A., and M. M. Lahren, Erratum to “Strike-slip fault system in Amargosa Valley and Yucca Mountain, Nevada”, Tectonophysics, Volume 277, Issue 4, 30 August 1997, Pages 345-346

Stern, T. A., and W. E. Holt, 1994, Platform subsidence behind an active subduction zone: Nature, v. 368, no. 6468, p. 233–236, doi:10.1038/368233a0.

Stuckless, J. S., and R. A. Levich, 2007, The geology and climatology of Yucca Mountain and vicinity, Southern Nevada and California (Vol. 199). Geological Society of America.

Sylvester, A.G., 1988, Strike-slip faults. Geological Society of America Bulletin 84, 1293–1309.

Thorsen, C. E., 1963, Age of growth faulting in southeast Louisiana: GCAGS Transactions, Vo.13, pp 103-110.

Thrasher, G. P., 1992, Late Cretaceous Geology of the Taranaki Basin, New Zealand, Victoria University of Wellington.

Tobias, C. 2015. "Fault seal analysis: Constraining fault seal risk using seismic velocities." *AAPG/SEG International Conference& Exhibition. Melbourne.*

Tripathi, A. R. P., and P. J. J. Kamp, 2008, Timing of initiation of reverse displacement on the Taranaki Fault, northern Taranaki Basin: Constraints from the on land record (Oligocene Te Kuiti Group): p. 1–17.

Walsh, J. J., and J. Watterson, 1988, Analysis of the relationship between displacements and dimensions of faults: Journal of Structural Geology, v. 10, no. 3, p. 239–247, doi:10.1016/0191-8141(88)90057-0.

Watts, N. L. 1987. "Theoretical Aspects of Cap-Rock and Fault Seals for Single- and Two-Phase Hydrocarbon Columns." *Marine and Petroleum Geology*.

White, M. A., and M. I. Jacobson, 1983, Structures Associated with the Southwest Margin of the Ancestral Uncompahgre Uplift, Grand Junction Geological Society, 1983 Field Trip.

Yielding, G., 2002, Shale Gouge Ratio - calibration by geohistory: no. 1997, p. 1–15.

Yielding, G., T. Needham, and H. Jones. 1996. “Sampling of Fault Populations Using Sub-Surface Data: A Review.” *Journal of Structural Geology*.

Zwaan, F., G. Schreurs, J. Naliboff, and S. J. H. Buiter, 2016, Tectonophysics Insights into the effects of oblique extension on continental rift interaction from 3D analogue and numerical models: Tectonophysics, v. 693, p. 239–260, doi:10.1016/j.tecto.2016.02.036.

APPENDIX

ARAWA #1 WELL-SEISMIC TIE:

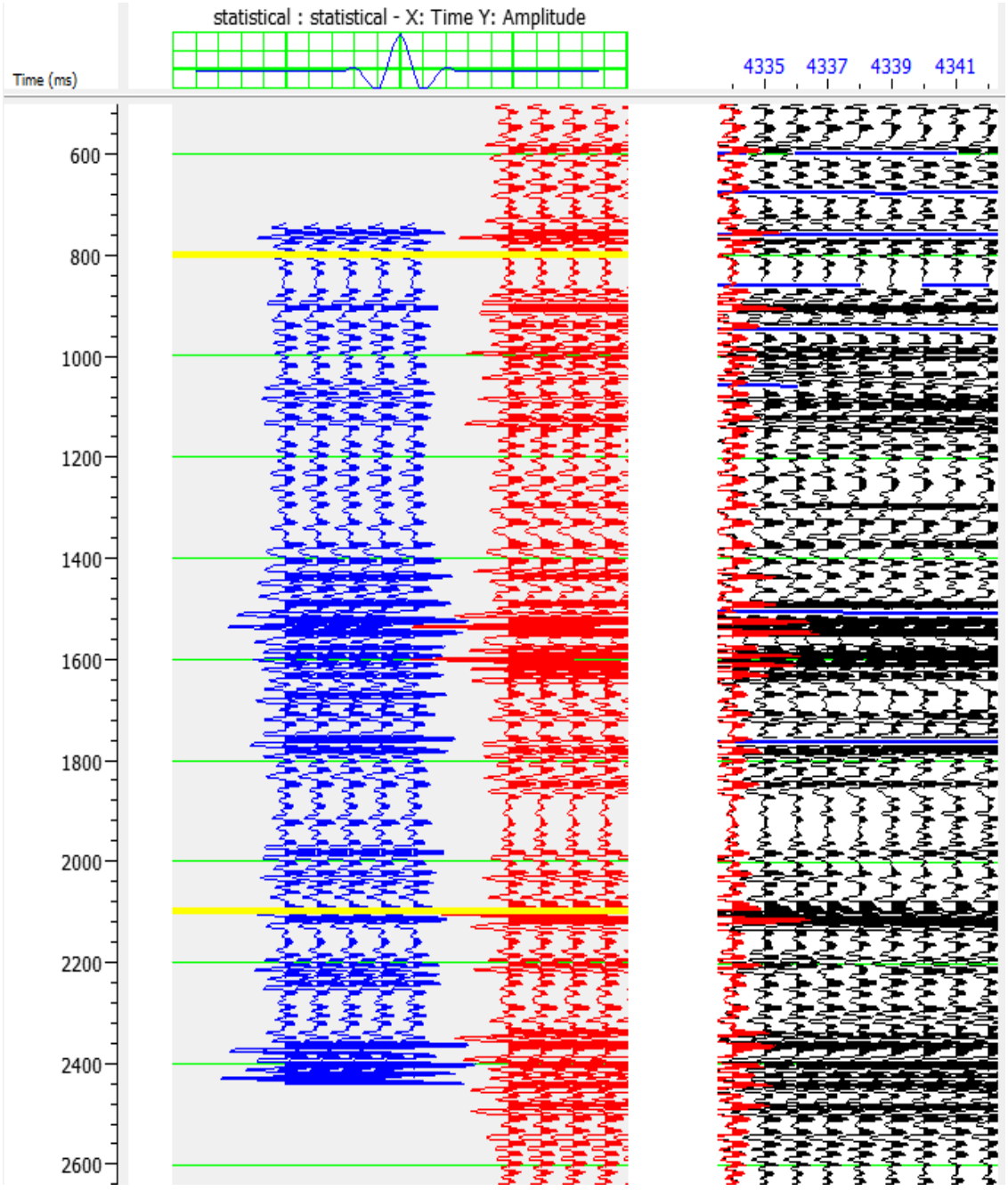


Figure A.1. Seismic well-tie for the Arawa #1 well.

OKOKI #1 WELL-SEISMIC TIE:

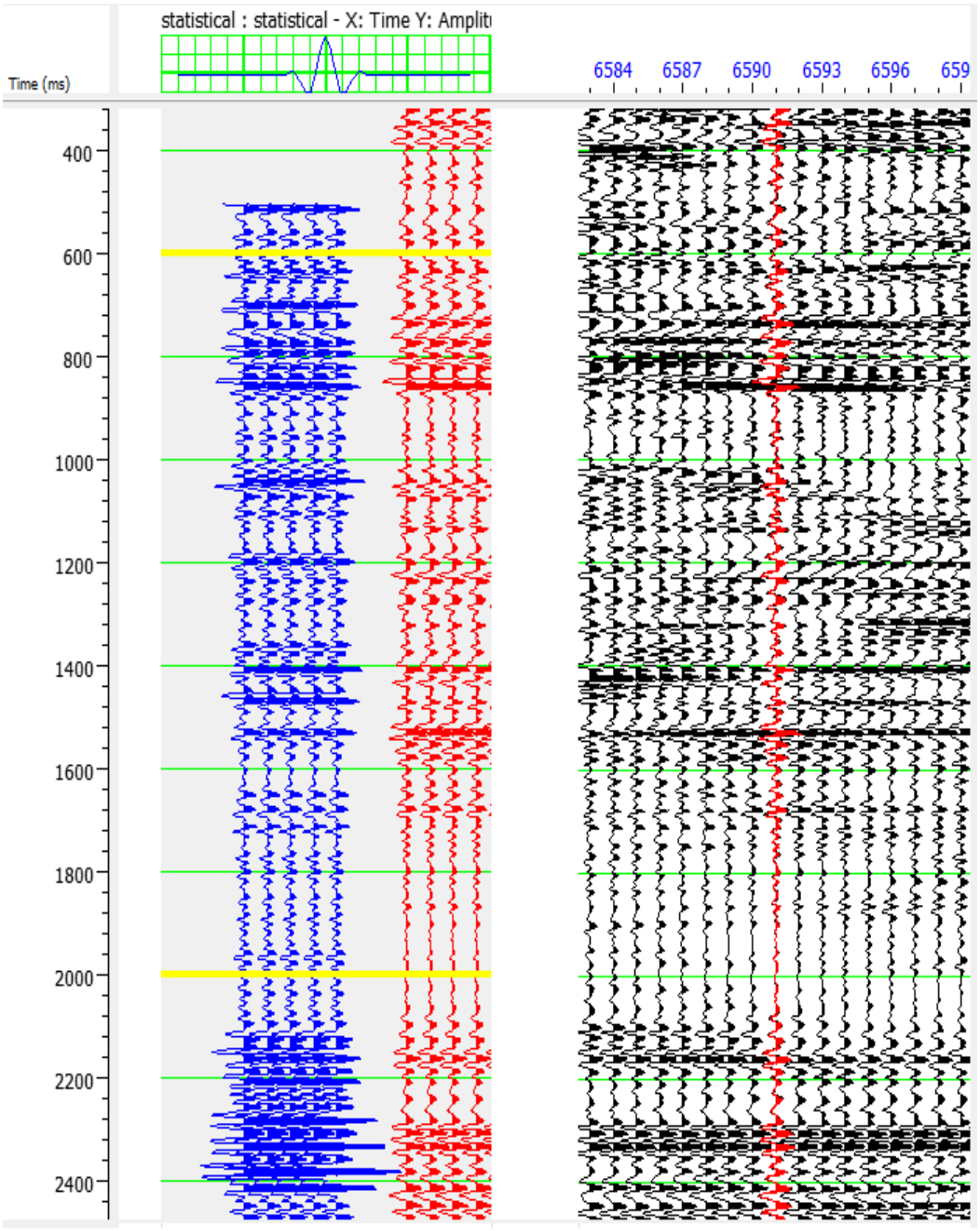


Figure A.2. Seismic well-tie for the Okoki #1 well.

TAIMANA #1 WELL-SEISMIC TIE:

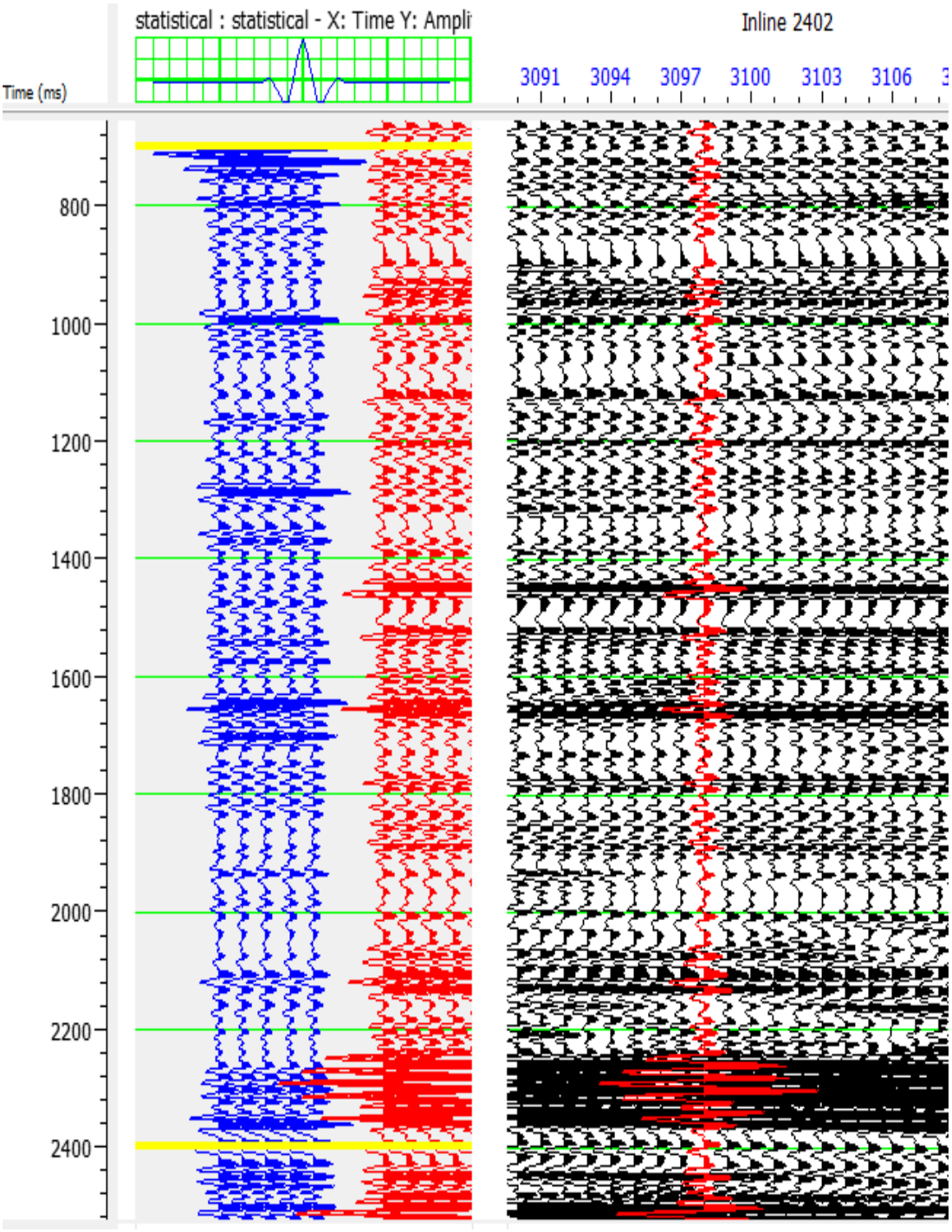


Figure A.3. Seismic well-tie for the Taimana #1 well.

WITIROA #1 WELL-SEISMIC TIE:

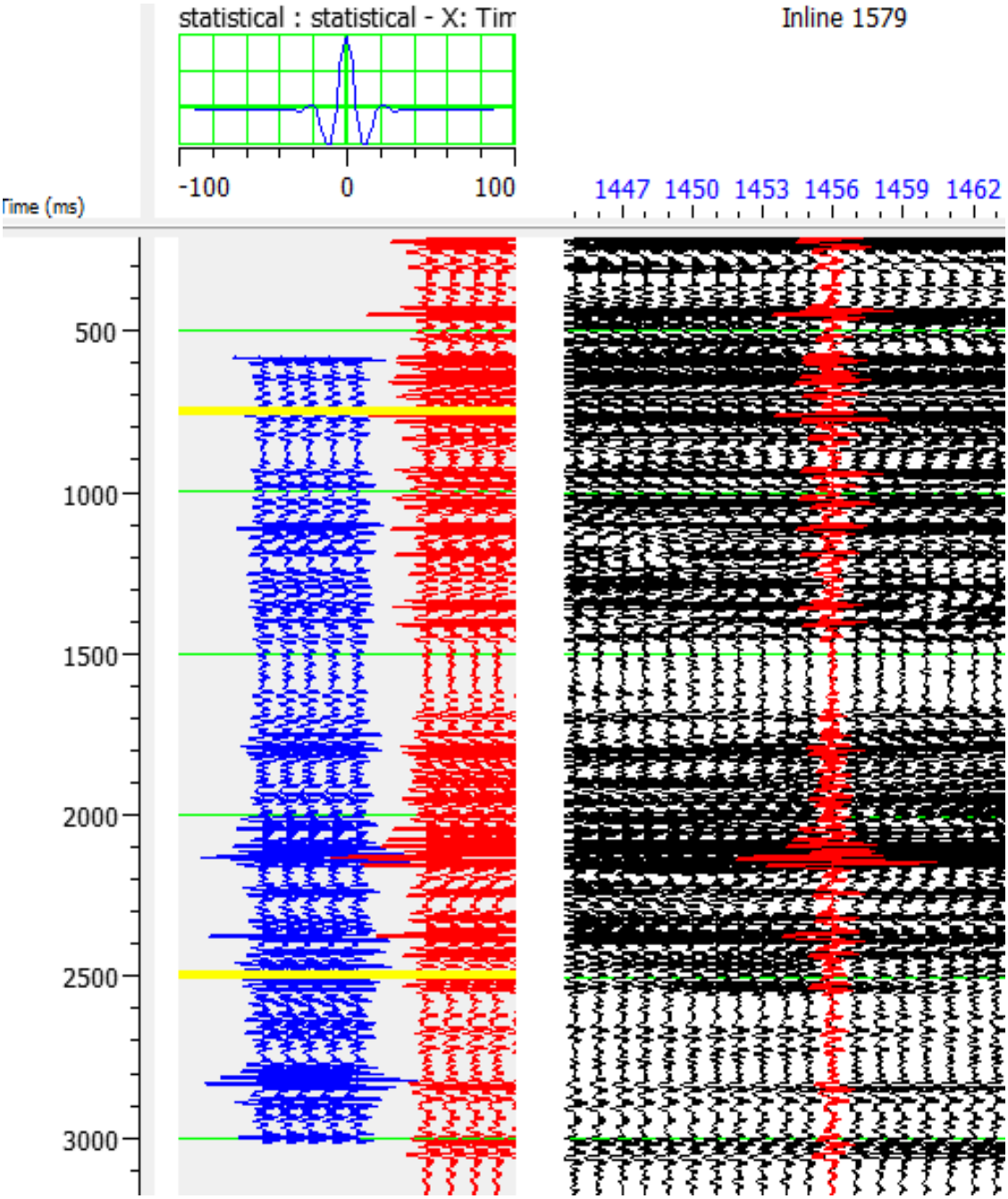


Figure A.4. Seismic well-tie for the Witoria #1 well.

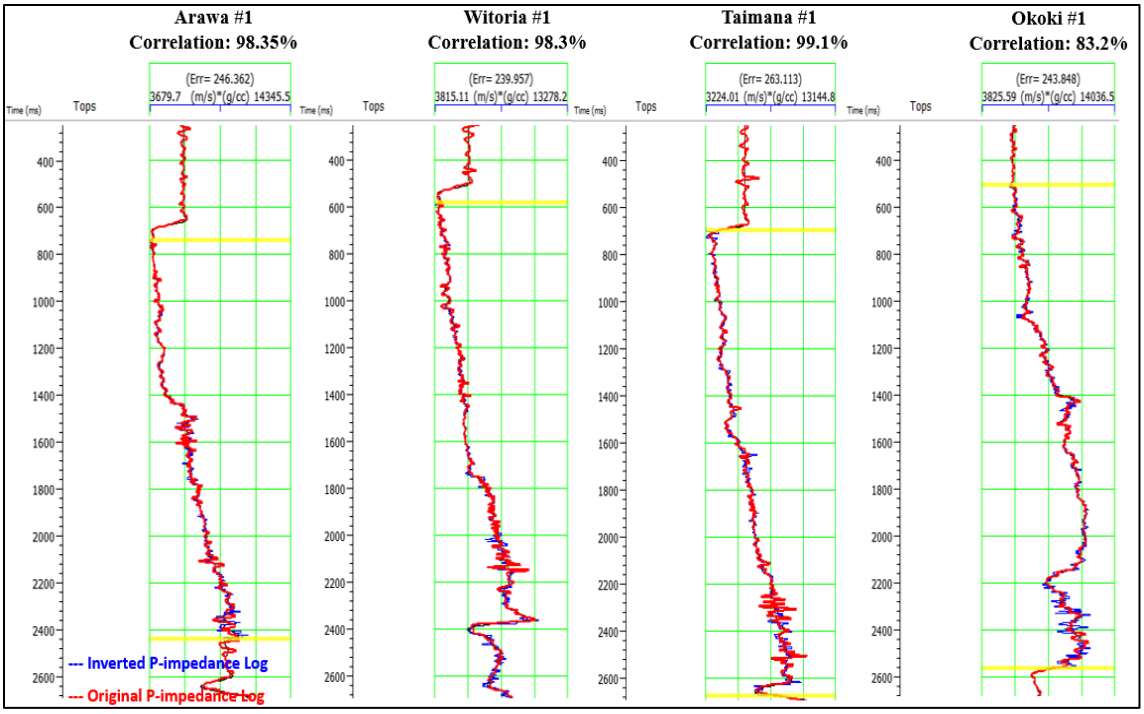


Figure A.5. Comparison between well logs and inverted P-Impedance.

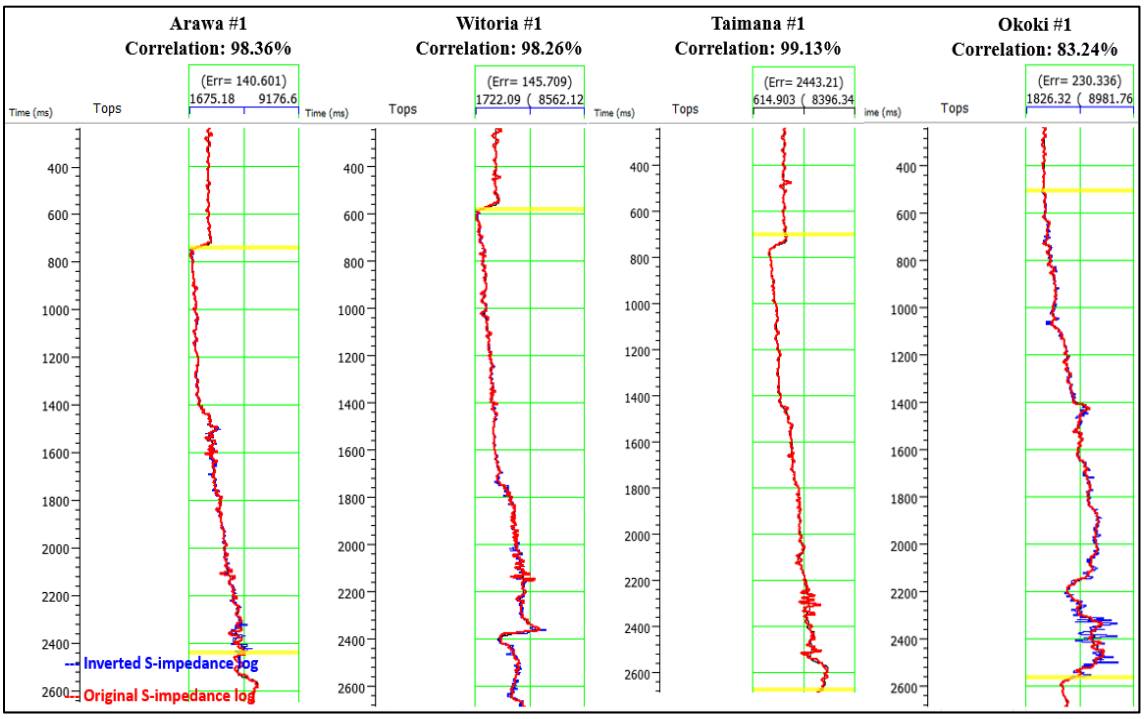


Figure A.6. Comparison between well logs and inverted S-Impedance.

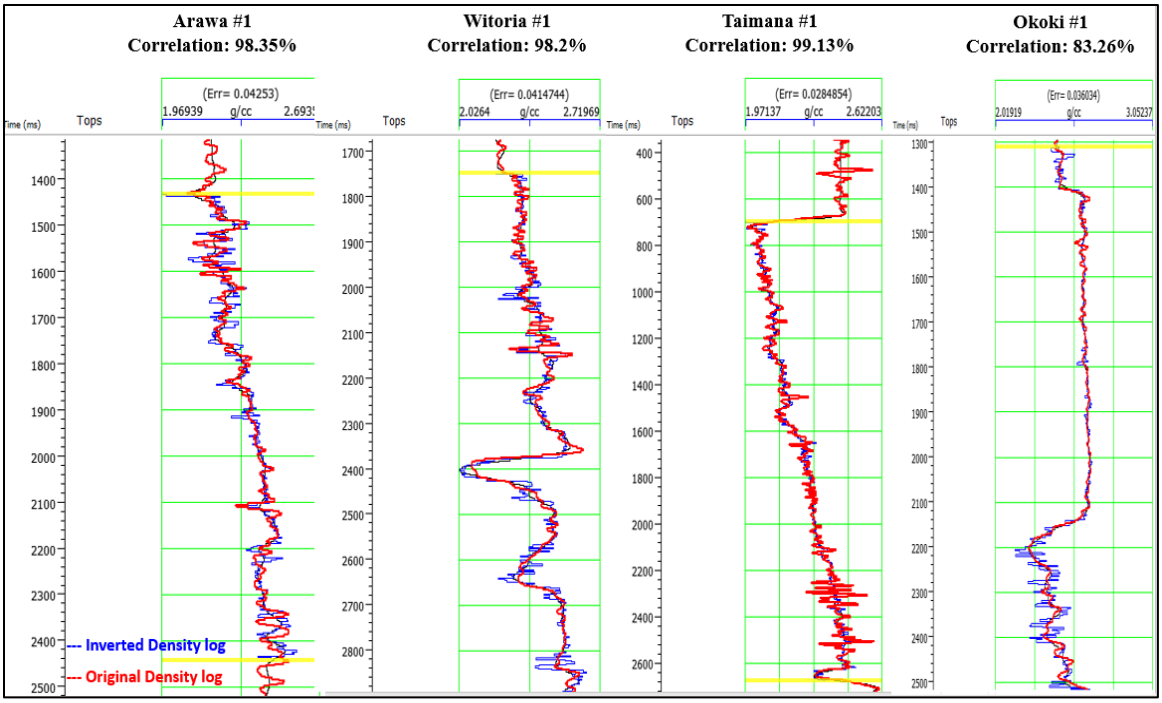


Figure A.7. Comparison between well logs and inverted density logs.

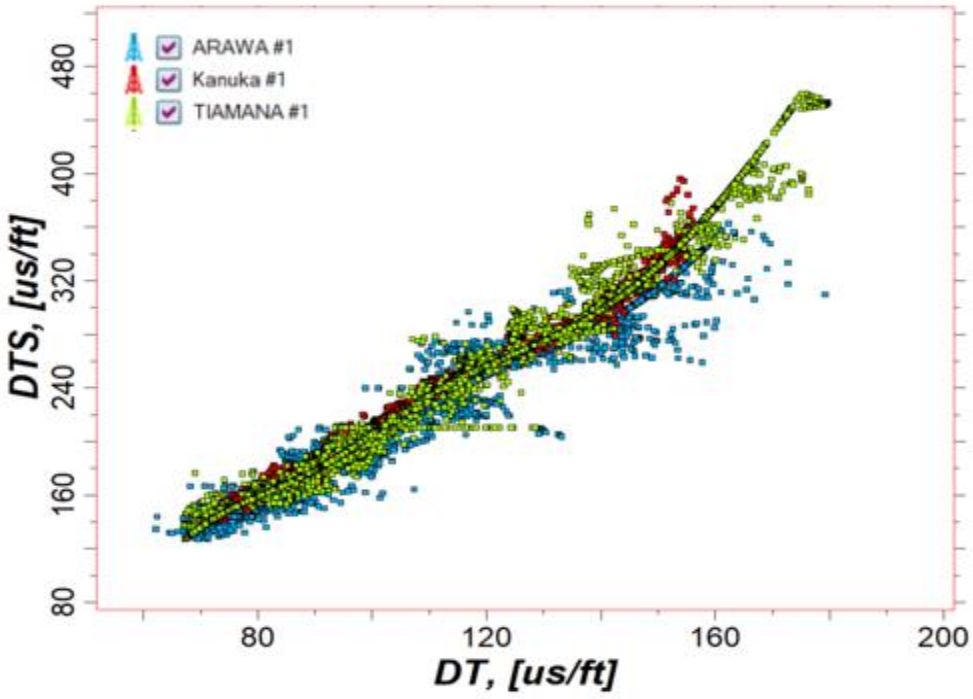


Figure A.8. Relationship between P-wave velocity and predicted S-wave velocity using a neutral network.

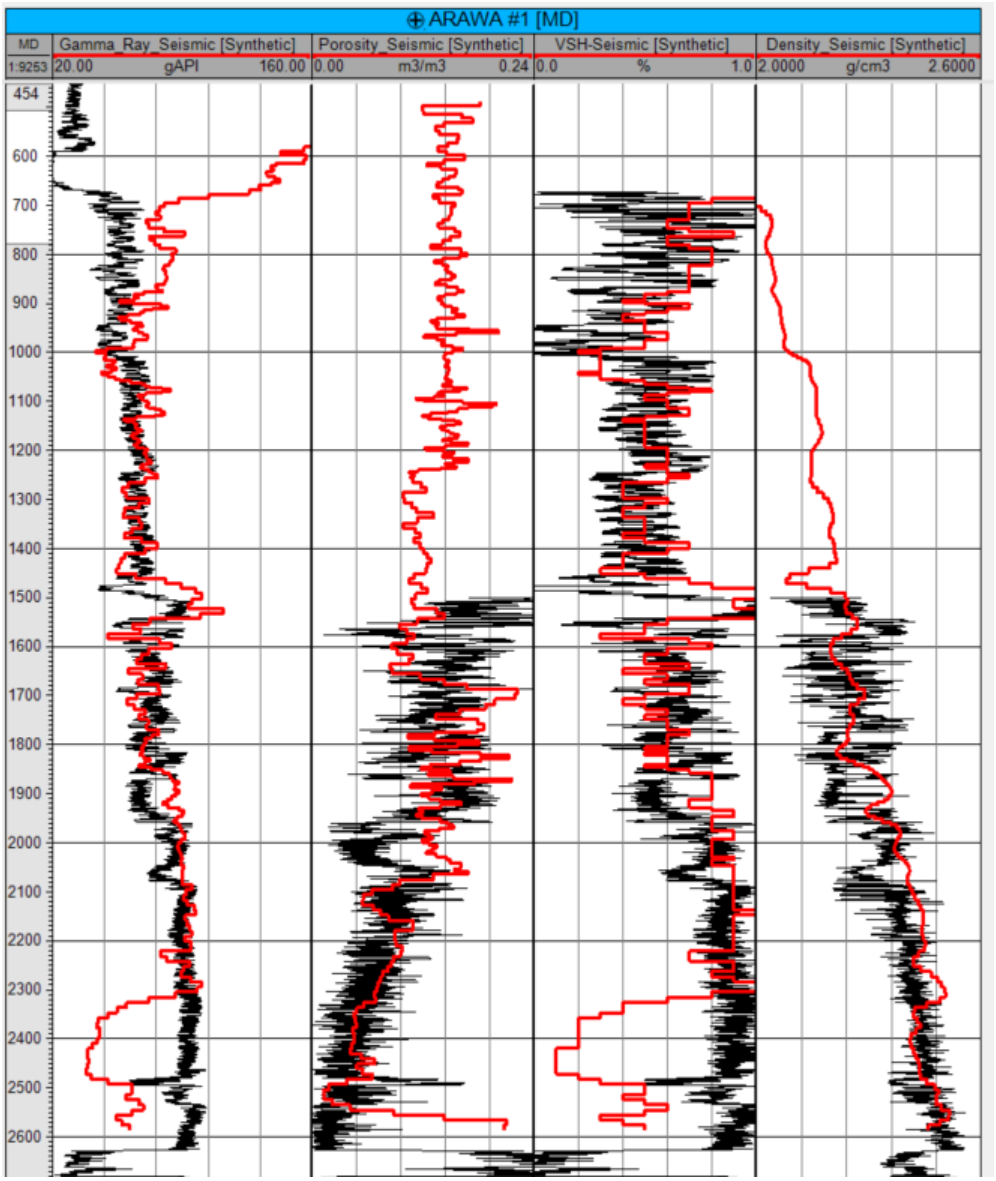


Figure A.9. Comparison between well logs and extracted seismic inversion properties (shown in red) at the Arawa #1 well location.

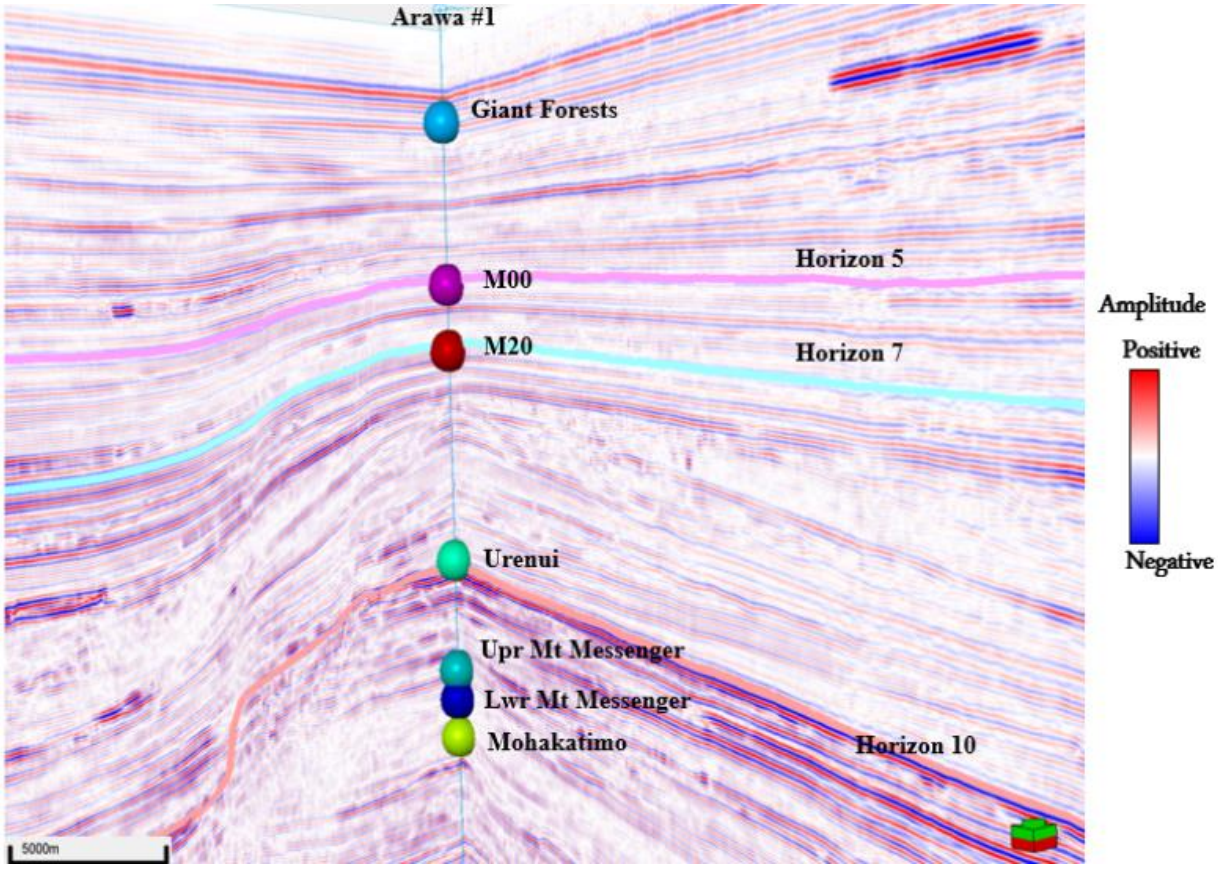


Figure A.10. 3D Seismic to well tie showing the main formation tops tied to the interpreted horizon.